RIGA TECHNICAL UNIVERSITY

Faculty of Material Science and Applied Chemistry
Institute of Inorganic Chemistry

Liene Plūduma

Doctoral Student of the Study Programme "Material science"

HYDROXYL ION QUANTIFICATION IN HYDROXYAPATITE AND THE EFFECT ON THE BIOLOGICAL RESPONSE

Doctoral Thesis

Scientific Supervisor:
Assoc. Professor., *Dr.sc.ing.*
KĀRLIS AGRIS GROSS

RTU Press
Riga 2017

Wonder is the beginning of wisdom

/Socrates/

ACKNOWLEDGMENTS

ANNOTATION

HYDROXYAPATITE, OXYHYDROXYAPATITE, HYDROXYL ION QUANTIFICATION, THERMAL ANALYSIS, FOURIER TRANSFORM INFRARED SPECTROSCOPY, RAMAN SPECTROSCOPY, HYDROXYAPATITE COATINGS, SURFACE CHARGE, OSTEOBLAST RESPONSE

Modification of the chemical composition provides a simple, but powerful approach in tailoring the properties of hydroxyapatite. To date, activity has been directed to measuring the calcium to phosphorous molar ratio, and substitution of calcium or phosphate. Less attention has been directed to the quantity of hydroxyl groups in hydroxyapatite. This is an issue with thermally processed hydroxyapatite, where hydroxyl ion content may be depleted and lead to changes in properties.

In the literature review of the thesis information about hydroxyapatite, it`s structure and properties are described, emphasizing hydroxyl ions. Literature about different analyze methods to identify and quantify the hydroxyl ion content in hydroxyapatite has been analyzed and summarized. Information about the influence of hydroxyl ions on the properties of hydroxyapatite coatings has also been described. Literature review concerning period from 1968 till 2017 compiles information in English and French. The experimental section has been written in two parts:

1. Measurement of the hydroxyl ion content - the preparation of standard hydroxyapatite has been described, the use of thermal gravimetric analysis for quantification of hydroxyl ions has been assessed, calibration curve for the determination of hydroxyl ion amount using Fourier transform infrared spectroscopy has been developed and results compared to Raman spectroscopy.
2. Influence of the hydroxyl ion content on the biological response of hydroxyapatite coatings - hydroxyapatite thermal spray coatings have been prepared and characterized, and the effect of hydroxyl ions on the osteoblast cell response has been studied.

The Doctoral Theses has been written in English, it consists of 134 pages, 46 figures, 16 tables, 8 appendices, and 193 reference sources.

ANOTĀCIJA

HIDROKSILAPATĪTS, OKSIHIDROKSILAPATĪTS, HIDROKSILJONU MĒRĪŠANA, TERMISKĀ ANALĪZE, FURJĒ TRANSFORMĀCIJAS INFRASARKANĀ SPEKTROSKOPIJA, RAMAN SPEKTROSKOPIJA, HIDROKSILAPATĪTA PĀRKLĀJUMI, VIRSMAS LĀDIŅŠ, OSTEOBLASTU ATBILDES REAKCIJA

Ķīmiskā sastāva modificēšana ir vienkārša un ērta metode hidroksilapatīta īpašību mainīšanai. Pašlaik galvenokārt tiek mērīta kalcija un fosfora molārā attiecība, kā arī noteikti piemaisījumi materiālā, taču hidroksiljonu daudzums hidroksilapatītā netiek noteikts. Šī problēma ir īpaši nozīmīga termiski apstrādātos hidroksilapatīta materiālos, kur hidroksiljonu daudzums temperatūras ietekmē mainās, kā rezultātā var tikt izmainītas materiāla īpašības.

Promocijas darba literatūras apskatā apkopota informācija par hidroksilapatītu, tā struktūru un īpašībām, liekot uzsvaru uz hidroksiljoniem. Analizēta un apkopota literatūra par dažādu pētīšanas metožu izmantošanu hidroksiljonu identificēšanai un daudzuma noteikšanai hidroksilapatītā. Apkopota informācija arī par hidroksiljonu ietekmi uz hidroksilapatītu pārklājumu īpašībām. Literatūras apskata veidošanai analizēti informācijas avoti angļu un franču valodās, kas aptver laika periodu no 1968. līdz 2017. gadam. Darba eksperimentālā daļa ir sadalīta sekojoši:

1. Hidroksiljonu daudzuma mērīšana – aprakstīta hidroksilapatīta standarta izgatavošana, izvērtēta termiskās gravimetrijas pielietošana hidroksiljonu daudzuma notiekšanai, izveidota kalibrēšanas taisne hidroksiljonu daudzuma noteikšanai ar Furjē transformāciju infrasarkano spektroskopiju un rezultāti salīdzināti ar Raman spektroskopiju.
2. Hidroksiljonu daudzuma ietekme uz hidroksilapatīta pārklājumu šūnu atbildes reakciju – izgatavoti un raksturoti termiski smidzinātii hidroksilapatīta pārklājumi un pētīita hidroksiljonu ietekme uz osteoblastu adhēziju un diferencēšanos.

Promocijas darbs uzrakstīts angļu valodā, tā apjoms 134 lpp. Darbā iekļauti 46 attēli, 16 tabulas, 8 pielikumi un 193 literatūras avoti.

CONTENT

ABBREVIATIONS

ACP	amorphous calcium phosphate
AFM	atomic force microscope
a.u.	arbitrary unit
CaF_2	calcium fluoride
cDNA	double-stranded deoxyribonucleic acid
cHA	conventional hydroxyapatite coating
Col1a1	collagen type I
CPP	calcium pyrophosphate
c.p.s.	counts per second
DAPI	4',6-diamidino-2-phenylindole
DCPA	dicalcium phosphate anhydrous
EU	European Union
FA	fluorapatite
FTIR	Fourier transform infrared spectroscopy
GAPDH	glyceraldehyde-3-phosphate dehydrogenase
HA	hydroxyapatite
HA_v6	standard hydroxyapatite heated in vacuum at 1000 °C for 20 h
HA_v8	standard hydroxyapatite heated in vacuum at 1000 °C for 48 h
HetCor	heteronuclear correlation proton spectroscopy
ht-cHA	hydrothermally processed hydroxyapatite coating
ICDD	International Centre for Diffraction Data
ICP-MS	inductively coupled plasma mass spectrometry
KBr	potassium bromide
MAS	magic-angle spinning
NMR	nuclear magnetic resonance spectroscopy
OAp	oxyapatite
OCN	osteocalcin
OH^-	hydroxyl ions
OHA	oxyhydroxyapatite
OPN	osteopontin
PO_4^{3-}	phosphate ions

PCR	polymerase chain reaction
P-value	probability value
RNA	ribonucleic acid
RSD	relative standard deviation
RUNx2	runt-related transcription factor 2
SEM	scanning electron microscope
STDEV	standard deviation
TCP	tricalcium phosphate
TGA	thermal gravimetric analysis
TTCP	tetracalcium phosphate
wt%	weight percent
XRD	X-ray diffraction
α-TCP	α-tricalcium phosphate
β-TCP	β-tricalcium phosphate

INTRODUCTION

According to the latest report (the year 2016) of the Organization for Economic Co-operation and Development (OECD) on the health problems in Europe, more should be done to improve the health of populations in the European Union (EU) countries to ensure healthy lives and promote well-being for all ages. Osteoarthritis is one of the most disabling diseases in developed countries – about 10% men and 18% women aged over 60 years suffer from it [1]. A sever form of osteoarthritis leads to the need of surgical procedures, mostly hip and knee replacement. Because of the physical inactivity, smoking, excess alcohol and injuries joint replacement procedures are becoming more popular even for younger ages. Based on the published statistics between the years 2008 and 2014, there has been 6% increase for the hip replacements and a 15% increase for the knee replacements in Latvia [2]. For wealthier nations, the increase for the orthopedic procedures performed each year is even larger (for example, 30% in Austria). Hip replacements are very high in demand in the EU, being performed 279 times per 100 000 inhabitants in Austria, and 112 times per 100 000 inhabitants in Latvia in 2014 [1, 2]. Joint replacements do not last forever, there is about a 5% chance of revision surgery within 10 years of a hip or knee replacement [3]. Also, about 10% of annual fracture patients experience nonunion or delayed healing reactions [4]. This has a significant influence on the quality of life and economical aspect.

Almost all hard tissues in human body consist of apatite. This is the reason for the wide study and use of apatite materials in medical fields: orthopedics, dentistry, and pathology [5]. Hydroxyapatite is the most popular biomaterial used for the reconstruction of bone tissue. Biocompatibility and bioactivity determine its use as a bone graft and coating of the metal components used in orthopaedic prostheses.

Fracture healing is a complicated process with the interaction of many factors, including cells and genes. If these factors are not sufficient or are interrupted, healing process is affected, which can result in a nonunion of the bone [6]. Since the viability of the implant depends on the biological processes at the bone-implant interface, the physico-chemical optimization of the implant's surface is essential to achieve a favorable and rapid bone integration. There is an increased incentive by society to increase the multifunctionality in materials, especially those used in high technology applications. It has been proposed that hydroxyapatite nanocrystals in a bone mineralization process are oriented in a specific direction along the collagen fibers [7, 8]. This suggests that an ideal hydroxyapatite implant should not only have the desired composition but also a specifically tailored surface.

Surface modification of implants with a hydroxyapatite coating has been extensively used, but the surface is random in terms of chemical phases, topography, and structural order. Plasma spraying of hydroxyapatite, which is the main process for commercial production of hydroxyapatite coatings, produces dehydroxylation, the removal of hydroxyl ions during heating [9], which effectively changes the properties. It has been suggested that the hydroxyl ions play an important role not only to provide the stoichiometry and thermal stability of hydroxyapatite but also to produce a surface charge [10]. The clear effect on material properties and the biological response has not been determined due to the absence of a suitable technique for hydroxyl ion measurement.

The structuring within hydroxyapatite goes beyond just changing the concentration of hydroxyl ions in the crystal lattice, but it can control the alignment of hydroxyl groups within the columns to produce a surface charge. Poling sintered ceramics has shown a higher cell population on charged surfaces [10], but the biological response has not been quantitatively related to the hydroxyl concentration. A full and detailed design of hydroxyapatite implant could show new capabilities to control cellular behavior and to enhance mineralized tissue formation. Enhanced fracture healing ability and long-term implant performance and stability would have a great economic and social impact.

Aim of the doctoral thesis:

To develop an easy accessible and usable method for hydroxyl ions quantification in hydroxyapatite, and to investigate the influence of hydroxyl ions on the biological response of hydroxyapatite coating.

Tasks of the doctoral thesis:
1. Investigate the use of thermal gravimetrical analysis for the quantification of hydroxyl ions in hydroxyapatite.
2. Develop a hydroxyl ion quantification method using Fourier transform infrared spectroscopy.
3. Compare Fourier transform infrared and Raman spectroscopy for the detection and quantification of hydroxyl ions in oxyhydroxyapatite samples.
4. Prepare hydroxyapatite coatings with ordered structure and different hydroxyl ion concentration.
5. Investigate the osteoblast response (cell adhesion and differentiation) on the hydroxyapatite coatings with different hydroxyl ion concentration.

Thesis statements to be defended:

1. Quantification of hydroxyl ions with spectroscopy gives more reliable and demonstrative results than thermal analysis.

2. Hydroxyl ion absorption line at 632 cm^{-1} in Fourier transform infrared spectra is more sensitive and gives more precise results of hydroxyl ion amount in oxyhydroxyapatite compared to the absorption line at 3570 cm^{-1}.

3. Increasing hydroxyl ion concentration in hydroxyapatite coating significantly improves osteoblast adhesion and differentiation.

Scientific novelty:

1. An easy-to-use method has been developed for the quantification of hydroxyl ions. Guidelines are provided for quantifying the hydroxyl ion content by Fourier transform infrared spectroscopy, Raman spectroscopy, and thermal analysis.

2. The hydroxyl ion content in hydroxyapatite coatings can be used to change the electrical potential and the resulting osteoblast cell response.

Practical significance:

1. An improved quality control method for hydroxyapatite implant materials.

2. Fourier transform infrared spectroscopy is a better hydroxyl ion detection and quantification tool compared to Raman spectroscopy and thermal analysis.

3. Identification of spectral peak that provides a more reliable indicator of the hydroxyl content.

4. Small variations in the hydroxyl ion content of hydroxyapatite lead to a noticeable effect on the in-vitro osteoblast cell response.

1. LITERATURE REVIEW

1.1. Bone

Bone is a metabolically active tissue that is capable of adapting its structure and repair itself. Bone is a biocomposite which main tasks are to provide structural support for the body, to protect the vital organs, provide an environment for marrow, and act as a mineral reservoir. Bone constantly undergoes remodeling as a result of the balance of the activity of osteoblasts, osteocytes (bone building and support cells) and osteoclasts (bone resorbing cells) [11, 12]. As a result of remodeling, the old, micro damaged bone is replaced with new and stronger bone to preserve bone strength.

Bone is composed of three major bone cells - osteoblasts, osteocytes, osteoclasts -, collagen, noncollagenous proteins (osteoid), and inorganic mineral salts deposited within the matrix. Bone structure from macro to molecular level is showed in Fig.1.1.
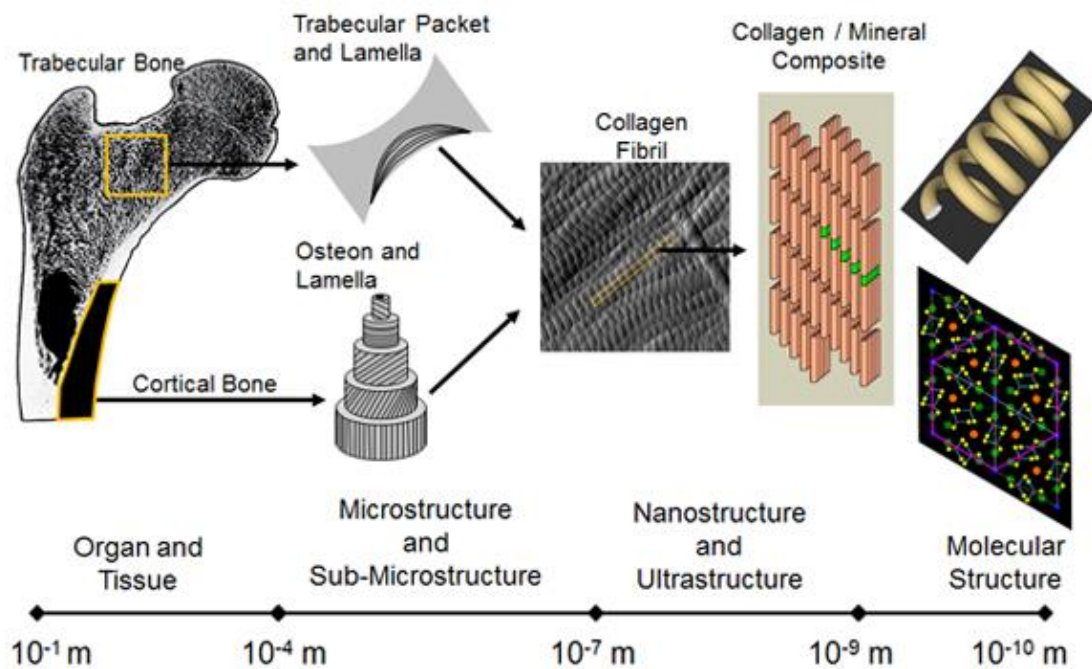
Fig. 1.1. Bone structure from macro to molecular level (modified from [13]).

Nano size hydroxyapatite platelets are oriented and aligned within self-assembled collagen fibrils. Collagen fibrils secreted by osteoblasts assemble into organized, close packed lamellar structure. Lamellae are organized concentrically around blood vessels to form osteons of the Haversian canal system. The osteons are then packed densely to form cortical (compact) bone or comprise a trabecular network of cancellous bone [7, 14]. In

mineralization process crystals may form within collagen fibrils (intrafibrillar crystals) or they can also form on the surface and between collagen fibers, in this case they are referred as interfibrillar crystals. The high degree of mineralization leads to a biocompostite – bone – which consists of around 65 wt% mineral phase, 25 wt% organic, and 10 wt% water [7].

Osteoblasts originate from mesenchymal stem cells of the bone marrow. They are involved in the synthesis of bone matrix and its mineralization. During differentiation osteoblasts secrete bone matrix around themselves, hence some osteoblasts become trapped forming osteocytes. These cells later form a calcified bone. Osteoclasts are large multinucleated cells which main function is the resorption of mineralized tissue (Fig. 1.2.) [15] Osteoclasts generate a localized acidic environment in order to selectively resorb biological apatite [16].
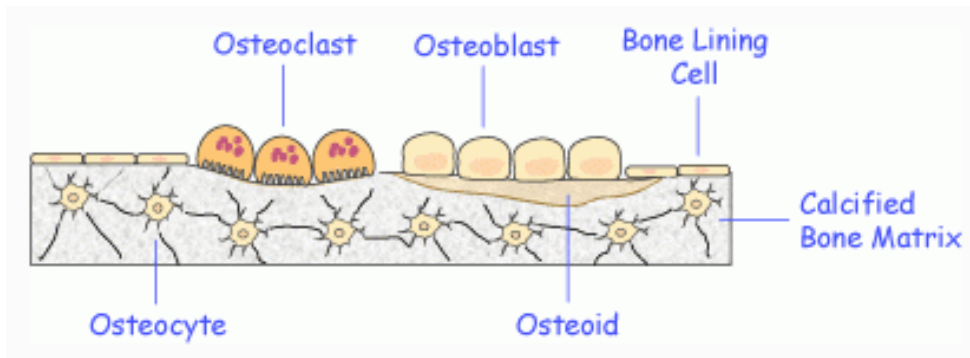
Fig. 1.2. Representation of bone cells and their role in the formation of bone [17].

Bone mineral consists of irregularly shaped platelets that are oriented with their c axis parallel to one another and lie along the collagen fibrils [18]. Bone mineral is calcium-deficient apatite with calcium/phosphorous (Ca/P) molar ratio less than 1.67, often referred as bone apatite or natural hydroxyapatite. It is formed by the maturation of amorphous calcium phosphate [7, 15].

1.2. Calcium phosphate biomaterials

Bone tissues exhibit the ability to self-regenerate when subjected to partial damage. If large loss of bone mass is present (result of trauma or disease) self-regeneration ability may be insufficient to promote bone healing, then bioactive biomaterial should be used. Such material should modulate cellular activities to stimulate self-regeneration ability of the bone tissue allowing a replacement of the biomaterial by new bone [11, 18].

Calcium phosphate biomaterials as bioactive and osteoconductive[1] materials allow attachment, proliferation, migration and phenotypic expression of bone cells leading to formation of new bone and forming intimate bond with the bone, thus creating strong interface. They were introduced as a bone substitute more than 50 years ago [19]. Calcium phosphate ceramics is widely used class of bioceramics. It includes both bioresorbable and bioactive materials. Bioresorbable calcium phosphates are especially requested to repair bone defects for younger people when it is more required for the body to create new bone tissues.

Based on the Ca/P molar ratio and the solubility of the compound there are a number of different types of calcium phosphates, most popular of them are included in Table 1.1. The solubility, thereby also bioresorbability, of calcium phosphates in water decreases in a row: ACP > DCPA > TTCP > α-TCP > β-TCP >> HA [20].

Table 1.1.

Most popular calcium phosphates in biomaterial field [21, 22]

Name	Abbreviation	Chemical formula	Ca/P molar ratio
Amorphous calcium phosphate	ACP	$Ca_xH_y(PO_4)_z \cdot nH_2O$	1.2-2.2
Dicalcium phosphate anhydrous	DCPA	$CaHPO_4$	1.00
Dicalcium phosphate dihydrate	DCPD	$CaHPO_4 \cdot 2H_2O$	1.00
Octacalcium phosphate	OCP	$Ca_8(HPO_4)_2(PO_4)_4 \cdot 5H_2O$	1.33
β-tricalcium phosphate	β-TCP	$Ca_3(PO_4)_2$	1.50
α-tricalcium phosphate	α-TCP	$Ca_3(PO_4)_2$	1.50
Calcium deficient hydroxyapatite	CDHA	$Ca_{10-x}(HPO_4)_x(PO_4)_{6-x}(OH)_{2-x}$ $0 \leq x \leq 1$	1.5-1.67
Hydroxyapatite	HA	$Ca_{10}(PO_4)_6(OH)_2$	1.67
Tetracalcium phosphate	TTCP	$Ca_4(PO_4)_2O$	2.00
Calcium pyrophosphate	CPP	$Ca_2P_2O_7$	<1.5
Oxyapatite	OAp	$Ca_{10}(PO_4)_6O$	

---

[1] biomaterial is considered osteoconductive if it allows attachment, proliferation and differentiation of osteoprogenitor cells at its surface, leading to the synthesis of an interface of mineralized collagenous bone matrix between bone tissue and bulk implant (by L. Hench)

Calcium phosphate biomaterials are still being widely researched to improve the properties and performance of the bone implant materials. According to the citation report results from the Web of Science database, the amount of published items which contains keywords "calcium phosphate" and "biomaterial" have increased from around 20 publications in year 1998 to 125 publications in year 2016 with more than 3500 citations in year 2016 (Fig. 1.3.).
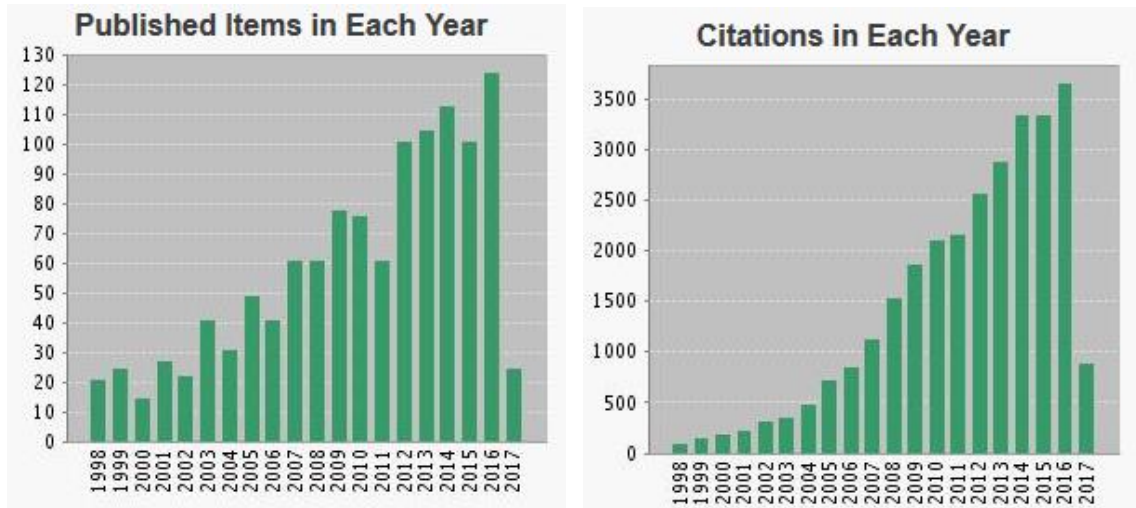
Fig. 1.3. Number of publications and citations about calcium phosphates each year. Citation report from Web of Science database using key words "calcium phosphate" and "biomaterials" (citation report created on 13.04.2017.).

Compared to hard tissues, calcium phosphate ceramics exhibit smaller mechanical strength and elasticity. Pure calcium phosphate ceramics is brittle with low modulus of elasticity, tensile strength and mechanical properties overall [23]. Consequently, it cannot be used in load bearing constructions. Because of these weaknesses calcium phosphate materials are mainly used as a bone defect filler (in the form of granules or cement) or a coating on a metal implant.

Hydroxyapatite, β-tricalcium phosphate and a mixture of both are the most popular calcium phosphates used for biomedical applications. According to Web of Science database, there are more than 220 items published containing key words "hydroxyapatite" and "biomaterial" in year 2016.

1.3 Hydroxyapatite for medical applications

1.3.1 Properties

Hydroxyapatite ($Ca_{10}(PO_4)_6(OH)_2$) is one of the most widely used bone regenerative material due to its compositional similarities to the inorganic extracellular matrix of bone tissues. HA exhibit excellent biocompatibility not only with hard tissues, but also with soft tissues such as skin and muscle, it is bioactive and promotes osseointegration[2] [18, 24]. Physical-chemical parameters of synthesized HA are showed in Table 1.2.

Table 1.2.

Physical-chemical parameters of synthesized hydroxyapatite [19, 25]

Parameters	Values	Notes
Theoretical formula	$Ca_{10}(PO_4)_6(OH)_2$	Composition can vary depending on a synthesis method and substitutions
Theoretical composition	39.68 mass% Ca; 18.45 mass% P	
Ca/P molar ratio	1.667	For stoichiometric HA
Spatial groups	$P6_3/m$ (hexagonal) $P2_1/b$ (monoclinic)	Transformation between monoclinic and hexagonal structure occurs at ~200 °C
Lattice parameters	a = b = 0.936 - 0.964 nm, c = 0.678 - 0.694 nm, $\alpha = \beta = 90°$, $\gamma = 120°$	For hexagonal structure
Theoretical density	3.16 g/cm^3	Varies with HA composition
Hardness (Moos scale)	5	Decreases with inclusion of H_2O and CO_3
Heat capacity	184.07 cal$\cdot$K^{-1}$\cdot$mol^{-1} at 298.16 K	HA synthesized by wet precipitation method and calcined at 950 °C
Thermal expansion coefficient	$(11-14) \times 10^{-6}$ K^{-1}	

---

[2] process when new bone is laid down directly on the implant surface and the implant acquires primary stability (definition by Schroeder)

Melting point	1614 °C	
Solubility	116.8 –log(K_s)	Aqua environment at 25 °C

HA ceramics exhibit low bending strength and fracture toughness under load-bearing conditions which is the reason why HA is generally used as a coating to improve bioactivity of metal implants and promote early fixation between bone tissues and implant surface [23].

For bone graft substitution HA can be used in different forms: granules, cement, coatings, porous and dense ceramics. Dense ceramics have been used as artificial vertebral bodies, iliac spacers, unloaded tooth root substitutes. HA can be used alone or as a composite with polymers or different ceramics. It can also be used in calcium phosphate cements and drug delivery systems [26]. HA can also be used as an adsorbent for bio-related substances such as proteins and amino-acids HA has been used as an adsorbent for chromatography mainly because of its ability not to cause denaturation of biorelated substances during the adsorbtion process [27]. The presence of hydroxyl ions in the structure of HA makes this material suitable for the use in electrical devices, as chemical sensors for detection of different gases [28, 29].

1.3.2 Structure

Apatite is widely available naturally occurring phosphate mineral on Earth. Stoichiometric apatites are usually represented by formula: $Me_{10}(XO_4)_6Y_2$ where Me represents a bivalent ion, XO_4 a trivalent anion and Y a monovalent anion. The structure of apatite supports numerous substitutions, but calcium phosphate hydroxyapatite is the most popular compound of this group: $Ca_{10}(PO_4)_6 (OH)_2$.

Biological apatite exhibit hexagonal crystal structure with a $P6_3/m$ space group. The characteristics for its crystal unit cell are as follows: a = b = 0.936 - 0.964 nm, c = 0.678 - 0.690 nm, $\alpha = \beta = 90°$, $\gamma = 120°$. To provide the lowest energy configuration for the elements in solid bodies, the PO_4 groups are distributed as regular tetrahedral where P^{5+} is positioned in the centre, but O^{2-} is in the four corners. The hexagonal unit cell consists of Ca^{2+} and PO_4^{3-} groups distributed within the unit cell (Fig. 1.4). There are two types of calcium atoms: four Ca atoms are located in Ca(I) position and bonded only to oxygen atoms, but the remaining 6 atoms take up Ca(II) locations in the corner of the hexagonal structure, surrounding the OH⁻ ions. Ca(II) are bonded not only to oxygen but also a

monovalent anion [30]. All six Ca(II) ions are not located within one plane. Each three Ca atoms are organized into a triangle. The OH$^-$ ion is centred inside the hexagonal unit cell. Similarly, the PO$_4$ are located in two triangles. The PO$_4$ groups create the base structural network that ensures stability of the apatite structure [5, 31, 32].
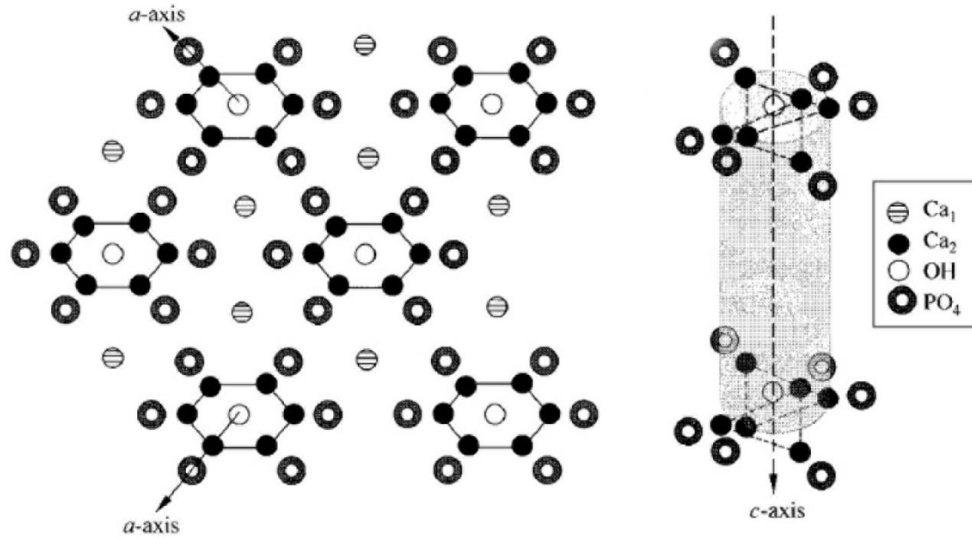
Fig. 1.4. The positioning of Ca atoms, PO$_4$ and OH groups in the HA structure (modified from [32].

HA structure consists of 0.30 – 0.35 nm wide channels along c-axis. They can be occupied by structural OH$^-$, other small ions as F$^-$, Cl$^-$, CO$_3^{2-}$ [5] or structural water [33]. In stoichiometric HA only hydroxyl ions are located in these channels, organized as …O-H O-H O-H… columns [34]. OH$^-$ anionic complex is too large to be positioned in the centre of Ca(II) triangle, so it is displaced above or below the plane (Fig 1.5). The ideal HA structure (space group P6$_3$/m) has a regular arrangement of OH$^-$ in a 'head-to-tail' arrangement to form columns within the channels, and half of the OH$^-$ in each column must be located above and half below the particular mirror plane [35].

Although mostly HA crystal structure has a space group of P6$_3$/m, pure, stoichiometric HA actually crystallizes in the monoclinic space group P2$_1$/b (Fig. 1.6). The main difference between the monoclinic and hexagonal symmetry is the ordering of OH$^-$ ions located in the (00z) column. Monoclinic symmetry characterizes with an order within and between columns which is not as exacting in the hexagonal phase [36]. Despite the monoclinic nature of HA at room temperature, it inverts to hexagonal structure at elevated temperature. There have been reported different conversion temperatures stating from 200 °C up to 370 °C [37-39].

(0,0,z)
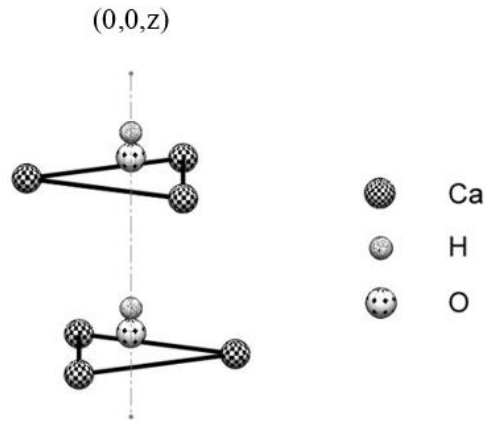
Fig. 1.5. One of the possible positions of OH⁻ in the structure of hydroxyapatite. Ca(II) triangle planes represent mirror planes at z = ¼ and ¾.

Although from thermodynamic aspect the monoclinic form of HA is more stable, hexagonal HA is more frequently observed and involved in biological bone formation because it allows for easier exchange of OH⁻ with other anions [40].
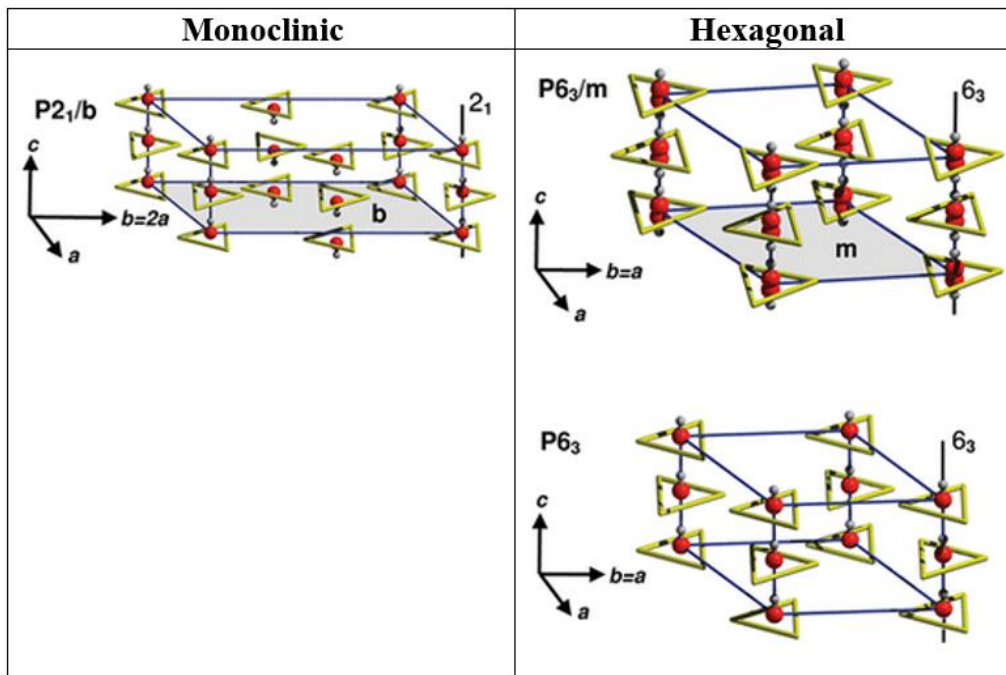
Fig. 1.6. Schematic of different possible HA structures: monoclinic (P2₁/b), experimental hexogonal (P6₃/m) and theoretical hexogonal (P6₃) unit cells. Experimental hexagonal symmetry means that each OH⁻ position statistically is only 50% occupied (modified from [40]).

22

1.3.3 Main factors affecting the hydroxyl ion amount in hydroxyapatite

Hydroxyl ions in apatite structure enables thermal stability of stoichiometric hydroxyapatite even until 1400 °C [41], they improve the structure and surface properties of HA coatings [42], as well as they might have a positive effect on the biological response of HA biomaterials [10]. As the structure of apatite is very flexible in accepting different substitutions (deliberately or as impurities during synthesis) and creating vacancies, it is necessary to know the main factors influencing the concentration of hydroxyl ions in HA:

1. ion substitution or incorporation in the structure
2. crystallite size
3. thermal treatment

Ion substitution in the structure. Different solid solution can exist between apatites with different compositions. Significant number of vacancies in XO_4 sites in apatite structure might produce a collapse of the structure and formation of other phases, whereas small defects like those corresponding to Me and Y vacancies allow preservation of the structure, although they are associated with a loss of cohesion and stability [43]. Figure 1.7 shows some of the possible cation and anion substitutions in apatite structure.
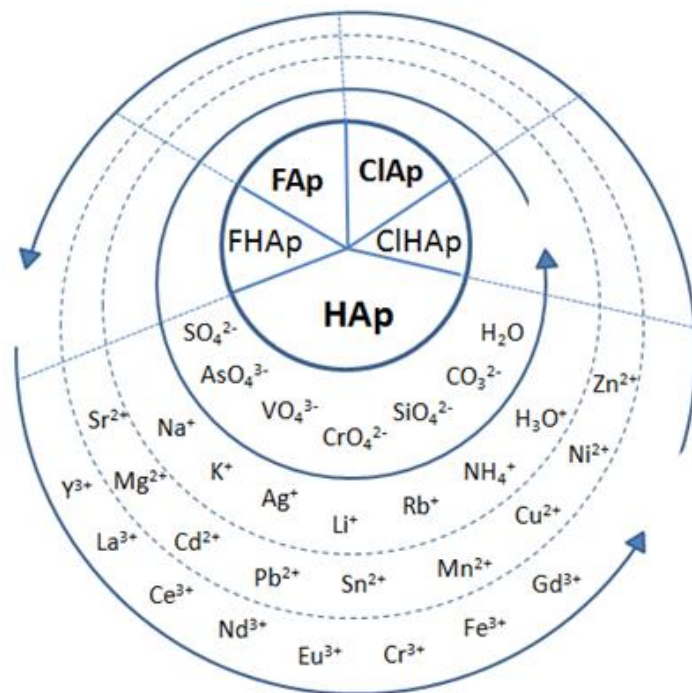
Fig. 1.7. Schematic representation of substitution elements in apatites. The inner layer shows anionic substitutions, while outer layer – monovalent, divalent and trivalent cationic substitutions [43].

Due to similar lattice parameters of the various apatite group minerals a large number of substitutions can occur. Splitting of OH^- stretching mode into more peaks in the range of $3495 - 3572$ cm^{-1} in Fourier transform infrared spectra of apatite indicates a substitutional reactions [44]. If an ion with different charge replaces another ion of the same sign, multiple substitutions occur to maintain a neutrality. Hydroxyl ion concentration can change in response to a change in oxidation state for a replacement ion. Substitution with silver will directly influence the OH^- ion concentration while strontium and magnesium will not cause a change [45, 46]. The lack of OH^- in biological apatites might be related to the substitution of OH^- by CO_3^{2-} (type A substitution) or the charge balance due to the replacement of PO_4^{3-} with CO_3^{2-} (type B substitution) [5, 47-49].

Molecules of adsorbed water can move from crystal surface into the lattice c-axis channels. That is followed by considerable structural disorder within and around c-axis channels and reduced amount of OH^-, particularly in the region underneath the apatite crystal surface [34]. *Yoder et al.* also indicate the presence of water in the hydroxyapatite structure. It has been assumed that water molecules are located within the calcium-ion channels, most likely replacing hydroxide ions. This might be occurring as a result of carbonate substitution which could widen the channel [33]. Stoichiometric apatite also shows HPO_4^{2-} on their surface due to a surface hydrolysis after contact with aqueous solutions. This property has to be taken into account in apatite reactivity and biological behavior [50]. The incorporation of CO_3^{2-} or HPO_4^{2-} into the apatite structure is related to a loss of negative charge and is mainly compensated for by complex defect associating calcium and OH^- vacancies [51].

Crystallite size. *Pasteris et al.* have suggested that the smaller the crystallite size, the greater is the atomic disorder within crystal unit cells and the less energetically favorable is for apatite to incorporate OH^- ions into its channel sites [16]. For biological apatites OH^- decreases in a row: tooth enamel, dentin, bone. In fact no OH^- band was detected in bone using Raman spectroscopy [16]. Study by *Rey et al.* using magic angle spinning proton nuclear magnetic resonance spectroscopy and resolution enhanced Fourier transform infrared spectroscopy confirms this finding [52]. *Pasteris et al.* have suggested that nanocrystallinity (low atomic order) suppresses OH^- incorporation into apatite. A correlation between the concentration of OH^- and the crystallographic degree of atomic order was found [16]. *Pajchel et al.* have also shown that OH^- in nanocrystalline apatite decreases and amount of water increases with decreasing crystal size [34].

Thermal treatment. The chemistry and resulting properties of apatite change in response to the source and processing history of hydroxyapatite. Hydroxyapatite, for use in the implant industry, is usually processed at high temperatures either by sintering at 1000 – 1350 °C or by thermal spraying that exposes particles to significantly higher temperatures [41, 53]. As a result of thermal treatment different processes in the following order can occur:

1. Dehydration – adsorbed surface water is reversibly removed from 25 to 200 °C without any effect on lattice parameters [43]. Water in pores, cracks and inter-crystallite locations is stabilized by capillary effects and requires temperature up to 400 °C for release [54].

2. Dehydroxylation (loss of hydroxyl ions) forming oxyhydroxyapatite ($Ca_{10}(PO_4)_6(OH)_{2-x}O_{0.5x}$) and then oxyapatite ($Ca_{10}(PO_4)_6O$). Dehydroxylation of HA begins at temperatures at about 900°C in air and 850°C in a water-free atmosphere [53-55]. Dehydroxylation can occur over a wide range of temperatures, it depends not only on the composition of the sample, but also on the heating atmosphere (Fig. 1.8).

3. Decomposition of oxyapatite forming a mixture of tricalcium phosphate and tetracalcium phosphate or tricalcium phosphate and calcium oxide [43].

The decomposition of HA is a process of continuous reactions, in which the conversion degree of dehydroxylation can strongly influence the critical temperature of subsequent decomposition. When OH^- are removed from HA structure, two OH^- ions combine to form one molecule of water: $2OH^- \rightarrow H_2O + O^{2-}$. This is followed by a small weight loss. Dehydroxylation introduces vacancies to create oxyhydroxyapatite with a similar crystal structure to HA [53, 56].
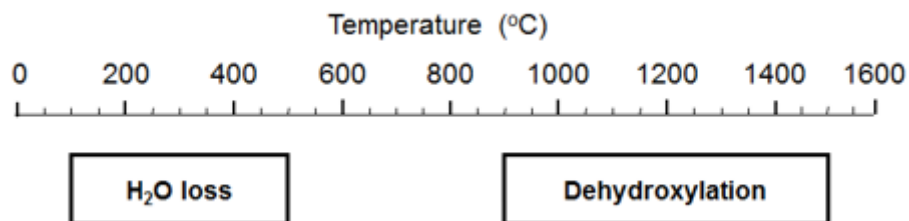
Fig. 1.8. Temperature range for the removal of adsorbed water and hydroxyl groups [57].

1.3.3.1 Oxyapatite

Apatite that retains the characteristic structure of hydroxyapatite, contains no hydroxyl ions in the structure, but has O^{2-} ions and vacancies (□) is called oxyapatite:

$Ca_{10}(PO_4)_6O_x\square_x$. As the temperature range for OAp stability is very narrow (around 800 – 1050 °C) [58, 59] and it easily absorbs moisture from the atmosphere [41], there is no reference in the literature at succeeding to produce pure OAp. It always contains a small concentration of OH ions, forming a solid solution of HA and OAp, called oxyhydroxyapatite $Ca_{10}(PO_4)_6(OH)_{2-2x}O_x\square_x$.

Despite the loss of the OH$^-$ ions, oxyapatite still retains the HA structure. Computer simulations made by *de Leeuw* showed that with regard to ordering of the channel O^{2-} ions in the a/b plane, ordered structure is energerically preferred over a random distribution of oxygen ions. Lowest energy configuration has all oxygen ions positioned in one a/b plane, located at a OH$^-$ symmetry position, with the next a/b plane of symmetry positions vacant. This positioning keeps the hexagonal symmetry of the material with a small uniform expansion in the c-direction [60]. Other studies show a rotation of the calcium triangles to compensate for the missing OH$^-$ ion, which reduces the overall crystal symmetry in the (001) direction [37, 61].

For the production of oxyapatite usually apatites with a column ions that are readily transformed to oxide ion are chosen, for example, hydroxyapatite or carbonated apatite [5]. A vacuume at high temperatures has been used to remove the OH$^-$ or CO$_3^{2-}$ ions, but pure OAp has never been obtained. Heating at too high temperature and/or for unnecessarily long durations will lead to a decomposition of the sample [54]. A very important property of highly dehydroxylated HA is that it can be easily rehydroxylated in a water vapour atmosphere at a temperature as low as 400°C [43, 56]. It is particularly important to eliminate all traces of water when OAp is to be prepared.

1.4 PHYSICO-CHEMICAL CHARACTERIZATION OF HYDROXYAPATITE

For full characterization of apatite (Me$_{10}$(XO$_4$)$_6$Y$_2$ where Me represents a bivalent ion, XO$_4$ a trivalent anion and Y a monovalent anion) a measurement of two atomic ratios is required: Me/X and Y/X assuming that the number of vacancies in X sites is negligible. However mostly only the Me/X ratio is considered. One of the reasons is the lack of easy-to-use method for determination of OH$^-$ content [51].

Usually HA is considered to be stoichiometric if Ca/P ratio is 1.67. If the ratio is below this point tricalcium phosphate is obtained as a second phase, if the ratio is above 1.67 – calcium oxide forms. Mostly Ca/P ratio is determined by titration for phosphate ion and by atomic absorption spectroscopy for calcium ion. Although according to International

standard ISO 13779-3:2008 (E) HA should be considered as being stoichiometric with regard to the Ca/P ratio and purity if after calcination at 1000 °C for 15 h it meets following three conditions [55]:

1. the absence of β- and α-tricalcium phosphate is confirmed by X-ray diffraction
2. the absence of calcium oxide is confirmed by X-ray diffraction
3. the absence of oxyapatite is confirmed by Fourier transform infrared spectroscopy (no absorption band at 434 cm^{-1}).

1.4.1 Measurement of the hydroxyl ion content

Markovics et al. from *National Institute of Standards and Technology* have made a detailed physicochemical characterization of the reference hydroxyapatite. According to this approach to determine the hydroxyl content, the concentration of all other ions in the sample has to be measured. The total number of hydroxyl ions was calculated from the difference between positive and negative charge of all unit cell constituents which were determined by following methods [62]:

- calcium content was determined by atomic absorption spectroscopy
- phosphorous was determined calorimetrically as a phosphovanadomolybdate complex
- hydrogen phosphate was determined by *Gee and Deitz* method (conversion of HPO_4^{2-} into $P_2O_7^{4-}$ and hydrolyzing it into PO_4^{3-})
- water content was determined from mass loss by TGA and sample weighting
- carbonate content was determined by automatic calorimetric titration (sample was heated and carbonates were collected in an absorption cell)
- trace elements were analyzed by inductively coupled plasma mass spectrometry.

This is an indirect method for measuring OH$^-$ amount, it depends on the quality of the methods used to determine the amount for all other constituents, and it is too complex and time consuming in cases when only the amount of OH$^-$ is needed.

Different chemical methods using sample dissolution and titration or water estimation by Karl Fisher reagent have been used for OH$^-$ determination, but there are difficulties with these methods if sample contains adsorbed water, carbonate, hydrogen phosphate or other ions that can influence the equilibrium of the reaction [5, 63], also Karl Fisher method does not distinguish between water already present or formed during the reaction [5]. It has also

been stated that chemical analytic techniques can not be used with a sufficient accuracy for the measurement of OH⁻ ions in apatites with complicated chemical compositions [64].

Considering the difficulties with chemical analyses, physical methods that allow direct determination of OH⁻ ion concentration are more attractive. There are several physical techniques that can be used for the quantification of OH⁻. They have focused on the:

1. thermal behavior (thermal gravimetric analysis),
2. structure (X-ray diffraction),
3. local atomic arrangements or molecular bonding (nuclear magnetic resonance, Fourier transform infrared and Raman spectroscopies).

1.4.1.1 Thermal gravimetric analysis

Thermal gravimetric analysis (TGA) and differential thermal analysis (DTA) record real-time changes in weight and heat and so can follow dehydroxylation of a sample. TGA can follow the loss of adsorbed water and dehydroxylation [65]. Despite this capability, authors who have used this method have not fully characterized their sample to show a complete loss of hydroxyl ions [65-67]. Furthermore, there is no mention of the best parameters for the use of TGA to determine the OH⁻ content.

Complete dehydroxylation of the hydroxyapatite unit cell will release a maximum of one water molecule. The use of TGA has revealed that complete dehydroxylation and further decomposition occurs at 1450 ℃. According to a theoretical calculations a weight loss of 1.79% is expected for a stoichiometric HA. This can be used to measure the extent of dehydroxylation for samples heated to different processing temperatures, by measuring the amount of retained structural water. The degree of dehydroxylation (DD) is:

$$DD = \frac{1.79 - WD}{1.79} \cdot 100$$

where WD is the weight loss as a percentage upon heating to 1500 °C [66]. For this calculation, the authors have assumed that other molecules are not released within this temperature range that can contribute to the weight loss.

Another method for determing the quantity of OH⁻ with TGA uses a mixture of apatite and CaF_2 heated to 800 °C (Fig. 1.9), where all the OH⁻ ions are replaced with F⁻ ions to form a fluorapatite and liberate water. The weight loss can be used to determine the OH⁻ concentration assuming that water is the only species that can be released [68].

Although TGA is a precize, fast and easy-to-use method for calculating the OH⁻ content, the presence of other volatile substances should be considered. For calcium phosphates that

contain HPO_4^{2-} a weight loss between 400 and 700 °C occures after forming pyrophosphate with a release of water [69]. Samples should also be checked for the presence of carbonate, and if necessary the weight loss of CO_2 should be subtracted [5]. A loss of carbonate starts at 400-500 °C and is compleated at 800 – 1200 °C [70], or other research shows the loss of carbonate between 630 and 1250 °C [71]. There have been different implications about the temperature of the release of structural water: *LeGeros et al.* showed the range of 200 – 400 °C [72], *Yoder et.al.* defined the region as 200 – 550 °C [33], while *Mason et.al.* extended it to 800 °C [73]. Weight loss in the 200 – 550 °C region can be attributed to the release of structural or lattice water [33] or it could be water resulting from the condensation of hydrogen phosphate ions to pyrophosphate ions [74].
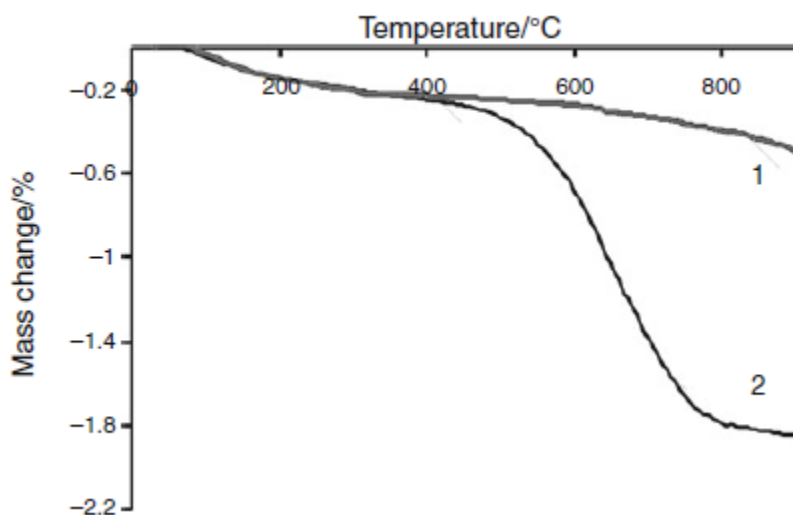
Fig. 1.9. Thermogravimetric analysis of (1) HA and (2) HA-CaF$_2$ mixture [43].

Mass spectrometry can be used in conjunction with TGA to determine the species released from the hydroxyapatite lattice during heating [43, 75, 76]. This can be used to detect both the quantity of CO_3 and water in the sample (Fig. 1.10). However, thermal gravimetric analysis – mass spectrometry (TGA-MS) is expensive and not readily available.
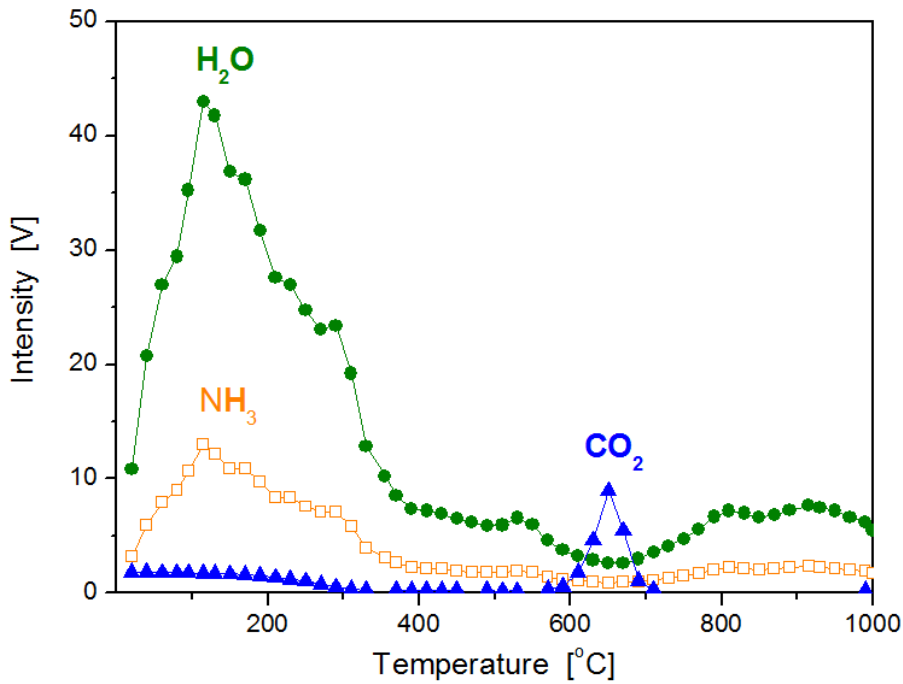
Fig. 1.10. Thermal analysis of carbonated apatite showing evolved gases from mass spectrometer (modified from [76]).

1.4.1.2 X-ray diffraction

Despite the widespread use of X-ray diffraction (XRD) for characterization of the crystal structure and chemical phase composition, it does not clearly show the degree of hydroxylation. Since the replacement of 2(OH$^-$) with an O^{2-} does not have a marked effect on the lattice parameters, XRD is not an easy method to differentiate stoichiometric hydroxyapatite from the dehydrated states [77]. The small increase in the height of the unit cell can be used to observe the shift of the (00*l*) type peaks to lower angles (Fig. 1.11) [78]. This allows the effect of dehydroxylation to be observed in solid solutions. Easier detection is possible with mechanical mixtures of hydroxyapatite and a highly dehydroxylated phase that will produce a doublet, most easily seen with the (004) peak at a 2θ of 53.1° with (Cu Kα source radiation) [78]. The (002) peak at 26.1° may also be used, but this is more complicated since the radiation from cathode ray tubes can produce a secondary peak while residual stress can contribute to a peak shift [61]. This requires particular attention to the source radiation and previous knowledge of the residual stress state of the sample being analysed. X-ray diffraction is useful for the evaluation of the crystal structure, but other methods are required to study the OH$^-$ concentration.
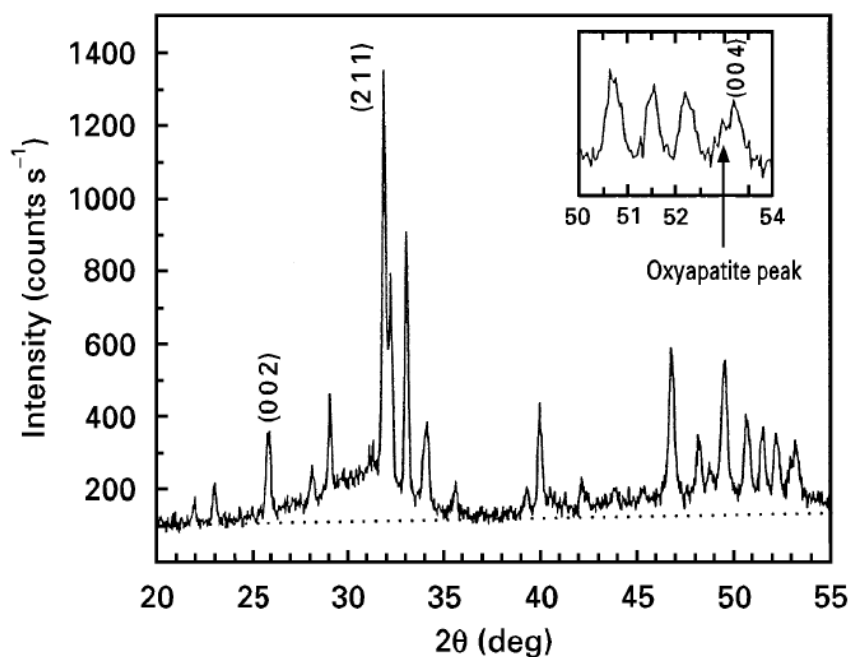
Fig. 1.11. XRD pattern of a hydroxyapatite coating produced by plasma spraying [41].
The oxyapatite peak indicates dehydroxylation of the HA.

1.4.1.3 Solid state nuclear magnetic resonance spectroscopy

Different solid state nuclear magnetic resonance (NMR) spectroscopy techniques have been used to detect OH^- ions in biological apatite while avoiding interference from organic species. The consecutive hydroxyls in the HA structure channels are too distant from each other to form hydrogen bonds (distance between two O is 3.44 Å), therefore their proton NMR peak recorded under magic-angle spinning (MAS) appears at 0.0 ppm [34].

Pajchel et al. have used the proton peaks at 0.0 and 5.4 ppm in ^{1}H and ^{31}P MAS NMR to quantify structural hydroxyl groups and water, respectively. Cross-polarization from the hydroxyl and water protons was used to analyze a complex ^{31}P MAS NMR line at 3.1 ppm that allowed to study the crystal interior and the crystal surface [34, 79]. Line at 5.4 ppm from ^{1}H NMR spectra can be related to both – adsorbed and structural water. Manipulations with different parameters allowed distinguishing between OH^- and water generated ^{31}P line at 3.1 ppm (Fig. 1.12). Chemical shifts of OH^- component were found at 3.10 ppm, for water – at 3.65 ppm. [34]. The interpretation of the ^{31}P MAS NMR spectra requires adequate caution and additional analysis, for example, to confirm that the broad peak does not arise from amorphous apatite. *Pajchel et al.* have showed with X-ray diffraction and Fourier transform infrared spectroscopy analysis that analyzed sample was fully crystalline

[34]. However, inverse cross-polarization experiments are time consuming, require long repetition times and suffer from loss of sensitivity [79].
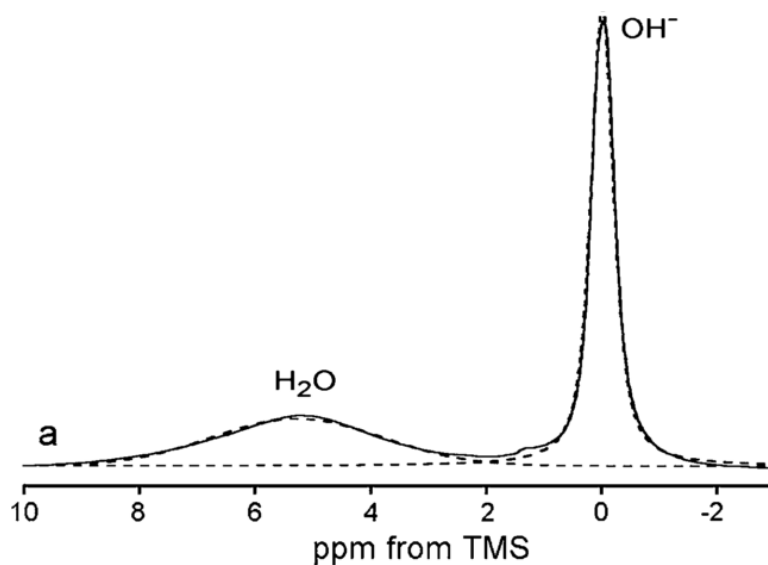
Fig. 1.12. Solid – state ^{1}H NMR spectra of apatite powder at 12 kHz (modified from [34]).

There have been attempts to measure OH$^-$ content by quantitative one dimensional (1D) proton MAS spectroscopy ('spin counting'). Because of baseline distortions and other artifacts in broad-line NMR spectra, it is unlikely that any reasonable estimate of the OH$^-$ content could be obtained by line fitting procedures on 1D spectra even when the signal-to-noise ratio is high [80].

The use of proton combined rotation and multiple pulse sequence NMR spectroscopy showed better spectral resolution than magic-angle spinning alone, but still could not completely eliminate organic matrix and water interference. However, very promising results have been obtained by two-dimensional (2D) ^{1}H-^{31}P heteronuclear correlation (HetCor) proton spectroscopy which relies on the radio frequency driven transfer of magnetization between different nuclear spin systems. As a result, only resonance from protons located within atomic distances (less than 1 nm) of phosphorous nuclei will generate the signal, and signal from organic matrix (which has less phosphorous content) are largely suppressed. The dipolar interactions for OH$^-$ ions at the crystal surface are different from OH$^-$ within the crystal. ^{1}H intensity in 2D HetCor spectra depends on many rate constants thereby these spectra are usually not used to quantify OH$^-$ content [80].

Solid state NMR has been also used to assess the local atomic environments in thermally processed hydroxyapatite. The observation of changes in HA coating induced by

plasma spraying is complicated due to the formation of amorphous phase. However, solid state NMR allows identifying local atomic environments in both crystalline and amorphous phases. The MAS line width is a function of the degree of order – depends on the preparation of the sample [81].

Initial studies showed a new peak in the ^{31}P spectra arising from dehydroxylation [82]. Further work has compared sintered hydroxyapatite with plasma sprayed hydroxyapatite looking at both the ^{1}H and ^{31}P spectra. *Hartman et al.* have analyzed large set of hydroxyapatite samples with different level of dehydroxylation (achieved by heat treatment in air), and suggests that 2D proton double-quantum spectra shows additional peaks for OH^{-} (5.2 and 7.5 ppm) which are adjacent to vacancies in the OH^{-} substructure. Double-quantum spectra can be used to study the distance of several protons in the structure. Depending on the degree of dehydration residual hydroxyl groups in the channel structure of oxyhydroxyapatite possibly form pairs stabilized by a bridging hydrogen bond [81]. However, *Wilson et.al.* suggest that 5.0 – 5.5 ppm peaks represent water, and these water molecules occupy vacancies in the crystal lattice, stabilizing the local structure by creating hydrogen bonding bridges between surrounding ions [83].

1.4.1.4 Infra red and Raman spectroscopy

Both, infra red and Raman spectroscopy, rely on the recognition of molecular bonding and can be used for quantitative analysis. From infra red spectroscopies Fourier transform infrared spectroscopy (FTIR) is the most widely used method. The peak positions or characteristic vibrations in spectrum correlate with the molecular structure of the crystal. Vibrations are infra red active if there is a change in dipole moment, but are Raman-active if there is a change in the polarity of the molecule during vibration [84, 85]. Each method shows slightly different vibrational intensities, making these methods complementary. Hydroxyapatite can thus be characterized by the

- absorption peak position that reflects the structure of the mollecules in the sample, even the slightest changes in the composition of material influence the bonding energy thereby the vibrational frequencies,
- peak width shows the atomic order in the unit cell of apatite, thus it reflects the crystallinity, and
- vibrational peak height or area can be used to determine the concentration of a molecular species

Stoichiometric apatite displays only OH$^-$ and PO$_4^{3-}$ absorption bands (Fig. 1.13 and 1.14). Wave numbers for the vibrational bands of HA are summarized in Table 1.3. Nano-crystalline HA exhibits a very weak OH$^-$ libration at 630 cm^{-1} and a very weak vibration at 3572 cm^{-1} [16, 86, 87], but with heating the sample, its crystallinity increases and so does the intensity of OH$^-$ absorption bands [16]. Heat treatment at increasingly higher temperatures decreases the absorption intensity at 630 cm^{-1}, thus reflecting the sensitivity of this peak to changes in temperature. However, the absorption peak at 3572 cm^{-1} is also indicative of the OH$^-$ concentration and becomes wider at higher temperatures as well as being more insensitive to the OH$^-$ concentration changes [86].
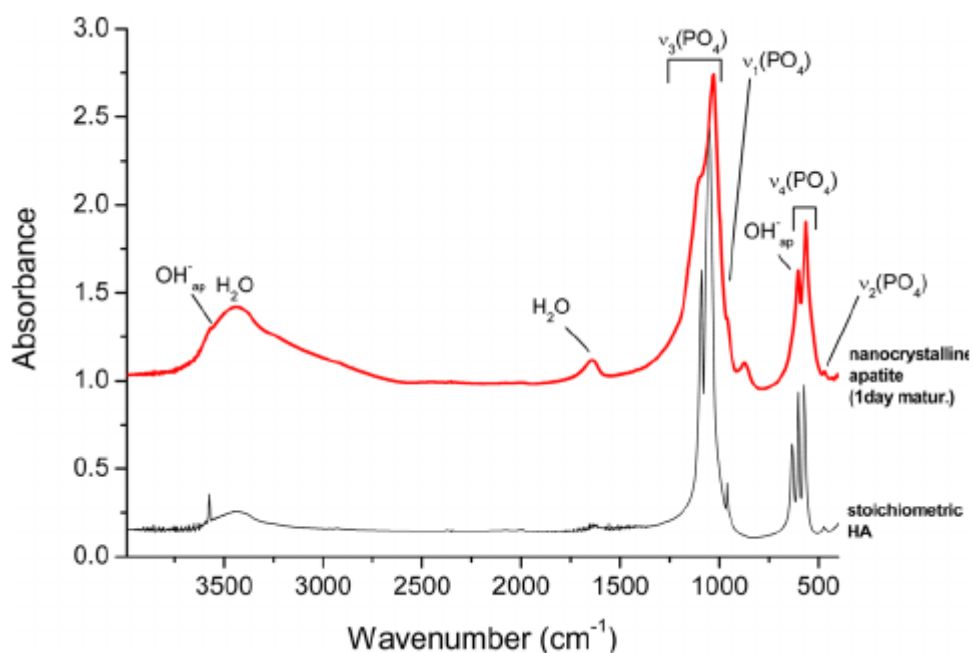
Fig. 1.13. FTIR spectra of stoichiometric and nanocrystaline hydroxyapatite [87].
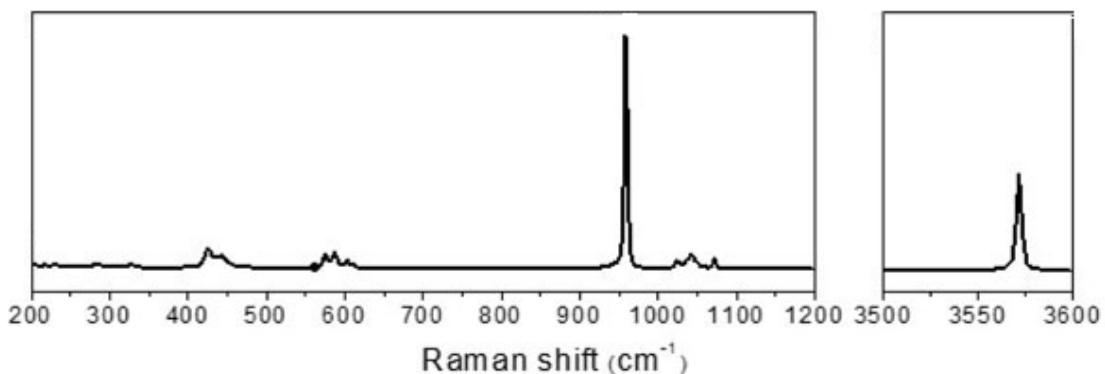
Fig. 1.14. Raman spectra of stoichiometric HA [88].

Table 1.3 .

HA vibrational bands in FTIR and Raman spectra

Band modes for HA		Wave numbers, cm^{-1}	
		FTIR [31, 62, 89, 90]	Raman [9, 16, 62, 88]
PO$_4^{3-}$	ν_2	464, 472	431, 447
	ν_4	567, 574, 601	579, 590, 607, 614
	ν_1	961	962
	ν_3	1026, 1034, 1040, 1063, 1090	1028, 1040 (shoulder), 1047, 1052 (shoulder), 1076
	overtones and combinations of ν_3 and ν_1	1950 - 2200 (weak)	
OH$^-$	Transnational mode	342	329
	Librational mode	635	
	Stretching mode	3571	3573

The concentration of hydroxyl ions can be calculated from the correlation of the intensity or area of the hydroxyl band at 3572 cm^{-1} and the phosphate band at 960 cm^{-1} [16]. Quantitative analysis requires a calibration curve made from samples with known OH$^-$ content. This requires a sample with the maximum possible OH$^-$ content and another sample without OH$^-$. Since ceramic processing causes dehydroxylation, the best calibration curve could then be made from solid solutions with different OH$^-$ contents. The major obstacle until now has been the production of oxyapatite. The purest oxyapatite reported in literature is 85% [91].

The amount of oxyapatite phase could also be used as an indication about the dehydroxylation level of hydroxyapatite. Identification of OAp is possible with spectroscopy. The replacement of two monovalent ions with a vacancy and a bivalent anion removes the hydroxyl absorption bands and creates additional phosphate absorption bands. This is explained with two unequal phosphate ions – while one PO$_4^{3-}$ is located closer to the vacancy, the other phosphate group is closer to the bivalent oxygen ion, O^{2-}. Oxyhydroxyapatite formed by heating HA in vacuum at 800 – 1000 ℃ produces two additional FTIR absorption bands at 475 cm^{-1} and 433 cm^{-1} [5]. Oxyapatite also has additional FTIR absorption peaks at 945 and 1025 cm^{-1}, but these are weaker and overlap

with existing phosphate peaks [54, 92]. The Raman spectra also show a change in the phosphate absorption peaks, forming a doublet at 950 and 968 cm^{-1} [93].

Although both methods, FTIR and Raman spectroscopy, gives similar information about the structure and composition of hydroxyapatite, there are some limitations for both of them. Strongly polarized bands have just a small change in its length during a vibration, therefore polar bands (C-O, N-O, O-H) have weak Raman scattering signal. However, they carry their charges during the vibrational motion, which results in a large net dipole moment change and produce strong IR absorption band [84, 94]. Some authors have also shown concerns about possible sample destruction and/or decomposition while taking Raman spectra, because of the long-term laser irradiation [84, 95]. Meanwhile the main drawbacks for the use of FTIR in HA analysis are the interference of water and atmosphere, and sample preparation that is crucial for obtaining good results. Water has a very broad and intense absorption peaks, as can be seen from the spectra recorded at the *National Institute of Standards and Technology* (Fig. 1.15), which means that any moisture in the sample and/or atmosphere can interfere with infrared analysis. This must be taken into account especially when analyzing hydroxyl groups which absorption bands coincide with the most intense absorption band of water. Nevertheless the interference of water can be limited by correcting the spectral background from the atmosphere and accurately drying and preparing the sample for analysis [55, 85].
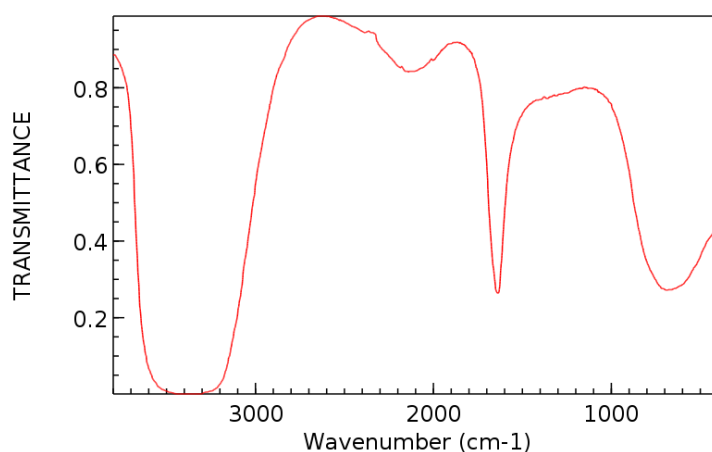
Fig. 1.15. IR spectrum of water [96].

Potassium bromide (KBr) sample preparation technique is used most widely for analysing hydroxyapatite samples. KBr is inert and transparent over a broad spectral range. A major drawback is that it is highly polar, which means it absorbs water from the

atmosphere very easily. Thereby a precaution must be used while preparing samples, especially if the absorption bands of hydroxyl groups in a sample are important. Sample preparation using KBr are described in details in various handbooks of FTIR, for example [85]. The most important things to remember are:

- sample must be ground to reduce the particle size to less than 2 microns in diameter. Bigger particles can scatter the infrared beam which causes a sloping baseline.

- Sample should be ground prior adding KBr. Grinding them together might cause a reaction between the sample and KBr. Besides, smaller KBr particles will absorbe moisture from the atmosphere easier.

- KBr pellet must be homogenious to ensure that a typical spectrum is measured, therefore it is important for the sample to be well dispersed in the KBr (lightly mixing together with spatula).

Improper or uncareful sample preparation for FTIR analysis can lead to incorrect results, which is particularly important if FTIR spectra are used for quantification purposes. Previous results show that too intense sample mechanical milling together with KBr might have caused the inclusion of hydroxyl groups in fluorapatite structure [57]. A study led by *Pajchel* also shows the uptake of the humidity from the atmosphere during milling of hydroxyapatite sample. Increasing surface area of crystallites favors this process (Fig 1.16). Water content was measured from TGA by heating the sample until 550 °C. Results suggested that adsorbed water molecules are capable of moving from the surface of apatite into its crystal lattice. It has been postulated that there is a proton exchange involving hydroxyl ions and water in c-axis channels. OH^- content decreases with the growing disorder within and around the c-axis channels [16, 34].
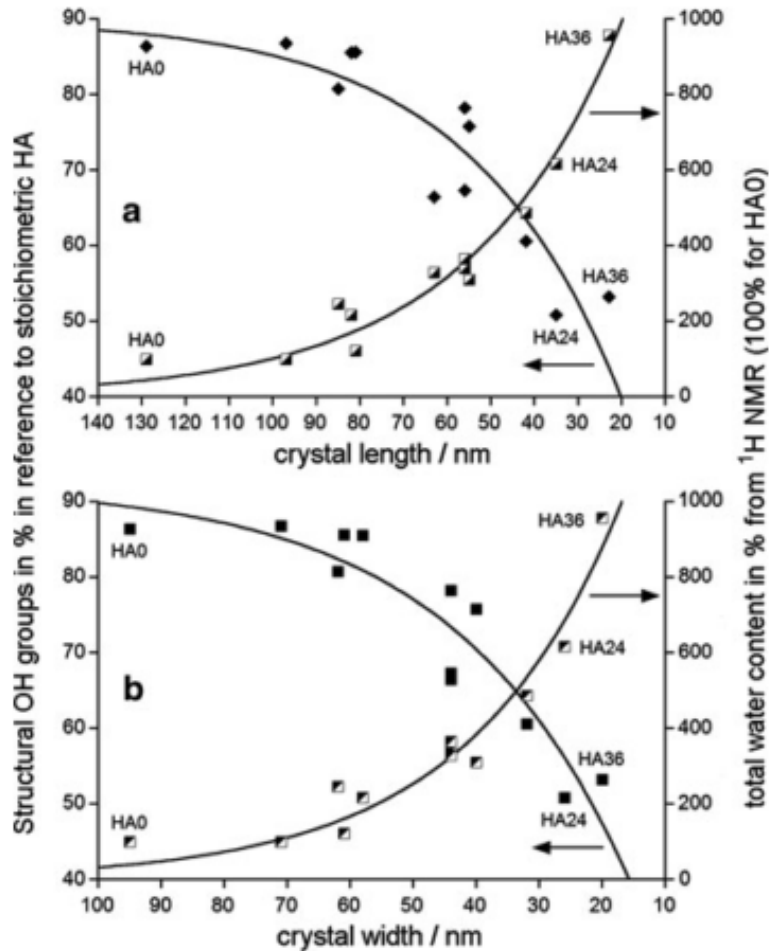
Fig. 1.16. The dependence of the concentration of structural OH⁻ groups and the total water content on the mean crystal dimensions: (a) on the crystal length, (b) on the crystal width. The OH⁻ and water concentrations were determined by proton MAS NMR [34].

1.4.1.5 Other methods

In addition to the most conventional methods (described above) information can also be found about other techniques used to characterize hydroxyl ions in hydroxyapatite:

- **X-ray photoelectron spectroscopy** allows the indirect determination of OH⁻ using P 2*p* and O 1*s* spectra. Using curve fitting it is possible to distinguish between P-O at 132.7 eV and P-OH at 133.8 eV bonds [42].

- **Electron microscopy** is a valuable technique for determining the crystal structure, but requires a high vacuum for electron diffraction. The concurrent exposure of oxyhydroxyapatite to the electron beam and the high vacuum produced dehydration and consequent decomposition and thus prevented the analysis of an oxyapatite [97].

The measurement of OH$^-$ has been a challenge not only to characterize biological and synthetic apatites, but also mineral samples – igneous apatites. The measurement of OH$^-$ mostly is carried out by measuring water concentration in mineral samples:

- **Electron microprobe analysis** has been used to determine OH$^-$ concentration as weight% of H_2O [98]. Disadvantage of this method is X-ray dependence on the exposure time of electron beam and crystallographic orientation that affects the detection limit of OH$^-$.

- **Secondary ion mass spectrometry** has also been used to measure H$^+$ content in apatite, but it does not give clear evidence weather H$^+$ source is OH$^-$ or some other functional group [99].

- **Elastic recoil detection** – a surface method that can determine absolute H$^+$ concentration in a surface layer. However the main disadvantages of this method are the requirement of large sample size, and inability to distinguish among different forms of H$^+$ [100]. *Wang et al.* combined elastic recoil detection with polarized FTIR to develop a method for quantifying the absolute values of OH$^-$ amount [100]. The calibration method developed requires the use of a single crystal apatite, is very specific for the use in geological field and is based upon using both analysis methods, thus making it time consuming.

1.5 Hydroxyapatite coatings produced by thermal spray methods

Low mechanical properties of hydroxyapatite ceramics are the primary limitations for its use as a load bearing implant. Mechanical properties of bone and synthetic HA are shown in Table 1.4. To overcome poor mechanical properties HA is coated on metallic substrates, thereby using the strength of the metal and biocompatibility of the HA ceramic. Many orthopedic implant systems use osteoconductive surfaces, such as, HA coatings to promote implant fixation to bone by direct bonding or osseointegration [101-104].

Table 1.4 .

Mechanical properties of hydroxyapatite and bone [26, 31]

Material	Tensile strength (MPa)	Compressive strength (MPa)	Young modulus (GPa)	Fracture toughness (MPa m$^{1/2}$)
HA	115 – 120	350 – 970	80 – 110	1
Cortical bone	78 – 196	160 – 250	4 – 30	2 – 12
Cancellous bone	10 -20	23	0.2 – 0.5	-

HA coatings can be produced by different techniques, such as thermal spraying, electrochemical deposition, sol-gel deposition, vacuum deposition, magnetron sputtering deposition, pulsed laser deposition and many others [101, 102, 105]. Thermal spraying is the most commercially used technique.

The metallic materials commonly used as implants are cobalt–chromium (Co-Cr) alloy and titanium (Ti) and its alloy, they provide good corrosion resistance and reasonable fatigue life. Before the coating procedure the surface of metal substrate should be prepared. Grit blasting alters the smoothness of the metal surface to produce a roughness of around several micrometers. This method has shown good implant fixation and is currently the major method for implants in clinical use [102].

Thermal sprayed coatings are formed from a stream of molten particles produced by injecting a powder in a flame or plasma jet. Powder with a particle size 20 – 50 μm is mostly used [82]. The quality of HA coating strongly depends on different characteristics of the powder such as particle size, distribution and morphology and powder chemistry. Powder particles with spherical geometry and narrow size distribution provide optimal heat transfer, increase efficiency of deposition, decrease coating porosity and surface roughness. HA coatings with a thickness around 50 μm show good fatigue resistance with good resorption and bone attachment characteristics. Coatings with thickness more than 80 μm become brittle, while very thin coatings often resorb too fast [106].

As during thermal spraying process HA particles are heated in air until a molten state, the structure and composition of HA coatings are different from bulk HA ceramics [107]. Studies have shown that the composition of the starting powder influences the phase composition of the coating [82, 108], especially because spraying is carried out in very high temperatures that lead to the partial dehydroxylation and decomposition of HA coatings.

HA with partly depleted hydroxyl ions can be described as a non-stoichiometric HA with distorted structure [81] or a solid solution of stoichiometric HA and oxyapatite [9, 45]. Thermal sprayed HA coatings also often express low crystallinity and high amounts of amorphous phase. The major phases of plasma-sprayed HA coatings are amorphous partially dehydrated monophosphate structures with only small amounts of TCP or TTCP, but about 70% of oxyapatite. [81, 109]. *Wang et al.* showed that during high-temperature plasma spraying HA lost part of its OH^- ions (showed by infra red spectroscopy) and increased its Ca/P ratio (showed by atomic emission spectroscopy). The results also suggested that the coating with lowest amount of OH^- had the strongest adhesion to a metal substrate [110]. Though this is an indirect conclusion knowing that this coating exhibited a higher extent of melting and had a denser microstructure. HA is unstable and most probably will undergo a phase transformation when the partial vapor pressure of water in the atmosphere is decreased. That implies that the scatter of OH^- ions is a sign of a stoichiometric instability of HA phase [110].

As HA is the most stable calcium phosphate phase, partial decomposition and formation of amorphous phase increase the dissolution rate and can also lead to a decrease in microstructural homogeneity and poorer mechanical properties and interfacial strength. All of that can leave an undesirable effect on the long-term fixation between the implant and surrounding tissues. For long term implants only HA with high crystallinity retains stable bone-HA-metal bond [107].

Gross described a model for coating formation from a single splat view (Fig. 1.17) [61]. For the case of a fully molten particle, crystalline phase formation depends on the quenching speed. The high quenching speed prevents the crystallization and supports the formation of an amorphous phase. It has been proposed that the amount of hydroxyl ions within the splat influence the ease of crystallization [41]. The core of the splat is expected to have the most hydroxyl groups as it was subjected to the least amount of heat during the coating process. That is why the middle part of the droplet will be the first to crystallize. The outer dehydroxylated layer will not have sufficient time for diffusion to form the decomposition phase, but with a lower driving force for crystallization to oxyapatite, will remain as an amorphous phase. The top of the droplet will cool more slowly, with heat dissipation through the already solidified droplet, and produce an oxyapatite in the upper part of the splat. For even slower cooling rates also the base of the splat can crystallize to an oxyapatite [61, 93]. At still slower quenching rates, the crystals will align with a <00*l*> orientation to provide a crystal orientation for the fastest heat dissipation [61].
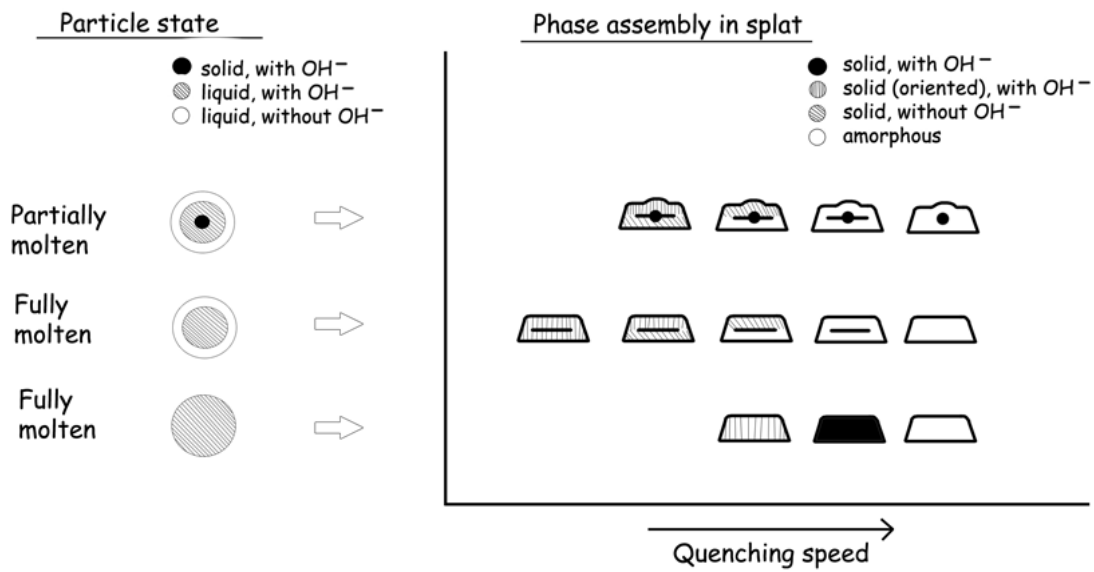
Fig. 1.17. Model showing the phase assembly in a splat depending on a quenching speed [61].

The presence of an amorphous phase makes it more difficult to analyze coatings with XRD. Hydroxyl ions might be trapped in the amorphous phase in which case the total OH$^-$ ion concentration cannot be determined because only the hydroxyl ion in the crystalline phase can be evaluated. Crystallization of the hydroxyl-rich regions takes place around 500 °C, while hydroxyl-depleted regions crystallize at 700 °C. Post-heating of the coatings at 700 °C allows the crystallization of amorphous phase to permit the analysis of total OH$^-$ content [45]. If the recrystallization is being done in air, OH$^-$ ions from the atmosphere can be included in the apatite structure. Rapid heating in the moisture free environment should be used. The absence of moisture must be maintained also during the testing of the sample.

Plasma sprayed HA coatings are widely used in commercial applications, but due to the very high temperature used in the process OH$^-$ depletion, amorphous phase formation or even partial decomposition can occur. It results in higher dissolution rate compared with a crystalline HA. This may lead to decrease in the microstructural homogeneity, and poorer mechanical properties, which will undermine the long term fixation between the implant and surrounding bone tissue. In order to improve the bioactivity - achieve better osteointegration or faster bone formation – surface modification of HA bioceramics has become essential.

1.5.1 Crystal alignment

Well controlled orientation might be a key factor in the development of high-performance materials. Naturally occurring HA often exhibits preferred crystal orientations resulting from highly specific biological processes, which influence the biological and biomechanical performance of hard tissues. HA orientation in living bone and dental enamel is different: c-planes are parallel to the enamel surface while a,b-planes are exposed on the bone surface [111].

Although much attention has been given to the texturing of bulk and thin ceramics for the application as piezoelectric, ferroelectric and thermoelectric materials, less have been done to texturing biomaterials. Some recent studies indicate that improved mechanical properties and bioactivity can be achieved through preferred orientation effects [112-114]. *Kim et al.* using nanoindentation have showed that c-axis oriented HA coatings have higher hardness and Young's modulus compared to HA coatings with randomly oriented crystals [112]. Studies on protein adsorbtion have shown that calcium phosphates with tailored crystallographic texture may enable a control of different cellular processes [112, 115-117].

Crystal alignment for HA coatings can be easily achieved during thermal spray process (Fig. 1.18). Substrate preheating at 400 °C produced aligned crystals for thermal spray HA coating. Diffraction peaks at 26.1° and 53.1° 2Θ correspond to HA peaks for the (002) and (004) planes. When a splat is subjected to heat from the thermal source, crystal growth occurs in the direction with the fastest heat dissipation. This corresponds to the (00l) direction explaining the high diffraction peak intensity from the (002) and (004) planes in the X-ray diffraction pattern [118].
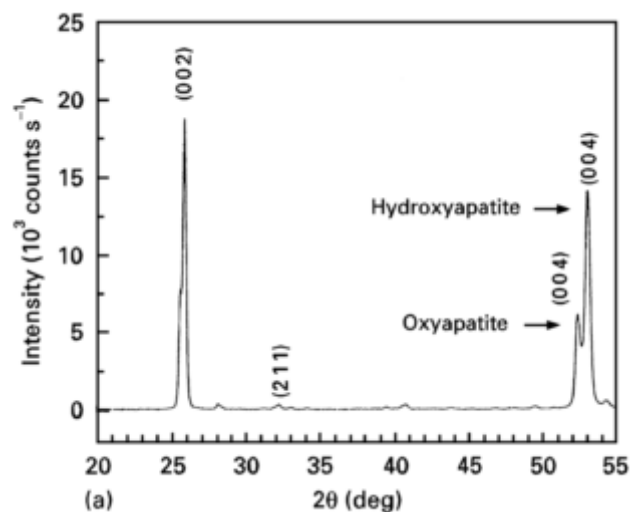
Fig. 1.18. XRD pattern of HA coating showing preferred crystal orientation [41].

43

Studies have showed that HA crystal alignment can be achieved also using pulsed laser deposition process. Increased laser energy increases the tendency for the c-axes of the HA grains to align perpendicular to the substrate [113, 119]. *Kim et al.* suggest that an important role in the surface texture development plays not only the dehydroxylation effects and anisotropic stresses during the deposition, but also a transport of hydroxyl ions [113]. Since OH^- is essential for HA formation, pulsed laser deposition should be carried out in an OH^--rich environment to compensate for dehydroxylation. As a result, coating can contain alternating layers of OH^--rich and OH^--poor areas. This gradient could work as a driving force for OH^- transport. Hydroxyl ions in HA crystal structure are located along the c-axis with no intervening atoms between adjacent groups. This atomic arrangement supports efficient OH^- transport along c-axis if sufficient driving force is applied. As a result the crystallization of HA grains with c-axis aligned in the direction of OH^- transport is expected [114]. Aligned crystals may grow faster than crystals with random orientation because OH^- stacked along the transport direction effectively function as channels that facilitate OH^- diffusion and incorporation into the neighboring regions [113].

Different methods have been used to produce orientation-controlled HA particles, coatings and dense ceramics. *Sato et.al* have prepared (100) plane (c-axis) oriented HA crystals by Langmuir-Blodgett method on substrates using carboxyl groups as a nucleation center [120]. Fiber-like (c-axis oriented) and plate-like (a,b-axis oriented) particles have been synthesized using the precipitation [121] or hydrothermal [122, 123] methods. Orientation-controlled HA coatings have been produced using electrochemical [124], thermal spray [41, 125] and pulsed laser deposition methods [112].

1.5.2 Hydrothermal treatment

Various post-treatments have been studied to restore the crystallinity of HA coatings. *Lin et al.* have done detailed analysis to show that decomposition phases in correct processing conditions (even heating in air) are able to reconstruct HA [109]. Hydroxyapatite requires water in the sintering atmosphere to remain phase purity and hydroxylation [56]. It has been reported that a hydrothermal treatment of plasma sprayed HA coatings can improve its properties.

Hydrothermal process even used as a HA synthesis method has shown very promising results for preparing well-crystallized and non-agglomerated crystals with homogeneous grain size, shape and composition. One of the advantages is also the use of low temperatures [42, 122, 123]. *Hu et al.* have used hydrothermal synthesis to form nano-hydroxyapatite on

a Ti substrate. Results showed that the amount of OH^- ions increased and the bonding strength of the formed nano-HA coating was higher than for HA coating made directly by HA suspension deposition [126]. Other studies show that during hydrothermal synthesis non-agglomerated crystals with homogenous grain size, shape and composition are obtained even at low temperatures [127]. However, the purity of the HA coating produced by hydrothermal synthesis method strongly depends on the purity of raw materials and synthesis conditions (concentration and pH values of solutions), in addition the coating deposition rate is many times slower compared to commercially used thermal spray process. As an alternative hydrothermal process as a post treatment for plasma sprayed coatings has showed good results [42, 128].

During the hydrothermal process the reaction atmosphere consists of vaporized water in the following equilibrium: $H_2O \leftrightarrows H^+ + OH^-$. The amount of H^+ and OH^- increases by increasing temperature [129]. The hydroxyl groups in atmosphere would presumably react with hydroxyl-deficient components converting them into crystalline HA phase through replenishment of hydroxyl ions.

Reheating ground HA coatings in air containing water vapour results in recrystallization of the glass phase and formation of HA at 600°C [82]. Heating the coating in the presence of water vapour can crystallize hydroxyapatite at 500°C [41]. Hydrothermal treatment in an autoclave at temperatures as low as 200°C can provide crystallization within the thermal spray coating structure [42]. *Weng et al.* found that plasma spraying HA powder on bulk ice produced no amorphous phase in the coating [130]. *Cao et al.* showed that the presence of water significantly increased the crystallinity of HA coating from 25 to 90%. In addition water molecules promoted transformation of unstable decomposition phases e.g. TTCP, TCP, CaO into more stable HA [107].

The extent of rehydration is more increased with temperature than with the immersion time. *Yoder et al.* also speculated that the movement of water molecules through the lattice channels of apatite might be driven by a proton transfer from water molecule to the neighboring hydroxide ion. This mechanism supports observation that OH^- concentration in carbonated and non-stoichiometric apatites increases as a function of temperature [30].

Yang et al. showed that increasing the hydrothermal heating time and temperature not only increased the crystallinity of HA coatings, but also decreased the amount of micro cracks on the surface through the dissolution – recrystallization process (Fig. 1.19). Reduction of microstructural defects due to a hydrothermal crystallization under an abundant saturated steam environment is referred to as a self-healing of HA coating [42].
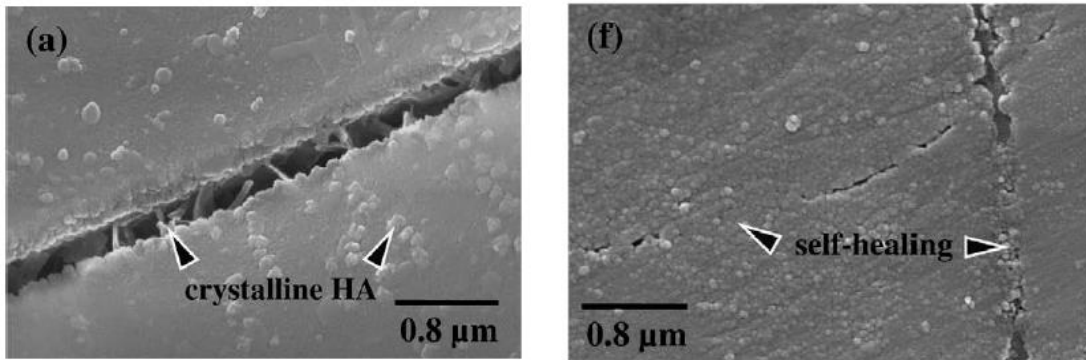
Fig. 1.19. Micrographs showing the self-healing of HA coating after a hydrothermal post treatment (modified from [42]).

The significantly improved bonding strength of hydrothermally crystallized HA coatings and enhanced coating/substrate adhesion due to the interfacial chemical bonding of OH⁻ ions allows better mechanical fixation and reliability of implants without dissociation problems [127]. In vivo study showed that due to the higher dissolution rate of the as-sprayed HA coating, granular particles dissociated from it and that resulted in lower extent of a new bone apposition compared to hydrothermally treated HA coating [128].

1.5.3 Polarization

Both bone and dentine show interesting electrical properties. Bone possesses not only piezoelectricity, the ability of generating electrical charge at the surface when stressed, but also a spontaneous dipolar electrical polarization due to its pyroelectric properties [131]. Streaming potential can also influence the electrical activity in bone [10]. Most recent studies have shown that the stored charge in bone is affected not only by total bone mass, but also by bone quality and structure [132]. Recently attention of the research has been oriented not only to mimic the bone chemistry and structure, but also to understand the surface properties of the biomaterial. Creating a surface charge on the HA biomaterial has become more and more popular, but the mechanisms of the conductor nature of hydroxyapatite is still not completely clear.

Because of the aligned hydroxyl ions in the columns along c-axis, HA has been described as a one dimensional conductor [10]. Ionic conductivity of HA has been explained by the existence of columns parallel to the c-axis. Polarization under an electrical

field is one of the most common methods to create a surface charge. During the polarization process OH⁻ are being organized in the structure by reorienting protons. Studies have shown that elevated temperature (at least 200 °C) and an electric field (even as low as 12 V/cm) is required [10, 133, 134], although some studies suggested that 350 – 450 °C is necessary for OH⁻ ions to receive enough thermal energy to reorient independently of their OH⁻ neighbors in the chain [135].

Two mechanisms for the creation of surface charge during the polarization process have been discussed:

1. ordering of OH⁻ in lattice by reorienting protons around O^{2-},
2. the migration of OH⁻ or H⁺ in the OH⁻ channel (ionic conduction).

Hitmi et al. suggested two steps for the reorientation of the OH⁻ direction. First, electrostatic repulsion between H⁺ and the closest Ca^{2+} ion would inhibit the rotation of the proton around O^{2-}. With increasing temperature, the fluctuations should make it possible to make 180° rotation that would put the H⁺ on the other side of Ca^{2+} triangle where electrostatic forces from the Ca^{2+} ions would tend to push it further away. At this moment a whole OH⁻ ion would come through the Ca^{2+} triangle and take a position essentially equivalent to the first but on the other side of the triangle [135]. The mechanism of the proton conduction is based on the proton vacancies in OH⁻ sites. In the influence of the temperature and electric field, proton would rotate around the O^{2-} ion and then migrate to the neighboring proton-vacancy site [136].

According to Nakamura et.al the proton conductivity of HA ceramics depends on the water vapor pressure of sintering atmosphere [136]. Some other studies have also shown that when the sintering atmosphere is water vapor, HA conductivity improves compered to samples sintered in air [137]. This is explained by the preservation of hydroxyl ions in the structure. Surface-bound water could also contribute to the conductivity of the material at temperatures below 200 °C [138].

Crystal orientation also affects the surface charge. HA is formed by two types of crystal planes with different atomic arrangements – a(b) planes with positively charged calcium ions, and c-planes which are rich with negatively charged phosphoric acid and hydroxyl ions [27]. Phosphate and hydroxide ions are all stacked above each other in hexagonal channels along the c-axis, where each hydroxide ion is coordinated to three surrounding calcium ions that lie in the same a(b)-plane. The c-plane is perpendicular to the hexagonal channels, whereas the a(b) plane has the hydroxide ion channels lying parallel to the surface and the surface is terminated by phosphate ions [27, 116, 139]. Increasing the amount of

a(b)-plane oriented crystals hydroxyapatites surface charge shifts from negative to positive and surface wettability decreases [111].

Different approaches have been used to induce and/or alter the surface charge of biomaterials to cause stimulation of new bone formation. Some of these methods are irradiation by focused electron beam [140], low-energy electrons [141], surface activation by plasma [142-144], electric polarized treatment in alkaline solution [145], coating with amino acids [146]. The most widely used method for creating a surface charge on apatites is polarization by placing the material between two electrodes which are connected to a power source. This system is placed in a furnace and heated until desired polarization temperature, dc electric field is applied and maintained for some time. The electric field is also maintained during the cooling phase (many references, for example [133, 136].

Different temperature, holding time and electric field values have been used for polarization of HA. Information about some of the studies are summarized in Table 1.5, including information about material type, polarization parameters and charge values. *Nakamura et al.* have shown that polarization at 300 °C has no effect on surface crystallinity, chemistry and morphology of HA coating. The study also showed that HA coating has higher stored charge values than HA ceramics. That could be explained with more defects in the coating that stimulate proton migration [147]. It is also reported that the grain boundaries are obstacles for proton migration during the polarization of dense HA [133].

Table 1.5.

Summary of some studies creating a surface charged hydroxyapatite bioceramics

Material	Polarization parameters	Charge measurement	Main conclusions	Reference
Dense HA ceramics (sintered at 1250 °C for 2 h in water vapor atmosphere)	T = 250-400 °C for 1h with dc field of 1 or 2 kV/cm	max current density: 7,87 nA/cm², max polarization charge: 14,9 μC/cm² (with 400°C, 1 kV/cm)	*) HA polarization is achieved by migration of protons in the OH⁻ channels *) Polarization charge of HA was 2 times larger compared to $BaTiO_3$	Nakamura et.al, 2001 [136]
Dense (98%) HA ceramics (sintered at 1250 °C for 2 h in water vapor atmosphere)	T = 300 °C for 1h with dc field of 1 kV/cm	max current density: 3,21 nA/cm², max polarization charge: 3,9 μC/cm²	*) Charged surfaces promoted bone reconstruction *) Surface with negative charge enhanced the osteobonding ability	Nakamura et.al, 2002 [148]
Pressed HA pellets sintered at 1200 °C for 2h and polished	T = 300 and 400 °C for 1h with dc field of 2 kV/cm	Max surface energy: 49.47 ± 3.76 mJ/m², max current density: 4,37 nA/cm², max stored charge: 4,28 μC/cm². contact angle of water: 65 ° for unpolarized HA, 59° for at 300 °C polarized HA, 47 ° for at 400 °C polarized HA	*) Increasing the surface charge increased the wettability and also the energy of HA surfaces *) Denser growth of cells with numerous cell–cell contacts was observed on negatively poled HA surface	Bodhak et.al, 2009 [149]
Compacted HA ceramic sintered at 1200 °C for 1-5 h in water vapor or air, TCP	T = 300 °C for 2min or 1h with dc field of 1 – 1000 V	dielectric constant: 30 for HA in air, 40 for HA in water vapor and <10 for TCP	*) Tests in SBF showed increased crystal growth for negatively polarized samples (even for polarization as week as 12 V/cm), no crystal growth was observed for positively charged surface *) Better results for sample sintered in water vapor compared to air *) Polarization treatment had no influence on TCP	Yamashita et.al, 1996 [133]

Material	Poling conditions	Measured values	Effect	Reference
HA coated Ti	T = 400 °C for 1h with dc field of 2 kV/cm	max current density: 1,19 nA/cm², max stored charge: 1,69 µC/cm².	*) Negatively poled surface accelerated mineralization process by selectively adsorbing Ca^{2+} ions, which promotes cell attachment and proliferation and faster cell differentiation, especially at early time points.	Bodhak et.al, 2010 [150]
Porous HA ceramics (interconnected porosity) and dense HA ceramics with one drilled hole	T = 400 °C for 1 h with dc field of 2 or 1,3 kV	polarization charge: 2,6 µC/cm² for dense HA and 13 µC/cm² for porous HA	*) Thickness of bonelike apatite layer formed in SBF was higher for polarized samples with negative surface charge	Iwasaki et.al 2008 [151]
HA dense pellets and porous (20-28%) HA	T = 400 °C for 1 h with dc field of 3 kV/cm	current density: 2,5 nA/cm² for dense HA, 10 nA/cm² for 20% porosity, 38 nA/cm² for 28% porosity	*) Depolarization current density increases with the level of porosity because of the high surface area to volume ratio	Gittings et.al, 2009 [137]
Porous HA scaffolds (80% connected porosity)	T = 400 °C with dc field of 3 kV/cm	not mentioned	*) Significantly more cells and increase in mineralized matrix on negatively charged surface was observed	Cartmell et.al, 2014 [152]
B-type carbonated apatite (CAp)	T = 350 °C for 30 in with dc field of 2 kV/cm	stored charge: 1,6 µC/cm² for HA, 4,3 µC/cm² for CAp with CO_3^{2-}/PO_4^{3-} molar ratio 1, 4300 µC/cm² for CAp with CO_3^{2-}/PO_4^{3-} molar ratio 5	*) Electrical conductivity and stored charge dramatically increased with increasing the carbonate ion content	Nagai et.al 2011 [153]
$Sr_5(PO_4)_3OH$ dense ceramics	T = 400 °C for 1 h with dc field of 2, 4, 10 kV/cm	current density: 2,6 nA/cm² with 2 kV/cm 106.3, nA/cm² with 10 kV/cm; stored charge: 60 µC/cm² with 2 kV/cm, 260 µC/cm² with 10kV/cm	*) Accelerated bone-like crystal growth on negatively charged surface *) On negative surface metallic cations in SBF are adsorbed faster, on positive surface anions are mainly adsorbed	Takeda et.al, 2002 [154]

Material	Method	Measurements	Findings	Reference
Biphasic calcium phosphate with HA and β-TCP	T = 400 °C for 1 h with dc field of 5 kV/cm	current density: 9,35 x 10^{-10} A/cm² for 75%HA, 5,72 x 10^{-10} A/cm² for 25%HA polarization charge: 2,38 µC/cm² for 75%HA, 1,11 µC/cm² for 25%HA	*) Stored charge was higher in composites with more HA phase *) Highest protein (bovine serum albumin) adsorption on the positively poled surfaces	Tarafader et.al, 2010 [155]
HA and HA/β-TCP (70/30) plates	T = 400 °C for 1h with dc field of 2 kV/cm	Average stored charge: 18,4 µC/cm² for HA/TCP plate, and 8,20 µC/cm² for HA plate	*) Good osteoconductivity for both HA and HA/TCP *) increased osteoblast activity for negatively polarized samples, decreased osteoclast activity on positively polarized plates.	Itoh et.al, 2006 [156]
Nano-crystaline HA thin films (330 nm)	irradiation by focused electron beam (electron energy 3 – 30 keV, electron beam current 1.4, 14 or 100 nA, irradiation time 70, 7 or 1 s)	Surface potential by Kelvin probe force microscopy: -0,6 - +0,1 V depending on the electron energy used	*) Materials with a designed and patterned surface potential can be obtained using irradiation by electron beam	Truchly et.al, 2013 [140]
HA coatings deposited on grade V Ti–6Al–4V alloy	HA coatings were activated by an air plasma (frequency of 22 kHz, output voltage 260 V)	contact angle: 35° for untreated HA coatings, less than 5° for plasma activated HA coatings	*) Greater cell attachment and adhesion on plasma-activated HA compared to untreated samples *) Atmospheric pressure plasma is a promising tool for modifying the biological function of a material without causing thermal damage	Tan et.al, 2012 [142]
Plasma sprayed HA coatings on Ti-6Al–4V alloy	Sample treatment with plasma electrolytic oxidation (PEO) method	contact angle: 43 – 67° for untreated HA coatings, 34 – 46° for PEO coatings	*) Collagen synthesis on PEO coatings was significantly higher than on the plasma sprayed coatings	Yeung et.al, 2013 [143]

Pressed HA pellets sintered at 1100 °C for 1h	sample treatment with low-energy electron irradiation in vacuum with excitation energy of 100 eV, electron current density of 100 nA/cm^2, exposure time 0 – 3000 s.	contact angle of distilled water: 10–100° changing exposition time from 0 to 3000 s. surface potential by Kelvin probe: around 0 V for hydrophilic HA (10°) and around 0,65 V for hydrophobic HA (100°)	*) DNA bound preferentially to the high wettability surface (<50 °), while hydrophobic interaction is the major determinant for protein adsorption *) Tailored hydrophilic and hydrophobic states remain stable at least for a month in different environment conditions (air and water)	Aronov, et.al, 2006 [141]
Plasma sprayed HA coating	activated by electric polarized treatment in 1 M NaOH solution at a dc voltage of 80 V for 3 min (PAS) or water vapor treatment with a pressure of 0.15 MPa at 125 °C for 6 h (WVT)	charges detected by the pH value change of SBF: 0,395 ± 0,058 for PAS and 0,190 ± 0,042 for WVT coating	*) PAS treatment created negative charge on the surface that improved bone-like apatite formation *) Animal experiments showed accelerated initial fixation for PAS coatings	Huang et.al, 2009 [145]

1.6 Effect of the hydroxyl ions and surface charge on the biological response of hydroxyapatite bioceramics

One of the most important parameters for successful bone implant material is its ability to promote effective osteogenic[3] differentiation. Extracellular and intercellular factors such as integrins, glycoproteins (e.g. fibronectin, vitronectin, osteopontin) and growth factors are important in influencing the adherence and differentiation of bone cells and development of bone in contact with HA material [157]. The commonly used methods to induce osteogenic differentiation include the use of growth factors (bone morphogenetic protein) and chemicals (e.g. dexamethasone) [158], but recently researchers have also been focusing on surface properties of a biomaterial. Alterations in the surface chemistry, composition, roughness, wettability and charge can influence cell response – adhesion, proliferation and differentiation.

The surface energy of the apatite influences the initial cell attachment and spreading of human osteoblastic cells at the surface and affects collagenous matrix deposition on the apatite. The enhancement of polar components on the surface of apatite may improve osteoblastic cell attachment and osteoconduction [10]. Previous studies show that HA bioceramics with an increased surface charge provides a benefit at all levels of the bone bonding process:

- improved bone-like apatite formation [156, 159]
- increased protein adsorption [141, 149, 160]
- stimulation of osteoconductivity [161]
- increased cell attachment, proliferation and metabolic activity [149, 150, 152]
- accelerated initial implant fixation [159, 162]

As already mentioned before the hydroxyl groups in apatite are important for creating a surface charge. Some research also shows their influence on the biological properties of material. HA coatings that have undergone hydrothermal post treatment showed higher extent of new bone apposition and lower dissolution rate compared to a traditional coating after 12 weeks of implantation [128]. *Pasteris et al.* have done a detailed study of biological apatites and have noticed that even a low-temperature (400 °C) heated natural bone that has a lot lower OH^- content than a synthetic apatite showed almost no resorption by osteoclasts. Although tooth enamel would benefit to have a high OH^- concentration and thus high buffering capacity to constantly attacking acids, lower OH^- amount in bone apatite would enable its dissolution ensuring a balance in osteoclast – osteoblast activity [16].

---

[3] derived from or composed of any tissue concerned in bone growth or repair

Substitutions in hydroxyapatite structure also influence the surface charge, hence the biological response. It was found that the polar interaction energy of HA with water was significantly decreased after carbonation. Carbonated apatite showed lower cell attachment and collagen production compared to HA. Nevertheless the results showed no significant difference in terms of cell growth indicating that the poor affinity of the carbonated apatite surface only induced a delay in the initial cell attachment not a change in cell growth or differentiation [163]. Contrary, silicon inclusion in apatite structure increased surface hydrophilicity and electronegativity. In vitro results showed larger expression of more alkaline phosphatase, type 1 collagen and osteocalcin, as well as this surface enhanced cell attachment and proliferation [164].

The increase in surface roughness appears to favor osteoblast activity and material integration. *Wanlei et al.* observed that surfaces with average roughness (Ra) values 0.77 – 1.09 μm show optimal promotion of osteogenic differentiation that is concluded from the results of osteoblast cell attachment, spreading and F-actin arrangement [165]. *Costa-Rodrigues et al.* showed that higher surface roughness favors also osteoclast adhesion, although it could limit cellular mobility [166]. Numerous studies have shown the importance of surface topography and geometry of the substrate to control and induce the osteogenic phenotype in mesenchymal stem cells [167]. A recent study connects surface roughness measurements with differences in surface charge values showing that surface potential is larger on rougher surface [168].

Zhuang et al. have showed that the attachment of osteoblast-like cells decreases with increasing a(b)-plane orientation degree in hydroxyapatite ceramics. As a general trend, initial osteoblast attachment is greatly enhanced on a more wettable (negative) surface, because a high-energy surface will improve cell attachment and spreading [111, 164]. Other studies also show the importance of crystal orientation on the adsorption of acidic or basic proteins. Surface properties of biomaterials are the main factor that determines the protein adhesion as the interactions between proteins and surface of material are mainly energetic – van der Waals, electrostatic, hydrogen bonding, hydrophobic interactions [146]. The adsorption of negatively charged bovine serum albumin was greater on a fiber-like HA particles compared to a plate like HA particles, a reverse order was observed for lysozyme (positively charged protein) [27]. Rod shaped HA particles with large a-plane area and mesoporous structure exhibit positive surface charge and show high-drug loading capacity and drug release properties for the negatively charged bovine serum albumin [121]. The (010) surface with the hydroxyl channels lying parallel to the surface has been found to interact more strongly with some negatively charged

species than (001) crystal alignment. In spite of this, (010) is thermodynamically less stable than the (001) plane. [169].

Rohanizadeh et al. have also discovered that the adsorption of proteins was dependent on the crystallinity and total surface area of HA although the electrostatic forces between proteins and HA surface influenced the protein adsorption to a higher extent compared to the crystallinity and total surface area [146].

Previous studies show that polarized HA surface enhance mineral deposition in simulated body fluid and osteoconductive capabilities in vivo. It has also shown to enhance the blood vessel regeneration of a vascularly injured model [170], and polarized hydroxyapatite in silk fibroin gel enhanced epidermal recovery from skin wounds in vivo [171]. Positively charged HA nanoparticles have shown the ability to induce the aggregation of the red blood cells, that could be attributed to the bridging force through the electrostatic interaction between positively charged HA and negatively charged groups on the surface of red blood cells [172].

It has been observed that the use of electric fields results in a positive effect by reducing the number of viable bacteria that make up the biofilms [173]. Based on this result it can be concluded that biomaterials with enhanced surface charge might have an antimicrobial effect by preventing or decreasing biofilm formation, increasing disintegration or enhancing the action of antimicrobial agents [174].

Brief summary about a material type, surface charge and resultant biological response is included in Table 1.5 (previous section). Results show that surface charge depends on the material chemistry, structure, preparation conditions etc. Lack of the detailed material characterization and diverse and variable biological parameters are the main reason why there are problems with developing a clear model about the bone cells response on the surface charge. Despite the different and sometimes disputed results most of the studies show that charged surface (negatively or positively) significantly increase the bone cell response compared to un-polarized surface [147].

1.7. Summary of the literature review

Looking at bone at its molecular level it has been shown that the main mineral component of bone is hydroxyapatite ($Ca_{10}(PO_4)_6(OH)_2$). This knowledge makes it very attractive to bone substitute researchers. HA as a bone implant material has been studied for many decades, but as for a very complex system, its full potential has not been discovered yet.

The structure of HA supports many different variations in form of substitutions, inclusions, defects etc. which makes it possible to vary HA properties in a wide range. Hydroxyl ions in the HA structure are placed in 0.30 – 0.35 wide channels along c-axis, usually organized as …O-H O-H O-H… columns, and they enable thermal stability of stoichiometric HA even until 1400 °C, improve the structure and surface properties of HA coatings and might even have a positive effect on the biological response of HA biomaterials. But the amount of OH$^-$ in HA is not constant and can change in a wide range: while stoichiometric HA has 100% OH$^-$ in its structure, oxyapatite contains no hydroxyl ions. The main reasons that influence the amount of OH$^-$ in HA are ion substitution or incorporation in the structure, crystallite size, and thermal treatment.

For full characterization of apatite, a measurement of two atomic ratios is required: Ca/P and OH/P, however mostly only the Ca/P ratio is considered. Main reason for that is the lack of easy-to-use method for determination of OH$^-$ content. There have been attempts to quantify the OH$^-$ in apatite by different techniques, but the poor explanations of the use of the method, long and complicated procedures, or not easily accessible equipment are the main reasons why the amount of hydroxyl ions is being rarely described. Chemical analysis for the determination of OH$^-$ are very long and complicated, also they can not be used with a sufficient accuracy, that is why physical techniques are more attractive. Nuclear magnetic resonance is being used to detect the hydroxyl ions in biological apatites, but this method has been described as time consuming and there might be difficulty to distinguish between signals arising from OH$^-$ and water. Several other less traditional methods as X-ray photoelectron spectroscopy, secondary ion mass spectrometry, elastic recoil detection etc. have also been used, but in order to develop a method that is easy to access and easy to use, in this study conventional methods as thermal analysis, Fourier transform infrared and Raman spectroscopy were chosen.

Thermal gravimetric analysis can indicate the OH$^-$ ion concentration from water loss by heating hydroxyapatite or in a thermal reaction that encourages release of water at lower temperatures. Spectroscopy allow to directly identify the presence of OH$^-$ from the absorption or vibration line. Quantitative analysis requires a calibration curve made from samples with known OH$^-$ content. This requires a sample with the maximum possible OH$^-$ content and another sample without OH$^-$.

Because of the low mechanical properties of hydroxyapatite, it can not be used as a load bearing implant, but it is widely used as a coating on metal (usually Co-Cr alloys or Ti and its alloys) implants. Thermal sprayed HA coatings are widely used in commercial applications, but

due to the high temperature, OH^- depletion, amorphous phase formation or even partial decomposition can occur. It results in higher dissolution rate and may lead to decrease in the microstructural homogeneity, and poorer mechanical properties. In order to improve the bioactivity various post treatments have been studied. Hydrothermal process not only restores the depleted hydroxyl ions, but also improves crystallinity, decreases the amount of unstable decomposition phases and improves microstructure of the coating. It has also been shown that the surface charge has improved implant fixation by promoting protein adhesion and increased cell activity thereby forming more bone.

This study investigated the role of hydroxyl ion concentration of hydroxyapatite coating on the primary human derived osteoblast adhesion, proliferation and bone-related gene expressions. In order to maximize the influence of hydroxyl ions and exclude interference of some random effects, all coatings were designed to have the highest level of structural order: crystals were aligned during the production of coatings, and OH^- were oriented by polarization.

2. MATERIALS AND METHODS

2.1. PART 1 Measurement of the hydroxyl ion content in hydroxyapatite

2.1.1. Sample preparation

2.1.1.1. Synthesis of hydroxyapatite

Hydroxyapatite powder was prepared in using wet chemical precipitation method by neutralizing a calcium nitrate solution ($Ca(NO_3)_2$) with ammonium hydrogen phosphate solution (($NH_4)_2HPO_4$) and ammonium hydroxide solution (NH_4OH). The reaction can be described by following equation:

$$10Ca(NO_3)_2+6(NH_4)_2HPO_4+2NH_4OH \rightarrow Ca_{10}(PO_4)_6(OH)_2+14NH_3+10H_2O+20NO_2$$
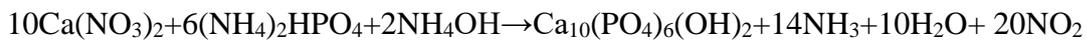
The calcium nitrate solution was prepared by dissolving 75 g $Ca(NO_3)_2 \cdot 4H_2O$ (*Sigma Aldrich*) into 400 ml deionized water and heated until boiling. The phosphate solution was prepared by dissolving 25,4 g $(NH_4)_2HPO_4$ (*Sigma Aldrich*) into 150 ml deionized water, and 30 ml of 30% NH_4OH (*Sigma Aldrich*) solution and then added dropwise into the calcium solution. The reaction media was continuously mixed during the reaction and then for another 30 minutes after the addition of all the phosphate solution. The resulting precipitate was then washed with deionized water, filtered and placed in freeze-dryer (*Alpha 2-4 LD, Martin Christ*) operated at -90 °C for 48 hrs. The synthesized apatite powder was heated at 1000 °C for 15 h in water vapor to provide a high concentration of hydroxyl ions. Hereafter the heat-treated hydroxyapatite powder is referred as the "standard hydroxyapatite".

2.1.1.2. Preparation of hydroxyapatite/ fluorapatite mechanical mixtures

Standard hydroxyapatite and commercial fluorapatite (*Sulzer Metco*) was used to prepare mechanical mixtures. Samples were weighted (*ABS 120-4, Kern & Sohn GmbH*) to an accuracy of ± 0,0001 g and mixed in a mortar for about 15 - 20 min to obtain an intimate mixture. HA/FA mixtures with the HA phase of 25, 50 and 75 weight% were prepared.

2.1.1.3. Preparation of oxyhydroxyapatites

In order to remove hydroxyl ions from the structure standard hydroxyapatite was heat treated in vacuum (1,3 x 10^{-4} Pa) at 1000 °C for 20 or 43 hours. A sorption pump (*Leybold-Heraeus*) was used to provide high vacuum level in a closed quartz system, cylindrical furnace (*LabEc*) was used for heating. Samples were prepared in custom made quartz ampules which were flame-cut and fused off the system after the heating process while still at 1000 °C (Fig.

2.1). In this way sample was protected from any influence from the atmosphere. Ampule was opened after the sample was completely cooled down.

Fig. 2.1. Oxyhydroxyapatite powder in a custom made quartz ampule.

To prepare samples with different amounts of hydroxyl ions, rehydroxylation of oxyhydroxyapatite produced in vacuum at 1000 °C for 43 h was performed. Thermal gravimetric equipment (*Setaram, Setsys Evolution*) with a setup of 90% humidity and gas flow of 10 ml/min was used. 90 mg of sample was put in a Pt crucible and heated until 350, 400 or 700 °C with a heating rate of 5 °/min. Holding time at maximum temperature was 30 minutes for 350, 400 and 700 °C and 1 h for 400 °C.

2.1.2. Physico-chemical characterization techniques of hydroxyapatite

2.1.2.1. Inductively coupled plasma mass spectrometry

Microelements in the hydroxyapatite were detected using *PerkinElmer SCIEX ELAN DRC-e ICP-MS*. Argon with a purity of 99.999% was used as a carrier gas. The sample (0.3 g) was digested in an oxidizing acidic medium using 65% nitric acid (*Merck*) and 30% hydrogen peroxide (*Merck*). For homogenization, an ultrasonic bath (*Sonorex RK100*) was used. Remineralization was carried out in a closed vessel microwave digestion system (*Anton Paar 300*). A total of 5 replicates were taken and averaged.

2.1.2.2. Determination of calcium and phosphorous content

Calcium was determined by atomic absorption spectroscopy with a *contra 300* (*AnalytikJena*) spectrophotometer at 442 nm wavelength. Phosphorous was determined as the phosphovanadomolybdate complex with a *UV-1800* (*Shimadzu*) spectrophotometer using a wavelength of 460 cm^{-1}. 6 replicate samples were used and averaged.

2.1.2.3. X-ray diffraction

Powder X-ray diffraction patterns were recorded on a *D8 Advance diffractometer (Brücker)* using Cu K$_\alpha$ radiation (λ = 1.54 Å) at 40 kV voltage and 40 mA current passing through a K$_\beta$ Ni-filter (0,020 mm). The diffracted intensity was recorded over a $10 - 60^0$ diffraction angle range (2θ) with a scanning step of 0.02^0 on a position sensitive detector. All samples were ground with a mortar and pestle before measurement. Crystalline phases were identified using ICDD (International Centre for Diffraction Data) diffraction patterns from pure phases.

For investigation of small quantities of a material X-ray diffractometer *SmarLab* (*Rigaku*) equipped with 9 kW Cu rotating anode X-ray tube, and a polycapillary optics was used. Samples after thermal gravimetric analysis was analyzed with this equipment.

2.1.2.4. Fourier transform infrared spectroscopy

A *Nicolet Is50* (*Thermo Fisher Scientific*) was used to determine functional groups in the standard hydroxyapatite, samples after thermal gravimetric analysis and oxyhydroxyapatite samples.

A *Frontier FT-IR/FIR Spectrometer (Perkin Elmer)* was used to determine functional groups in the fluorapatite, mechanical mixtures of HA and FA, HA with paraffin oil sample preparation method, and some of the oxyhydroxyapatite samples (for the comparison of different equipment).

In all cases samples were prepared identically: 1) small amount (about 2 mg) of the sample was ground in a mortar, 2) 200 mg of KBr (*Uvasol®, Merck*) was added to the ground sample and lightly mixed (no grinding) to form a homogeneous mixture, 3) pellet was made by uniaxial pressing of the mixture. For the analysis with paraffin oil: 1) sample was ground in mortar, 2) a drop of paraffin oil *Nujol* (*Sigma Aldrich*) was added to the ground sample and mixed together, 3) the slurry was placed between two KBr discs for analysis.

Spectra were taken over a $400 - 4000$ cm^{-1} range at a resolution of 4 cm^{-1}. A total of 64 scans were taken and then averaged. At least 3 KBr pellets for each sample were prepared and measured.

2.1.2.5. Raman spectroscopy

Raman spectra of standard hydroxyapatite and oxyhydroxyapatite samples over $400 - 4000$ cm^{-1} range was collected on an *inVia* micro-Raman spectrometer (*Renishaw*) after irradiation with a 514.5 nm laser at 10% (for standard HA) or 100% (for oxyhydroxyapatite samples) laser

power through a 5x objective. The signal was collected for 10 seconds, the measurement repeated 3 times, and the average determined to identify the vibrational lines. Each sample in at least three different places was measured.

2.1.3. Quantitative measurement of hydroxyl ion content in hydroxyapatite

2.1.3.1. Thermal gravimetric analysis

Thermal analysis was investigated for measuring the OH^- content by three different thermal reactions involving a loss of hydroxide ions from the apatite structure and consequent release of water:

1. Heating HA powder until decomposition to tetracalcium phosphate ($Ca_4(PO_4)_2O$; TTCP) and tricalcium phosphate ($Ca_3(PO_4)_2$; TCP) according to the following reaction:

$$Ca_{10}(PO_4)_6(OH)_2 \rightarrow 2Ca_3(PO_4)_2 + Ca_4(PO_4)_2O + H_2O$$
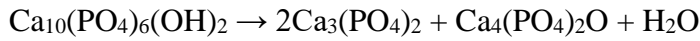
2. Heating HA with calcium pyrophosphate (made from dicalcium phosphate dihydrate by heating at University of Toulouse) to produce tricalcium phosphate as per the following reaction:

$$Ca_{10}(PO_4)_6(OH)_2 + Ca_2P_2O_7 \rightarrow 4Ca_3(PO_4)_2 + H_2O$$

3. Heating HA with calcium fluoride (*Sigma Aldrich*) to replace hydroxyl ions with fluoride to produce fluorapatite ($Ca_{10}(PO_4)_6F_2$; FA) according the following reaction:

$$Ca_{10}(PO_4)_6(OH)_2 + CaF_2 \rightarrow Ca_{10}(PO_4)_6F_2 + CaO + H_2O$$
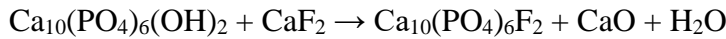
For the mechanical mixtures samples were weighted to an accuracy of $\pm 0,0001$ g and mixed in a mortar for about 15 - 20 min to obtain an intimate mixture. To ensure complete reaction CaF_2 and $Ca_2P_2O_7$ was used in excess (e.g. for 100 mg HA 30 mg of CPP was taken, and for 100 mg HA 10 mg CaF_2 was taken). More detailed information about the mechanical mixtures including the weighted mass of the samples and repeated reactions are shown in Appendix 1.

Mass loss was measured from a 100 mg sample in Pt crucible during heating up to 1200 $^{o-r}$ 1500°C at a rate of 10 °/min in Ar flowing at 20 ml/min. *Setaram* (*Setsys Evolution*) thermal gravimetric equipment was used. Thermal reactions were repeated at least three times to determine the standard deviation of the measurement.

The amount of hydroxyl ions was calculated according to formula:

$$OH^-(\%) = \frac{mass\ loss\ of\ OH^- \times M_{HA}}{M_{OH}}$$

where mass loss of OH^- was obtained from TGA curve, M_{HA} was a molar mass of hydroxyapatite, and M_{OH} is molar mass of hydroxyl ions.

2.1.3.2. Fourier transform infrared and Raman spectroscopy

FTIR spectroscopy (for hydroxyapatite/ fluorapatite mechanical mixtures and oxyhydroxyapatite samples) and Raman spectroscopy (for oxyhydroxyapatite samples) were used to determine the concentration of hydroxyl ions in the apatite structure. Three approaches were used for the measuring the ratio of OH^- and PO_4^{3-} peak area:

1. Area of the OH^- peak at 3570 cm^{-1} and area of the ν_1 PO_4^{3-} peak at 964 cm^{-1} was measured using *SpectraGryph* software. Spectra background correction was done with the same software.

   a. for FTIR spectra OH^- peak area was measured between 3596 and 3541 cm^{-1} and PO_4^{3-} peak area was measured between 800 and 1300 cm^{-1}. In this case, all absorption bands from both ν_1 and ν_3 PO_4 modes were included in the calculations

   b. for Raman spectra OH^- peak area was measured between 3590 and 3560 cm^{-1} and ν_1 PO_4^{3-} peak area was measured between 990 and 920 cm^{-1}.

2. Deconvolution of the spectral range between 500 and 700 cm^{-1} was performed using *MagicPlotStudent* software (for FTIR spectra), and area of the OH^- absorption peak at 632 cm^{-1} and ν_4 PO_4^{3-} absorption peaks were measured. Spectra background correction was done with the same software.

The ratio OH/PO_4 was calculated for all samples and compared with the OH/PO_4 ratio for standard HA. Three to six replicates for each sample were measured and standard deviation was calculated.

2.2. PART 2 Influence of hydroxyl ion content on the biological response of hydroxyapatite coatings

2.2.1. Coating prepartion

2.2.1.1. HA coating preparation by flame spray process

The HA powder (*Captal®30, Plasma Biotal Limited*, particle size of 20 – 40 µm) was delivered from the powder feeder (*Metco 4MP-Dual, Perkin Elmer*) into a flame spray torch (*Casto DynDS 800*) operated using acetylene and oxygen for the flame, and air as a carrier gas. Commercially pure (grade 1) titanium substrates (grit blasted with Al_2O_3) were positioned 12 cm from the torch and preheated to 250 °C. Melted particles from the torch produced round splats on the preheated titanium, and ensured crystal alignment.

The shape and size of the HA coating was chosen suitable for biological testing. Ten coupon-like coatings were produced at the same time using a sample holder shown in Fig. 2.2. Titanium plate (thickness 1 mm) was laser-cut to make 12 mm diameter discs which were still holding to the plate. For the spraying procedure this substrate was attached to the metal sample holder with screws. In this way all surface of the round samples was sprayed. After spraying the coated HA coupons were cut out using a pliers.
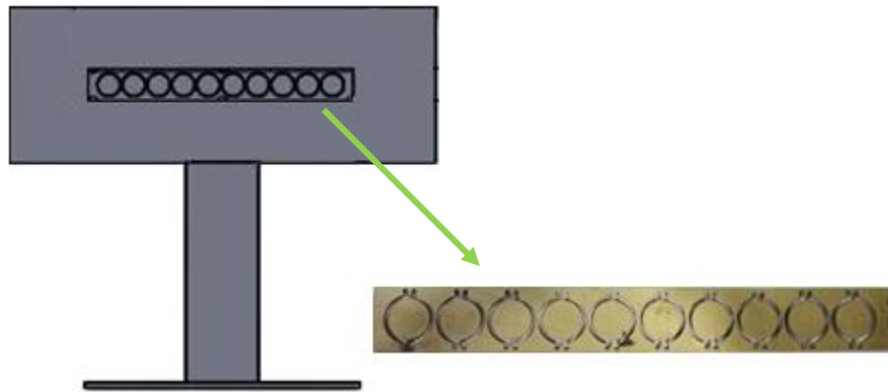
Fig. 2.2. A schematic model of the sample holder for spraying procedure and a photo of a substrate.

2.2.1.2. Hydrothermal treatment of HA coatings

Half of the HA coatings were subjected to hydrothermal post-treatment in water vapour for 20 h at 200 °C. Temperature and time was chosen based on the previous results (unpublished, partly presented in *the International Symposium on Apatite and Correlative Biomaterials, France, 2013*).

The pressure vessel used for the experiments are shown in Fig. 2.3. A special sample rack was made which allowed to process eleven samples at a time. After the hydrothermal processing samples were dried in an oven (*Venti-Line, VWR*) at 120 °C for 2 h. In total 25 samples were hydrothermally processed.

Fig. 2.3. Pressure vessel and a sample rack used for the hydrothermal treatment of HA coatings.

2.2.1.3. Polarization of HA coatings

To ensure the alignment of hydroxyl ions all coatings were polarized in a strong electric field (5 kV/cm) at 400 °C for 3 h. Polarization parameters were chosen based on the literature analysis. Heating rate of 10 °C/min was used and the electric field was maintained also during the cooling process.

Electric field is created by two parallel stainless steel electrodes to which voltage that is equal to 2 kV is applied (*H.V. Power supply N 1130-4, Wenzel-Elektronik*). Distance between the two electrodes is fixed to be 5 mm by placing silica cylinders in between. Voltage is supplied by vires inserted in ceramic insulators. The whole assembly is then placed inside electric furnace (*Keramserviss*) like shown in Fig 2.4. Samples are put in between the two electrodes. Thickness of the titanium substrate is 1 mm therefore the distance between the coating and the top electrode is 4 mm. In total 50 samples were polarized.
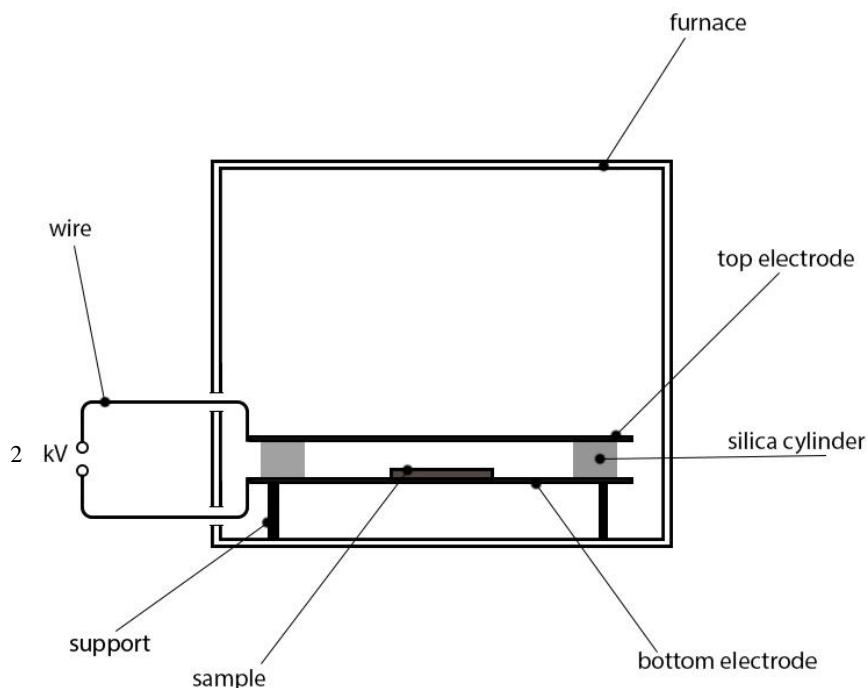
Figure 2.4 Scheme of the polarization system

2.2.2. Physico-chemical characterization techniques of HA coatings

2.2.2.1. X-ray diffraction

X-ray diffraction patterns were recorded on a *D8 Advance diffractometer (Brücker)* using Cu K_α radiation ($\lambda = 1.54$ Å) at 40 kV voltage and 40 mA current passing through a K_β Ni-filter (0,020 mm). The diffracted intensity was recorded over a $10 - 60^0$ diffraction angle range (2θ) with a scanning step of 0.02^0 on a position sensitive detector.

Phase analysis was done for the commercial HA powder, as-sprayed coatings and from the substrate peeled and crushed coatings. The powder and peeled coatings were ground with a mortar and pestle before measurement. Crystalline phases were identified using ICDD diffraction patterns from pure phases.

2.2.2.2. Fourier transform infrared spectroscopy

A *Frontier FT-IR/FIR Spectrometer (Perkin Elmer)* was used to determine functional groups in the commercial powder and coatings. Spectra were taken over a $400 - 4000$ cm^{-1} range at a resolution of 4 cm^{-1}. A total of 64 scans were taken and then averaged. Sample preparation technique with KBr was used (described in Section 2.1.2.3).

For the calculation of OH$^-$ amount deconvolution of the spectral range between 500 and 700 cm^{-1} was performed using *MagicPlotStudent* software, and area of the OH$^-$ absorption peak at

632 cm^{-1} and ν_4 PO$_4^{3-}$ absorption peaks were measured. Spectra background correction was done with the same software. The ratio OH/PO$_4$ was calculated for all samples and compared with the OH/PO$_4$ ratio for standard HA.

2.2.2.3. Kelvin Probe Atomic force microscopy

Atomic force microscope (*Solver-Pro NT-MDT, AFM*) with Kelvin probe force microscopy function was used for measuring surface electrical potential. Surface electric potential is being detected by the curvature of the cantilever when it is deformed by the electrostatic forces that occur between the scanning needle and the sample surface. Platinum coated chip (*NSG01/Pt, NT-MDT*) and semi-contact method was used. Ten measurements for each sample were carried out and the average values were calculated.

2.2.2.4. Scanning elecetron microscopy

Microstructure of HA coatings was observed using a scanning electron microscope (*Philips XL 30, SEM*) at a 10 kV acceleration voltage. Secondary electron detector was used. Samples before imaging were sputter coated with platinum.

2.2.2.5. Profilometry

Surface roughness measurements were performed with a *Talysurf Intra 50* stylus type profilometer (*Taylor Hobson*). Stylus Arm 112/2009 with a tip radius 2μm, measurement speed of 0,5 mm/s, data length (x and y) of 3 mm and 400 points was used. 3D roughness measurements were determined levelling the surface to correct positioning inaccuracy, and filtering the waviness and roughness using the Gaussian filter with a 0.8 mm cut-off according to standard ISO 25178.

2.2.3. Biological in-vitro testing

2.2.3.1. Cell culture

In-vitro study involved 3 donors of normal human bone-derived osteoblasts (passage 4) cultured on HA coatings for 1 day, 1 week and 2 weeks. Osteoblasts were obtained from normal patients during joint replacement surgery or bone fragments were isolated from bone marrow aspirates obtained from iliac crest biopsy of normal volunteers at the Royal Adelaide Hospital, Australia. Detailed procedure of separating a single-cell suspension is described by *Atkins et.al* [175]. All samples were sterilized with ethylene oxide, placed in 24-well plates (*Corning*

Incorporated) and seeded at a cell concentration of $2x10^4$ cells/well. 500 µl of proliferation media was used in each well. Proliferation media consists of α-MEM (Minimum Essential Medium, *Sigma Aldrich*) with added 1% HEPES (4-(2-hydroxyethyl)-1-piperazineethanesulfonic acid, *Media Production*), 1% Penicillin/ Streptomycin (*Thermo Fischer Scientific*), 1% L-Glutamine (*Novachem*) and 10% FBS (Fetal Bovine Serum, *Thermotrace*). Media was changed every 3 days. All samples were incubated at 37 °C in an atmosphere of 5% CO_2.

This study was approved by the University of Adelaide Human Ethics Committee (H-35-2001) and informed consent was obtained from all patients in accordance with the Declaration of Helsinki.

2.2.3.2. Scanning electron microscopy and cell coverage calculations

Cell morphology, attachment, growth and spreading on a material were assessed by SEM imaging after 1 and 14 day incubation. All samples for SEM observation were fixed with 4% paraformaldehyde/ 1.25% glutaraldehyde with 4% sucrose solution. Post-fixation was performed with 2% osmium tetroxide for 30 min at room temperature. Fixed samples were then dehydrated in an ethanol series (1 time for 70% and 90%, and 3 times for 100%) followed by a hexamethyldisilazane drying procedure. Then samples were sputter coated with platinum and examined with a scanning electron microscope (*Philips XL 30*) at a 10 kV acceleration voltage.

Five representative images were taken for each material at 200x magnification and quantified. Photoshop software was used to trace all cells with a pencil tool, and Image J analysis software was used to calculate the difference between the colored and uncolored area. The area of cells (in % from the total area) for each sample was determined. Standard error from 15 images per sample (3 donors, 5 images per donor) was calculated.

2.2.3.3. Confocal microscopy and cell counts

To visualize nuclei and the actin cytoskeleton samples were subjected to staining with 4',6-diamidino-2-phenylindole (DAPI) and phalloidin after incubation for 1 and 14 days. After incubation the cells were washed with phosphate-buffered saline (PBS). Fixation and permeation were done with 4% paraformaldehyde and 0.1% Triton X-100 (*The Rohm & Haas Company*), respectively. Methanolic stock (*Ajax Finder*) was then added and stained for 30 min at room temperature, followed by the addition of DAPI (*Sigma*). The samples were then fixed on the slide using an anti-fade mounting media (*Life Technologies*). The cellular morphology

was observed using a confocal microscope (*Leica TCS SP5*). The confocal microscope was chosen as this can measure greater vertical distances as an atomic force microscope. It can be used to scan through the material to find the Z increment below and above the surface. A z-series was taken between these two points in steps of 0.4 μm.

Fifteen representative images were taken for each material (3 donors, 5 images per donor) and the number of cells identified by DAPI were counted manually. Standard error from the results obtained was calculated.

2.2.3.4. Real-time polymerase chain reaction

Ribonucleic acid (RNA) was extracted from cells grown on the material at two time points throughout the cell culture (day 7 and 14) using TRIzol (*Ambion Life Technologies*). Reverse transcription was carried out using a Corbett real-time polymerase chain reaction (PCR) machine (*Rotor Gene RG-3000, Corbett Life Science*) with random hexamer primer (GeneWorks) and SuperScript III reverse transcriptase (*Invitrogen*) according to the manufacturer's instructions to produce double-stranded deoxyribonucleic acid (cDNA).

Quantitative real-time PCR was performed to compare expression levels of cDNA for specific osteoblast genes in cells grown on the HA coatings. Glyceraldehyde-3-phosphate dehydrogenase (GAPDH) was used as a housekeeping gene to allow comparison of the data and normalize the expression values of the target genes. for each of the genes. Expression of the specific genes encoding osteoblast-related proteins - collagen type I (Col1a1), runt-related transcription factor 2 (RUNx2), osteocalcin (OCN) and osteopontin (OPN) - was compared between the different samples. Statistical analysis of data was performed using the *Graph Pad Prism 6* software, statistical significance was determined by unpaired t-test. All data were collected in independent triplicate experiments and the mean values and standard errors were calculated.

3. RESULTS AND DISCUSSION

3.1. PART 1 Measurement of the hydroxyl ion content in hydroxyapatite

3.1.1. Preparation of the standard hydroxyapatite

To measure hydroxyl ion concentration a standard hydroxyapatite is required. A wet chemical precipitation method was used to obtain HA because of its simplicity, relatively inexpensive raw materials, good repeatability, and accessibility to equipment. The main synthesis parameters which influence the composition of the resulting powder are Ca/P molar ratio and the drop rate of reactants. Even slight differences in the Ca/P molar ratio may change the composition and thereby the properties of hydroxyapatite [176, 177]. Some studies have shown that OH^- content in HA is directly influenced by synthesis parameters. Initial pH values influence the balance of ions in the solution. For the precipitation of HA high concentration of OH^- in solution is necessary [178].

The process was firstly chosen to establish a structure that could accommodate hydroxyl ions. This required:

      a) the absence of impurities,

      b) a pure apatite without accompanying decomposition phases (a Ca/P ratio of 1.67),

      c) the absence of carbonate,

      d) structural order within the apatite phase.

Firstly, analytical grade reagents were chosen to avoid inclusion of unnecessary cations. Secondly, particular care was directed to preventing calcium deficiency – stoichiometric calcium and phosphate amounts were used and high pH during the reaction was maintained. Thirdly, a high wet synthesis reaction temperature prevented carbonate inclusion, thereby allocating crystallographic sites for hydroxyl ion inclusion. Increase of the suspension temperature decreases the solubility of CO_2 in the water and consequently decreases the carbonate included in the apatite. Finally, high reaction temperature also increased the crystal size and the structural order, thereby establishing crystallographic sites for a more defect-free structure. Based on previous studies it is expected that hydroxyapatite will include more hydroxyl ions in its structure when synthesis is caried out in higher temperature, because with temperature the order of structure increases [16]. These conditions established an apatite lattice that needed maximum OH^- filling.

As for further studies highly crystalline hydroxyapatite is needed, as-synthesized powder was heat treated in 1000 ^{0}C for 15 hours. Previous results show that there are several types of

water binding in the apatite – physically and chemically adsorbed and structural water in the form of OH⁻ ions. Adsorbed water is removed under 360⁰C, but higher temperatures (from 1000 ⁰C) cause dehydroxylation from HA [43]. To prepare standard hydroxyapatite with maximum quantity of hydroxyl groups in its structure, water vapor was directly supplied into the furnace during heating. Previous experiments showed that heating environment (water vapor), temperature (1000 °C) and time (15 h) chosen are suitable and sufficient to prepare crystalline and well hydroxylated hydroxyapatite [57]. Hereafter the heat-treated hydroxyapatite is referred as the 'standard hydroxyapatite'.

To determine the phase composition of the standard hydroxyapatite, X-ray diffraction was used. The results showed highly crystalline apatite – according to ICDD database all diffraction maximums corresponded to hydroxyapatite phase (Fig. 3.1).
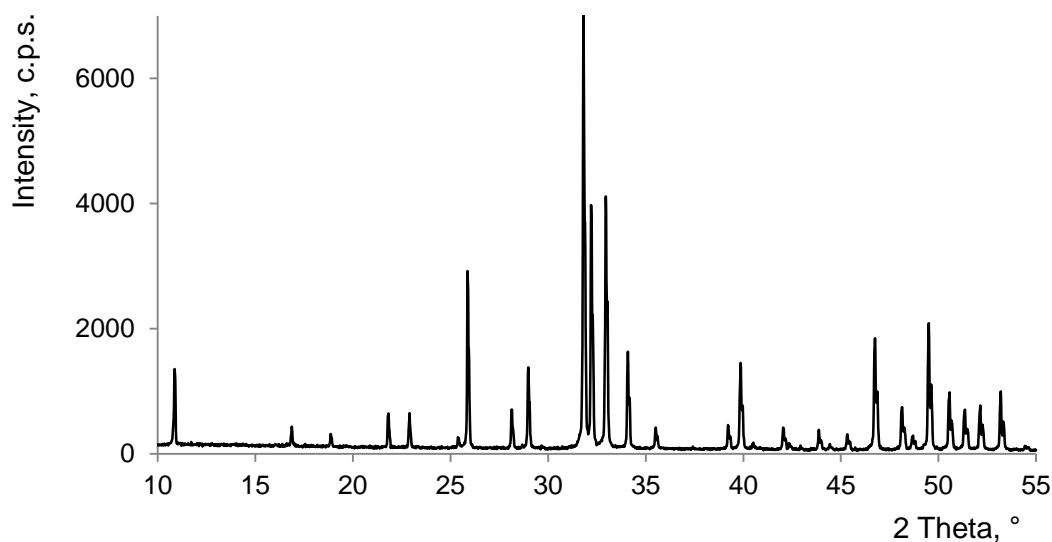
Fig. 3.1. XRD pattern of the standard hydroxyapatite.

The structure of obtained HA was also studied with FTIR spectroscopy. All vibrations of functional groups displayed in the spectra were characteristic to hydroxyapatite phase (Fig. 3.2). Spectra showed a clear hydroxyl vibration peak, at both 631 cm⁻¹ and 3573 cm⁻¹. The second peak was located on a broad band between 2800 cm⁻¹ and 3600 cm⁻¹, representing asymmetrical and symmetrical stretching vibrations of adsorbed water. The most intense absorption bands of hydroxyapatite were situated at 1043 cm⁻¹ and 1090 cm⁻¹, corresponding to the asymmetric stretching modes of PO_4^{3-}, while the peaks at 962 and 472 cm⁻¹ derived from the symmetric stretching and bending mode of PO_4^{3-}, respectively. The two very sharp and separated peaks at 601 and 573 cm⁻¹ represented the bending mode of the phosphate group.

70
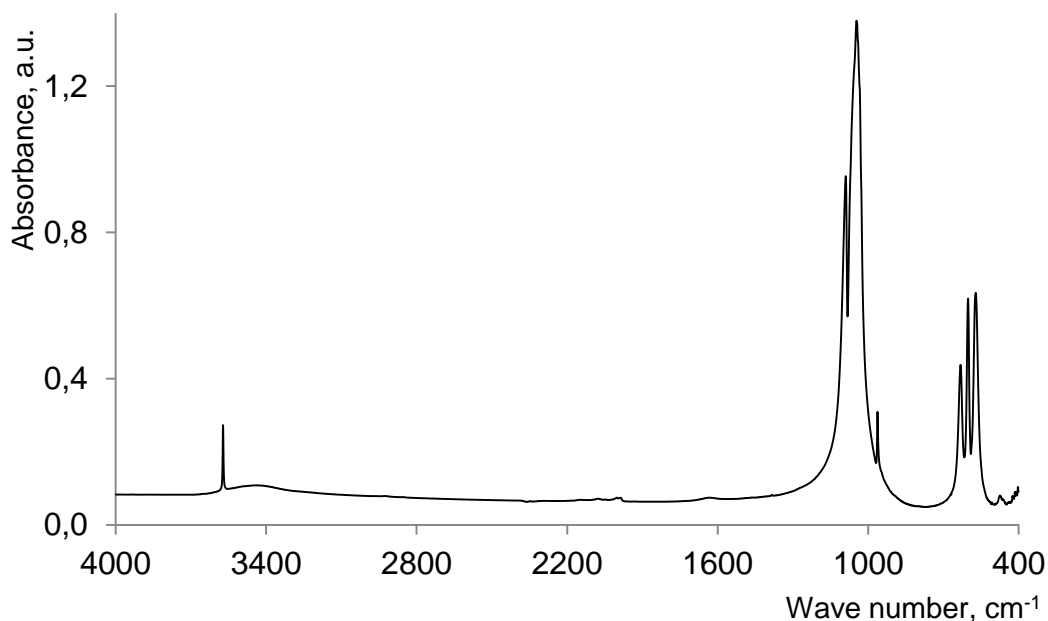
Fig. 3.2. FTIR spectra of the standard hydroxyapatite.

The measured calcium content was $39.39 \pm 0.19\%$, while phosphorous content was $18.39 \pm 0.12\%$, which gave the Ca/P molar ratio of 1.66. ICP-MS results (listed in the Table 3.1) showed a concentration of microelements in the standard hydroxyapatite. *Markovics et al.* analyzing a standard HA considered that only trace constituents with a mass fraction >0,0005% are significant [62]. Compared to their results, HA in this study contained microimpurities in much smaller amount, and only Sr with a mass fraction of 0,00266% exceeds that limit. According to the ISO13779-1:2008(E) standard [179] maximum allowed limit for impurities is 50 µg/g, except for arsenic it is 3 µg/g, cadmium and mercury 5 µg/g, and lead 30 µg/g. The obtained results show the prepared standard hydroxyapatite contains trace elements in much lower concentration.

Table 3.1.

ICP-MS results of the standard hydroxyapatite, expressed in µg/g

Cr^{52}	Mn^{55}	Co^{59}	Ni^{60}	Cu^{63}	Zn^{67}	As^{75}	Sr^{88}	Cd^{111}	Pb^{207}
0.07	0.13	0.22	3.80	0.15	0.42	0.077	26.6	0.06	0.49
±0.004	±0.01	±0.08	±0.01	±0.04	±0.12	±0.008	±0.9	±0.004	±0.06

Note. Measured concentration of Rb, Ba, Ce and Hg was lower than 0.01 µg/g.

The obtained results suggested that HA used in this study can be considered as stoichiometric with regard to Ca/P ratio and purity, because it meets all conditions from the ISO13779-3:2008(E) [55] and ISO13779-1:2008(E) [179] standards:

- according to XRD results HA did not contain α- and β-tricalcium phosphate
- according to XRD results HA did not contain CaO
- there was no oxyapatite absorbance line in FTIR spectra at 434 cm^{-1}
- $1.65 \leq Ca/P \leq 1.82$
- the concentration of all chemical impurities is smaller than the limit listed in the standard.

The obtained standard hydroxyapatite was used for further experiments to develop a method for measuring the quantity of hydroxyl groups in the apatite. Based on the results mentioned above, it is proved that this material is pure, stoichiometric hydroxyapatite.

3.1.2. Thermal gravimetric analysis

During thermal treatment hydroxyl groups tend to release from HA structure in the form of water. Based on this principle the amount of OH$^-$ ions can be determined by measuring the weight loss using TGA. However, there are some limitations to this method that have to be taken into the account to obtain a valid result – the weight loss can result not only from the release of structural water, it can be also due to the release of adsorbed water, carbonate or other volatile species if the sample contains them. Another effect what can be sometimes observed during the TGA when the reaction media is not completely dry, is a small weight gain in the beginning of the reaction. This potential rehydroxylation of the sample during the heating is described in other studies [180].

To develop the method for OH$^-$ measurement three different thermal gravimetric analysis approaches which all produce a departure of structural water from the apatite structure were used:

1) standard HA powder was heated until decomposition to TTCP and TCP
2) heating standard HA with calcium pyrophosphate
3) heating standard HA with calcium fluoride

Other reactions are also possible such as heating HA with a chlorinating gas in order to replace OH$^-$ with Cl$^-$ (but chlorinating reagents are corrosive), or heating HA under dry CO_2 to get type A carbonate apatite.

Results from thermal analysis showed a weight loss in all reactions, and contrasting kinetics marked by a different start temperature and rate of weight loss. First reaction with heating hydroxyapatite displayed the highest thermal stability and the slowest rate of mass loss that commenced at 600 °C and continued to decomposition at 1350 – 1450 °C (Fig. 3.3-a). A plateau was reached above 1400 °C, indicating high thermal stability. X-ray diffraction suggested full decomposition to tricalcium phosphate and tetracalcium phosphate (Fig. 3.3-b).

The thermal reaction between HA and calcium pyrophosphate commenced at 600 °C and was complete at 1050 °C, resulting in a narrow window within which hydroxide ions were removed in accordance with the chemical reaction involved (Fig. 3.4). A full OH^- release could be presumed from the remaining pure α-TCP as shown by micro-XRD and FTIR spectroscopy (Fig. 3.4). Absorption bands characteristic to pyrophosphate was also detected in FTIR spectra, this is due to the excess of pyrophosphate used in the reaction. The broad FTIR peak at 3100 – 3600 cm^{-1} was representative of adsorbed water, possibly introduced during sample preparation.

The reaction between HA and CaF_2 started at an even lower temperature of 460 °C and was complete at 900 °C. The reaction seems to occur in two stages (Fig. 3.5). It could be related to the special stability of HA containing 50% F^- due to hydrogen bonding. According to other research hydroxyfluorapatites are the most stable, and are even less soluble than FA [181]. A total hydroxide ion loss was confirmed by fluorapatite and calcium oxide formation as attested in the micro-XRD pattern (Fig. 3.5). FTIR spectra of the heated powder showed vibrations characteristic of FA (Fig 3.5) and no OH^- absorption peaks at 3572 cm^{-1} belonging to HA. An absorption band at 3640 cm^{-1} assigned to OH^- from $Ca(OH)_2$ which is formed during the reaction of CaO with air (during sample preparation for FTIR), similarly, very weak bands of calcium carbonate at 870 and 1435 cm^{-1} can be observed.

a)

b)
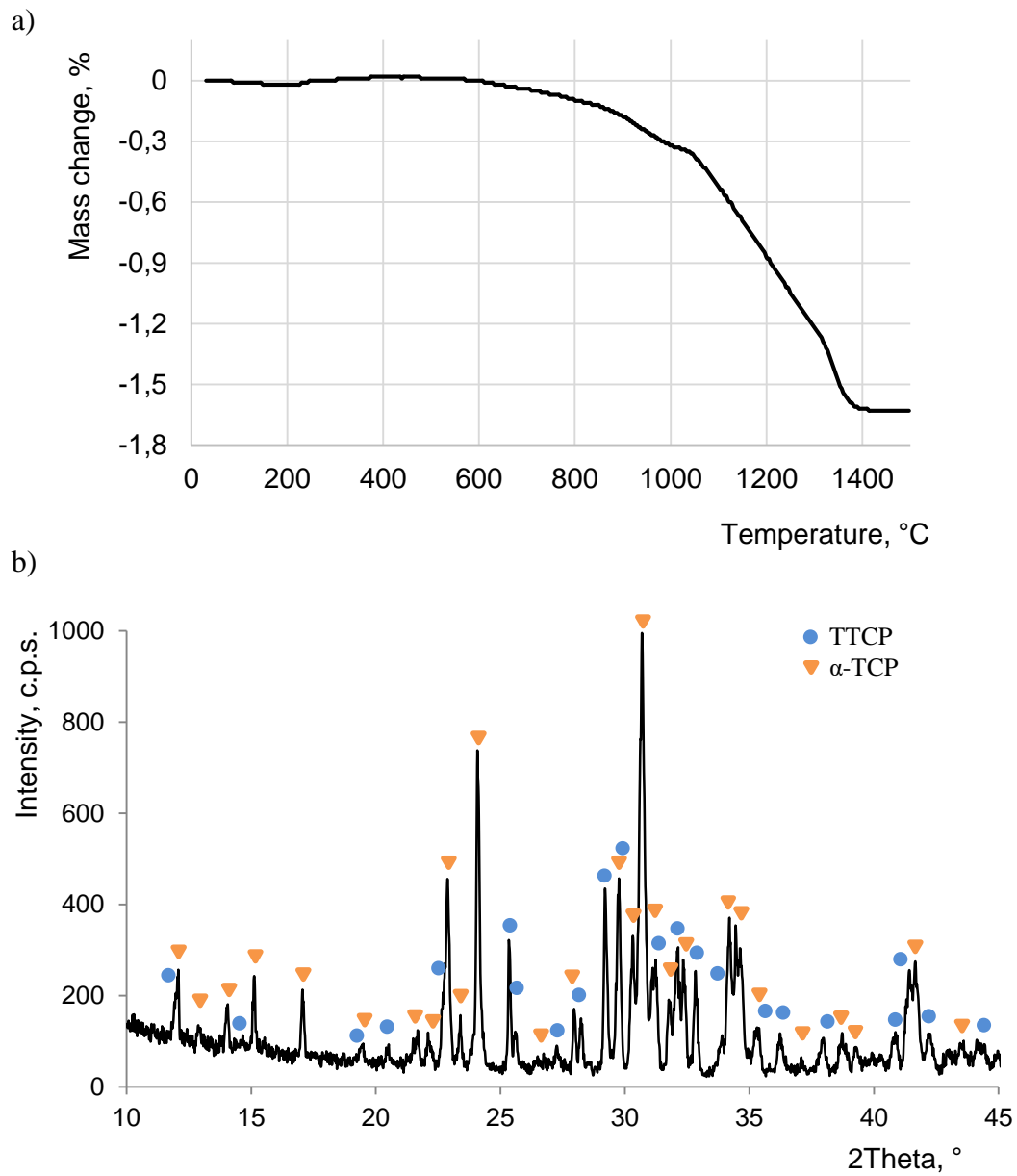
Fig. 3.3. Thermal gravimetric analysis (a), and XRD pattern after TGA (b) of the standard hydroxyapatite.

Thermal reaction

$$Ca_{10}(PO_4)_6(OH)_2 + Ca_2P_2O_7 \rightarrow 4Ca_3(PO_4)_2 + H_2O$$

Characterization of the final phase
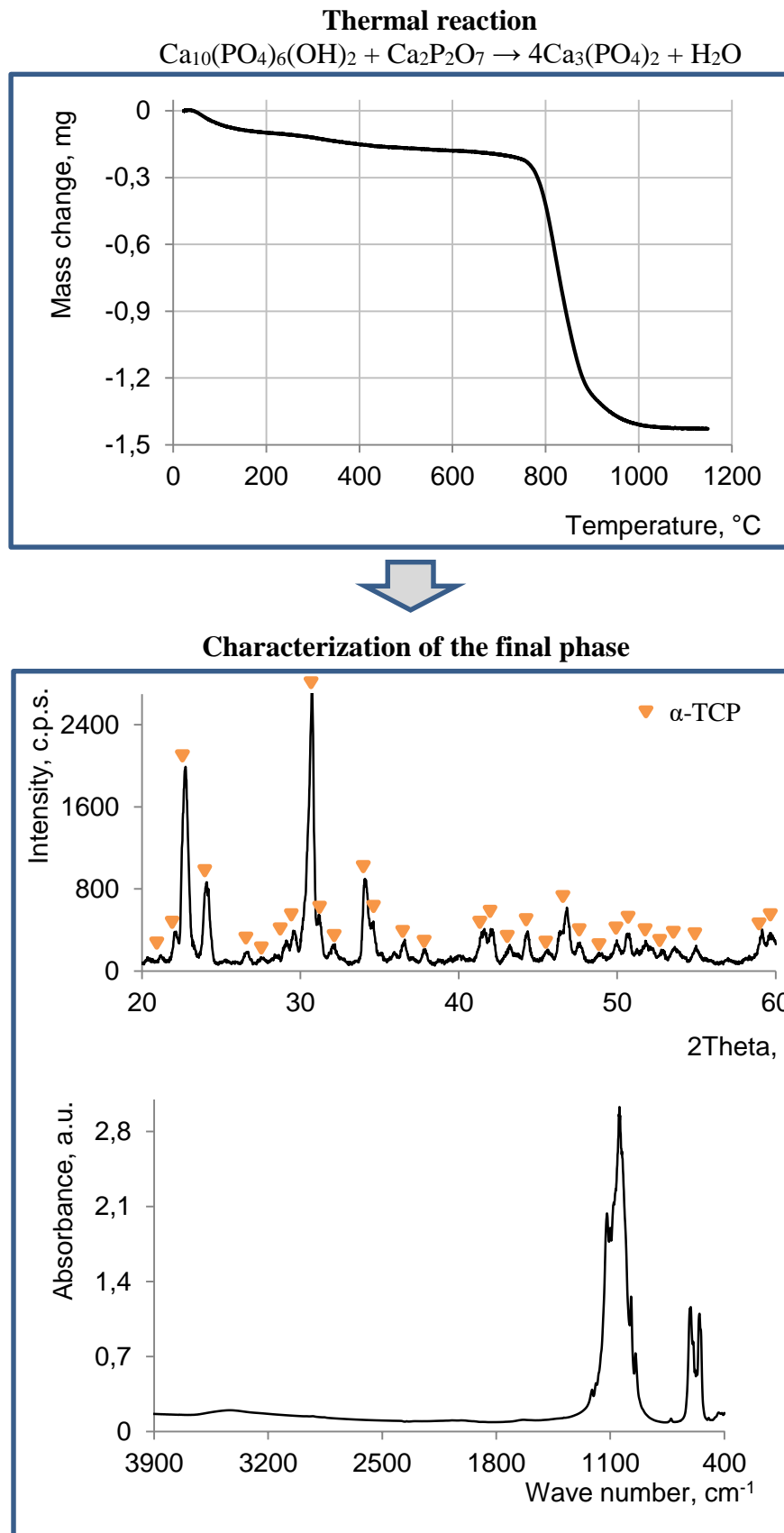
Fig. 3.4. TGA of HA and CPP mixture and characterization of the final phase after thermal reaction with XRD and FTIR.

Thermal reaction

$$Ca_{10}(PO_4)_6(OH)_2 + CaF_2 \rightarrow Ca_{10}(PO_4)_6F_2 + CaO + H_2O$$

Characterization of the final phase
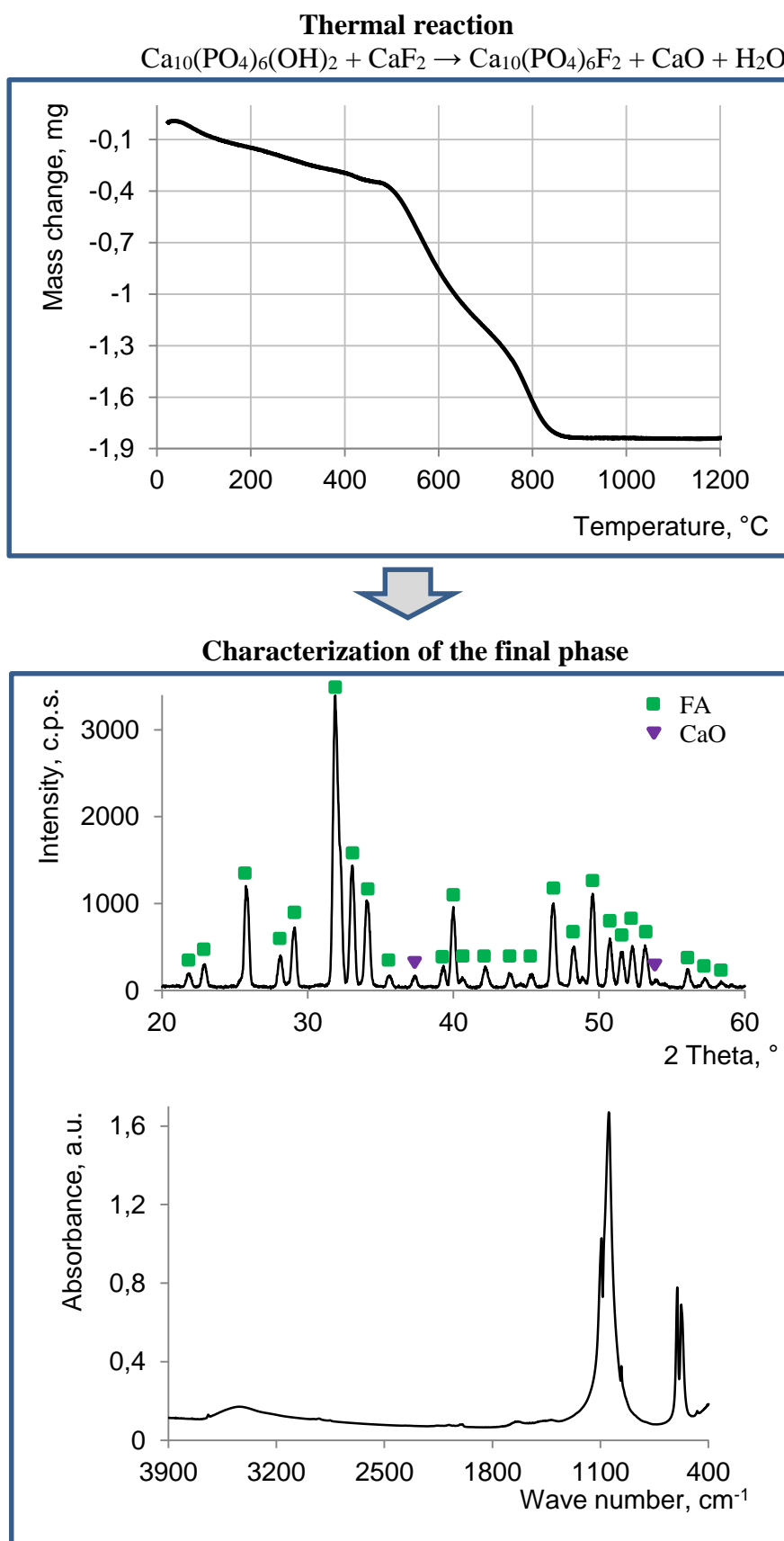
Fig. 3.5. TGA of HA and CaF_2 mixture and characterization of the final phase after thermal reaction with XRD and FTIR.

In order to use TGA results for calculation of the OH⁻ amount, several things must be taken into account:

- samples should be dried before the reaction to minimize the effect of adsorbed water on the mass change;
- since the completion of the solid state reactions depend on the contact between particles, every HA crystal has to be in close proximity with reactant crystals. An excess amount of the reactants must be used to be sure that no HA crystal has escaped the reaction and a complete reaction has been reached;
- larger amount of mixture than that strictly needed for the TGA experiment should be prepared to insure better homogenization during grinding;
- homogeneous mixture is the most important step to obtain complete reaction. Sufficient time and care must be given to the grinding process;
- mass loss at 100 – 150 °C corresponds to the adsorbed water (due to insufficiently dried samples or it might be also incorporated during the grinding process), it must be subtracted during the calculations;
- mass loss at 250 – 400 °C also corresponds to the water [43] and should be subtracted to get the dry mass of the sample.

The distinct mass loss in the TGA curve showed the possibility to quantify the structural water content within hydroxyapatite powder (formula used for the calculations is described in the methods section). Experimental results are summarized in the Table 3.2. Mass loss up to 400 ºC was excluded on determining the experimental values from TGA curve. As results strongly depend on the sample preparation, at least three repeated measurements for each reaction were performed and standard deviation was calculated. TGA from all repeated measurements and full calculations are included in Appendix 1.

Table 3.2

Percentage of occupied OH⁻ sites based on weight loss from thermal analysis

Thermal reaction	Temperature of reaction, °C	Mass change due to OH⁻ release, %	*Amount of OH⁻, %	Average amount of OH⁻ ± STDEV, %
HA	600 - 1450	1.53	85.45	84.47 ± 6.83
		1.63	90.75	
		1.38	77.20	

HA + CPP	600 - 1050	1.74	96.96	102.12 ± 5.11
		1.77	98.83	
		1.94	107.94	
		1.88	104.77	
HA + CaF$_2$	450 - 850	1.90	105.98	99.83 ± 5.66
		1.77	98.71	
		1.70	94.82	

* compared to OH⁻ amount of stoichiometric HA: 1.79 %

For the calculation of OH⁻ amount, the first reaction (decomposition of HA in high temperature) does not give demonstrative and clear results, because of the high thermal stability of HA. It is difficult to determine a clear start and end point of the reaction. The high temperature needed for the reaction could also result in the depletion of phosphate [182]. An overlap may occur between the temperature range for dehydroxylation and loss of phosphate, that complicates the calculation of OH⁻ content. A further degree of complication could arise when a non-stoichiometric apatite produced decomposition phases at lower temperatures.

The more suitable techniques include both the use of calcium fluoride and calcium pyrophosphate, because the release of OH⁻ happens faster and in lower temperature: 460 – 900 °C for HA reaction with CaF$_2$ and 600 – 1050 °C for HA reaction with CPP. However, the low temperature for the beginning of the HA reaction with CaF$_2$ makes it difficult to see the start of OH⁻ release if adsorbed water is stabilized by capillary effects and requires higher temperature for release. In thermal reaction with calcium fluoride an additional loss due to the hydrolysis from the release of HF and the formation of CaO could also happen. Considering the above mentioned complications, HA thermal reaction with calcium pyrophosphate might be the most reliable for determining the amount of hydroxyl ions.

Solid state reactions strongly depend on the particle size, and so a complete reaction may never actually happen if the HA particles are too large. Also, using grinding there is always a risk that the mixture is not homogeneous (there are always particles still remaining in the mortar after grinding and it is assumed that they are an exact mixture of those in the powder). As a result, the thermal reaction methods, although simple and straightforward from a theoretical perspective, practically are not that simple to use in order to get a precise result.

Based on the results described above it was proved that the prepared standard hydroxyapatite is fully hydroxylated – OH^- amount within the margins of error corresponds to the theoretical OH^- concentration in the stoichiometric hydroxyapatite.

3.1.3. Fourier transform infrared spectroscopy

Fourier transform infrared spectroscopy offers a narrow and well-defined hydroxyl ion adsorption peak for measuring the OH^- content. Different samples can be compared by measuring the intensity or area of the absorption peaks. Since the hydroxyl group has its characteristic absorption peak - there is no interference from other groups - this clear distinction makes FTIR better than the TGA method. The vibration of OH^- in hydroxyapatite is at 3571 cm^{-1} (stretching mode) and 635 cm^{-1} (librational mode).

For obtaining quantitative results a calibration curve using the samples with known amount of hydroxyl groups should be prepared. For this reason, the hydroxyapatite sample with maximum amount of OH^- ions in the structure and one with no OH^- ions is needed. In this work 2 approaches were used to obtain samples with different concentration of OH^-, which could be used to prepare the calibration curve:

1. Mechanical mixtures in different ratios of standard hydroxyapatite and fluorapatite (FA does not contain any OH^- ions, but its structure is similar to the structure of HA).
2. Various oxyhydroxyapatite (OHA) solid solutions.

3.1.3.1. Hydroxyapatite/ Fluorapatite mechanical mixtures

First calibration curve was obtained using mechanical mixtures in various ratios of fully hydroxylated HA (standard HA) and fluorapatite. Standard HA is described in the section 3.1.1. XRD analysis of FA showed diffraction peaks characteristic to fluorapatite phase (according to ICDD number 00-015-0876). FTIR spectra of FA showed that it contains a minor quantity of OH^- from an $OH^- \cdots F^-$ absorption band at 3534 cm^{-1} and 746 cm^{-1} (Fig. 3.6). Based on other studies, the presence of these absorption bands suggest that the F^- content in fluorohydroxyapatite is at least 75% [183-185]. Absorption bands at 1950 – 2200 cm^{-1} are characteristic to the overtones and combinations of the ν_3 and ν_1 PO_4 modes [62].

a)

b)
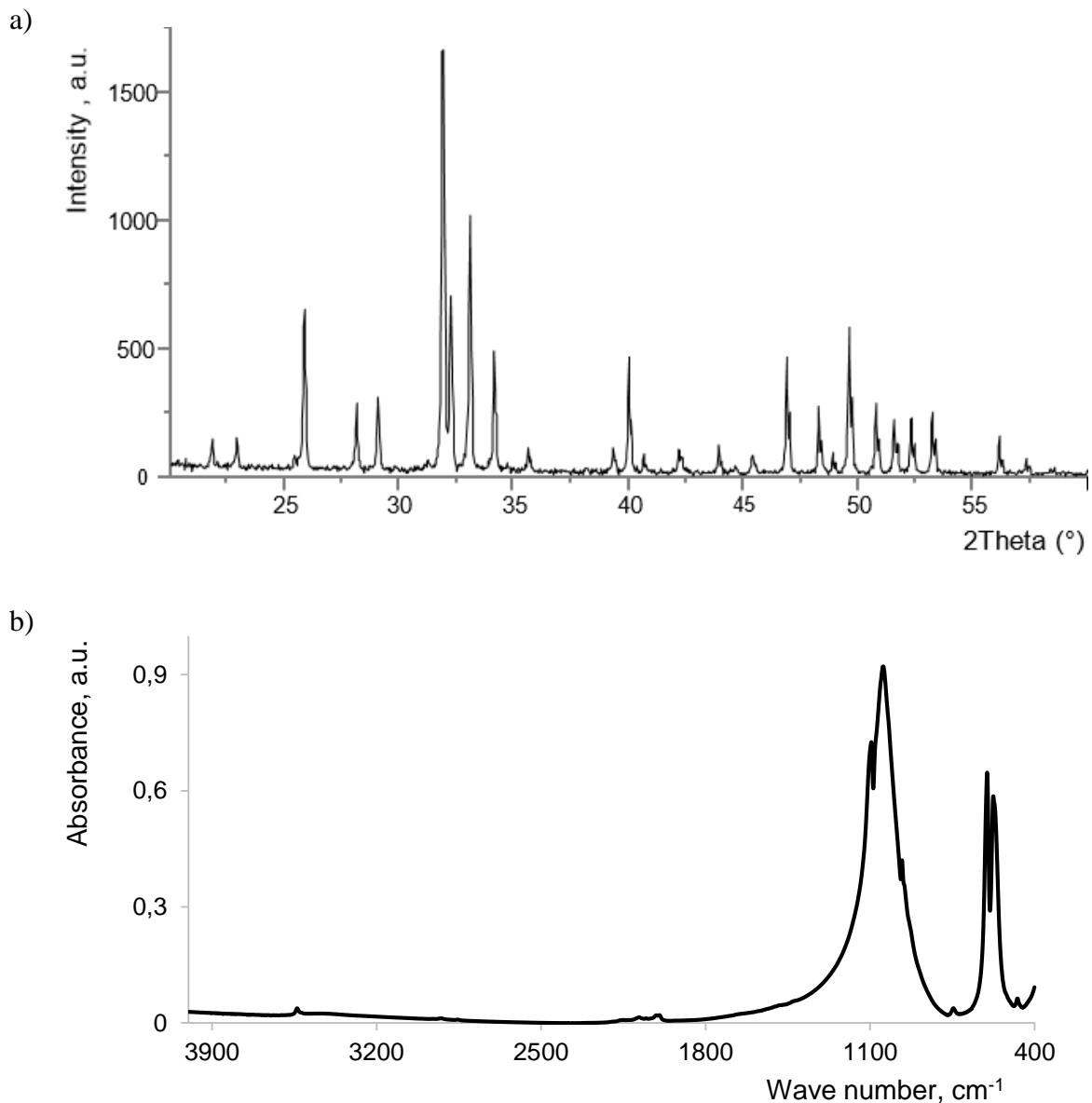
Fig. 3.6. XRD pattern (a) and FTIR spectra (b) of fluorapatite used for HA/FA mechanical mixtures.

To minimize the effects of sample preparation on the calibration curve, all HA/FA powder blends were prepared at the same time, under the same conditions. A calibration curve was made from HA concentrations in steps of 25 wight% with FA. For each mechanical mixture 3 pellets with KBr were prepared and FTIR spectra was recorded (Fig. 3.7). OH^- absorption band at 632 cm^{-1} was chosen for the calculations of OH^- amount in hydroxyapatite because this band is more sensitive than absorption band at 3571 cm^{-1} [86]. To separate the OH^- peak from phosphate peaks, spectral area of 500 – 700 cm^{-1} was deconvulated, and area of OH^- and PO_4^{3-} peaks was measured (Fig. 3.8).
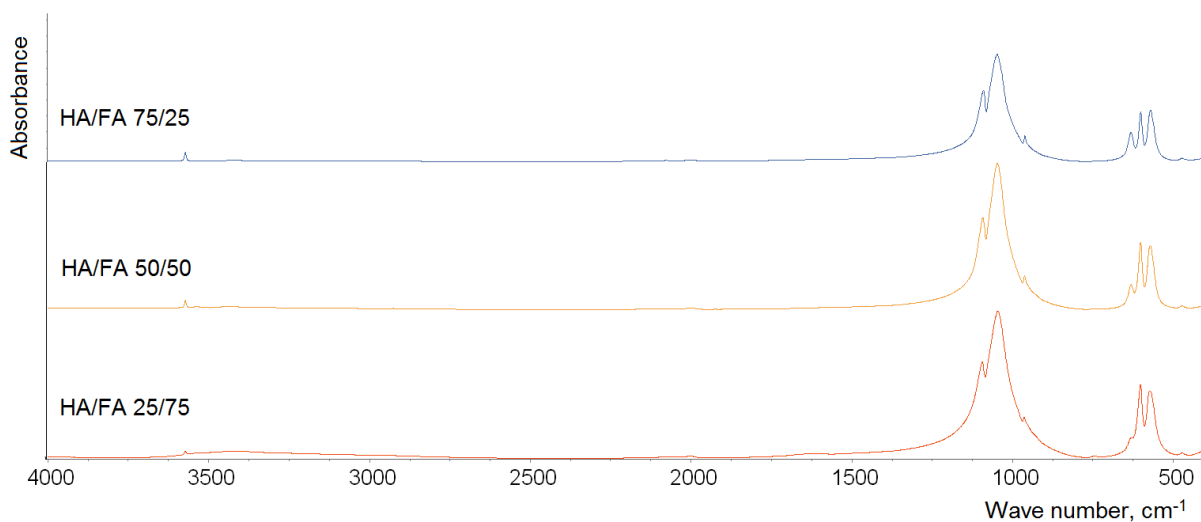
Fig. 3.7. FTIR spectra of HA/FA mixtures.

Best mathematical fit after baseline correction and using lorentzian type of curves is shown in Fig. 3.8. A model with 7 lorentzian curves was used for all HA/FA samples. For mathematical fit the three ν_4 phosphate peaks characteristic to apatite phase (567, 574 and 601 cm^{-1}) are shown as 4 curves in 600 to 565 cm^{-1} range. Small peaks at 653 and 668 cm^{-1} are necessary to add to the mathematical deconvulation model. Absorption band at 668 cm^{-1} has been previously reported in fluorapatite samples [186]. It is assumed that the absorption band at 653 cm^{-1} could be associated with KBr sample preparation technique and might be introduced from adsorbed water. Area of both peaks at 653 and 668 cm^{-1} is not used for OH$^-$ calculations.

The ratio of the OH$^-$ absorption peak area at 632 cm^{-1} relative to the ν_4 PO$_4^{3-}$ absorption peaks area at 565 - 600 cm^{-1} was calculated (Table 3.3) and plotted against the OH$^-$ content according to the increasing amounts of HA in HA/FA powder mixtures. This internal reference removed the influence of powder mass by providing an internal standard.
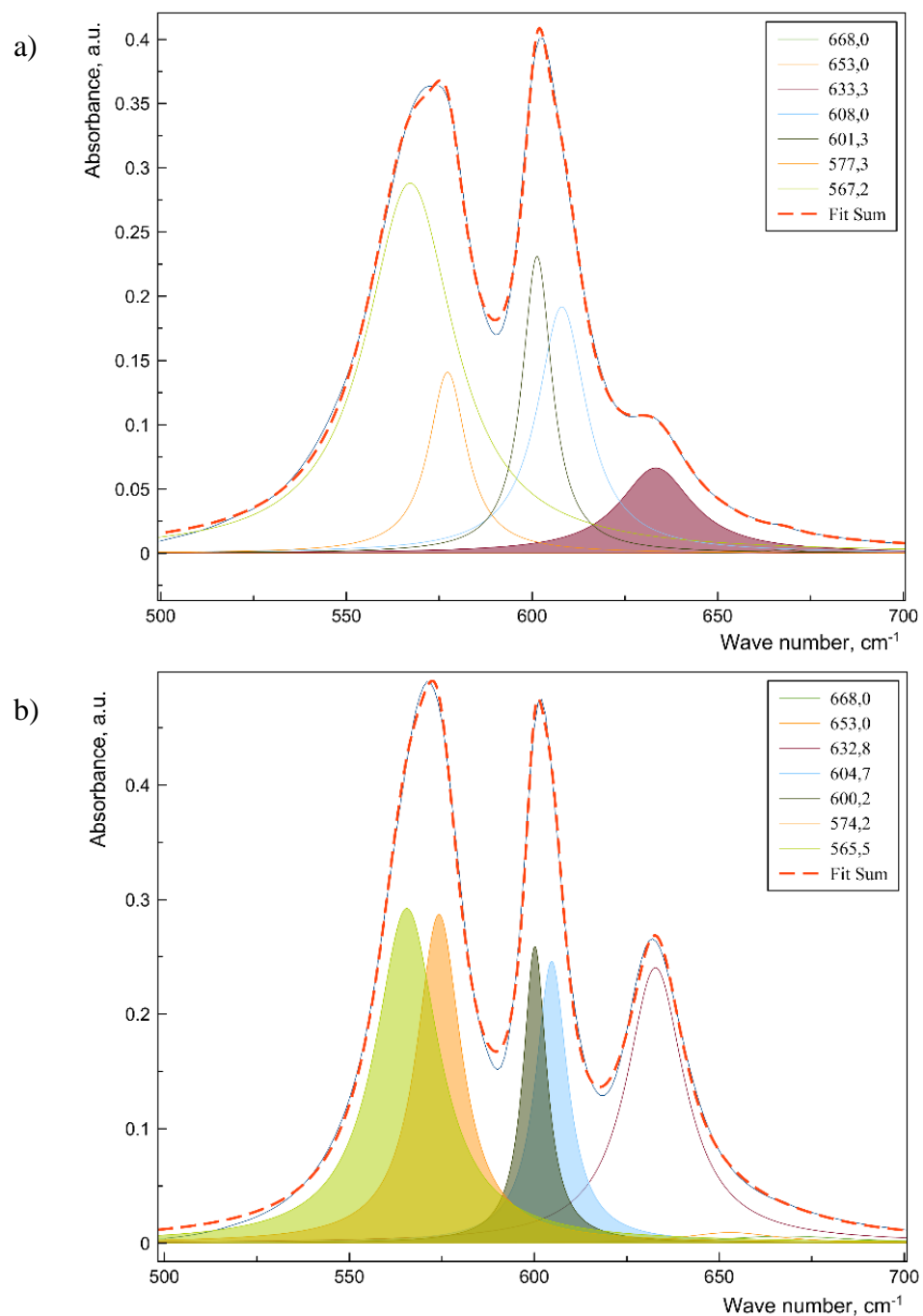
Fig. 3.8. Deconvulated FTIR spectra of: (a) HA/FA mechanical mixture with 25% HA, and (b) HA/FA mechanical mixture with 75% HA. For better visualization, OH⁻ peak area used for further calculations is colored in figure a, and total PO_4^{3-} peak area used for further calculations is colored in figure b.

Table 3.3.

Hydroxyl ion (at 632 cm^{-1}) and phosphate ion (at 565 – 600 cm^{-1}) peak areas* of HA, FA and HA/FA mechanical mixtures measured from FTIR spectra

| Sample type	OH$^-$ peak area, a.u.	Sum of PO$_4^{3-}$ peak areas, a.u.	OH/ PO$_4$	Average (OH/ PO$_4$) ± stdev (RSD, %)	**Corrected average (OH/ PO$_4$)
100% HA	4.48	12.05	0.37	0.36 ± 0.013 (3.52)	0.36 ± 0.013 (3.52)
	12.17	33.70	0.36		
	8.64	24.92	0.35		
75% HA/ 25% FA	6.15	21.69	0.28	0.31 ± 0.023 (7.46)	0.30 ± 0.023 (7.46)
	6.21	20.04	0.31		
	7.40	22.48	0.33		
50% HA/ 50% FA	4.08	22.89	0.18	0.18 ± 0.007 (3.78)	0.17 ± 0.007 (3.78)
	4.66	24.79	0.19		
	2.89	16.53	0.17		
25% HA/ 75% FA	4.72	40.19	0.12	0.10 ± 0.014 (14.22)	0.09 ± 0.014 (14.22)
	3.53	39.44	0.090		
	4.84	49.72	0.097		
100% FA	1.04	71.49	0.014	0.01 ± 0.002 (16.18)	0
	0.40	37.90	0.011		
	0.43	36.37	0.012		

Full data about peak parameters and replicate samples are included in Appendix 2.

*** For the calibration curve corrected OH/PO$_4$ values were used. Correction was made by subtracting the OH/PO$_4$ value of 100% FA sample of all other samples containing FA fraction.*

As mentioned before, fluorapatite sample used for the mixtures contains a small amount of OH$^-$ ions. For the calibration curve calculations results were corrected by the OH/PO$_4$ ratio in the FA sample. Value of 0.01 was subtracted from all samples containing fluorapatite. From the obtained results, a calibration curve was constructed with the amount of HA phase in the sample on abscissa and ratio of OH$^-$/PO$_4^{3-}$ area on the ordinate (Fig. 3.9). The coefficient of determination (R^2) which shows how well a line fits a set of data was obtained 0.9921. OH$^-$ concentration for unknown sample can be calculated using the equation:

$$x = \frac{y + 0{,}0027}{0{,}0037}$$

where x is OH$^-$ concentration and y is the OH$^-$/PO$_4{}^{3-}$ ratio.
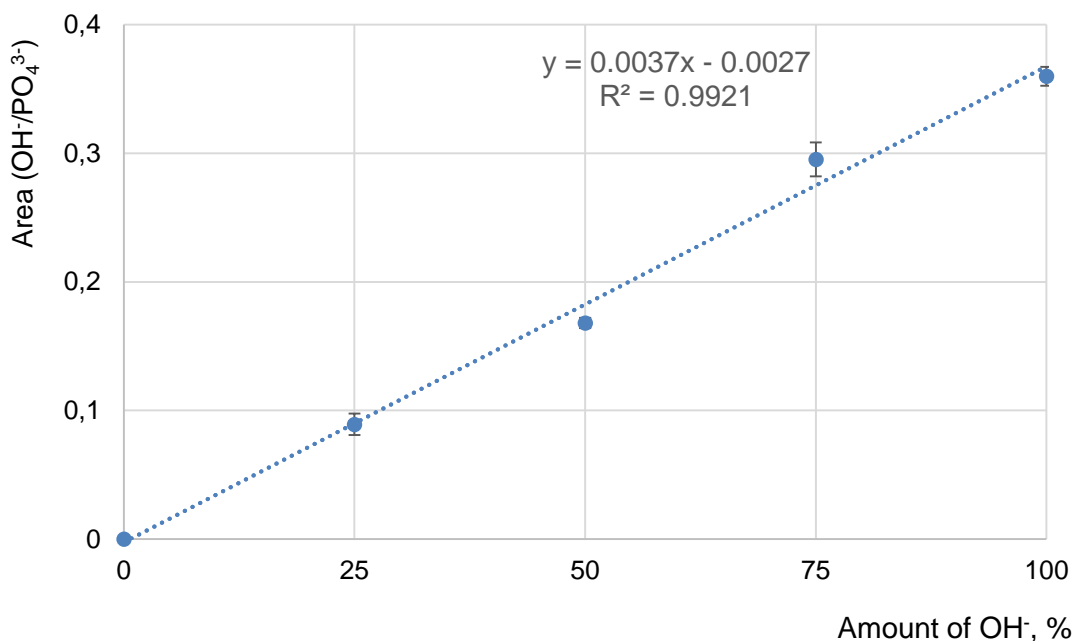
Fig. 3.9. Calibration curve for determining the amount of OH$^-$ in hydroxyapatite using OH$^-$ at 632 cm^{-1} and PO$_4{}^{3-}$ at 565 – 600 cm^{-1} peak areas from FTIR spectra.

The linearity of the method is proved by the calibration curve (Fig 3.9) and its equation. To evaluate precision and accuracy of the developed method additional samples were prepared and measured. Additional mechanical mixtures of HA and FA were prepared in different ratios than those used to make a calibration curve. Mechanical mixtures with HA/FA ratio 40/60, 60/40 and 80/20 were prepared and three sample replicates were measured. Six new KBr/sample pellets from a previously used HA/FA powder with a ratio 50/50 were also prepared. For all these samples spectra were recorded, deconvulated and OH$^-$/PO$_4{}^{3-}$ ratio was calculated (information about the peak areas is includen in Appendix 3). Hydroxyl ion content in percentage was calculated using the equation from calibration curve.

Calculated absolute deviation value shows how much values vary from each other, hence the precision of the method. It was calculated by following formula:

$$Deviation = Average\ of\ (average\ of\ data - each\ individual\ value)$$

The accuracy (the closeness of the measurement to its actual value) of the measurements were calculated using following formula:

$$Accuracy\ (\%) = \frac{theoretical\ value - experimental\ value}{theoretical\ value} \times 100$$

where theoretical value is the weighted percentage of HA in HA/FA mechanical mixtures. Results (included in Table 3.4) showed that the average precision of the method is ± 2% (up to 3% for individual values), while the average accuracy is 6% (up to 14% for individual values). The differences between individual values indicated that more than one replicate sample should always be measured and the value averaged.

Table 3.4.

Evaluation of the precision and accuracy of the developed hydroxyl ions quantification method

Weighted amount of HA, %	OH^-/PO_4^{3-}, a.u.	OH^-, %	Calculated average OH^-, %	Absolute deviation, a.u.	Average deviation, a.u.	Absolute accuracy, %	Average accuracy, %
80	0.30	80.67	81.07	0.40	0.27	0.84	1.34
	0.30	81.48		0.41		1.85	
	0.29	81.06		0.01		1.32	
60	0.24	64.42	63.85	0.57	0.51	7.37	6.42
	0.23	63.08		0.77		5.14	
	0.23	64.05		0.20		6.75	
50	0.17	47.92	50.46	2.54	0.92	4.15	2.31
	0.19	51.33		0.86		2.65	
	0.19	50.85		0.39		1.70	
	0.18	50.23		0.23		0.45	
	0.19	51.50		1.04		3.00	
	0.19	50.94		0.48		1.88	
40	0.17	45.44	42.56	2.88	1.92	13.61	6.40
	0.15	41.74		0.82		4.35	
	0.15	40.49		2.07		1.24	

3.1.3.2. Oxyhydroxyapatites

Preparation of HA ceramics requires heating and hence dihydroxylation occurs, forming a solid solution of HA and oxyapatite. For that reason, the best way for obtaining the calibration curve would be using HA which is fulfilled with OH^-, OAp which does not contain any OH^- and HA/OAp solid solutions or oxyhydroxyapatite (OHA) with known amount of OH^- ions in its structure. However, pure OAp has not been prepared, the best result mentioned in the literature is 75% OAp [91].

Oxyhydroxyapatite with the least amount of OH^- in the structure was prepared using high temperature (1000 °C) heating for 20 or 43 hours in vacuum in closed quartz system. Standard HA (described in the section 3.1.1) was used as a starting powder. For 20 h heated HA sample was labeled as HA_v6 and for 43 h heated HA sample was labeled as HA_v8. XRD results (Fig. 3.10-a) confirmed that the prepared OHA samples do not contain any decomposition phase (TCP, TTCP, CaO), in fact all diffraction peaks were characterized as hydroxyapatite. FTIR results also showed absorption bands characteristic only to apatite (Fig. 3.10-b). Traces of OH^- absorption bands at 3570 and 632 cm^{-1} and PO_4^{3-} band at 961 cm^{-1} showed the presence of hydroxyapatite phase, while PO_4^{3-} absorption bands at 433, 475 and 945 cm^{-1} are characteristic of OAp [5, 92].

To prepare more samples for the calibration curve (with different OH^- concentration) rehydroxylation of HA_v8 sample was carried out. Hydroxyl groups were re-introduced in the structure of sample by heating it in air with 90% of humidity at different temperatures (350, 400 and 700 °C). Holding time at all temperatures was 0,5 h, except for one sample which was held for 1 h at 400 °C. XRD for all samples was recorded and all samples showed only HA phase, no traces of decomposition. FTIR spectra also confirmed HA phase and indicated the presence of OAp (XRD patterns and FTIR spectra of all rehydroxylated OHA samples are included in Appendix 4).
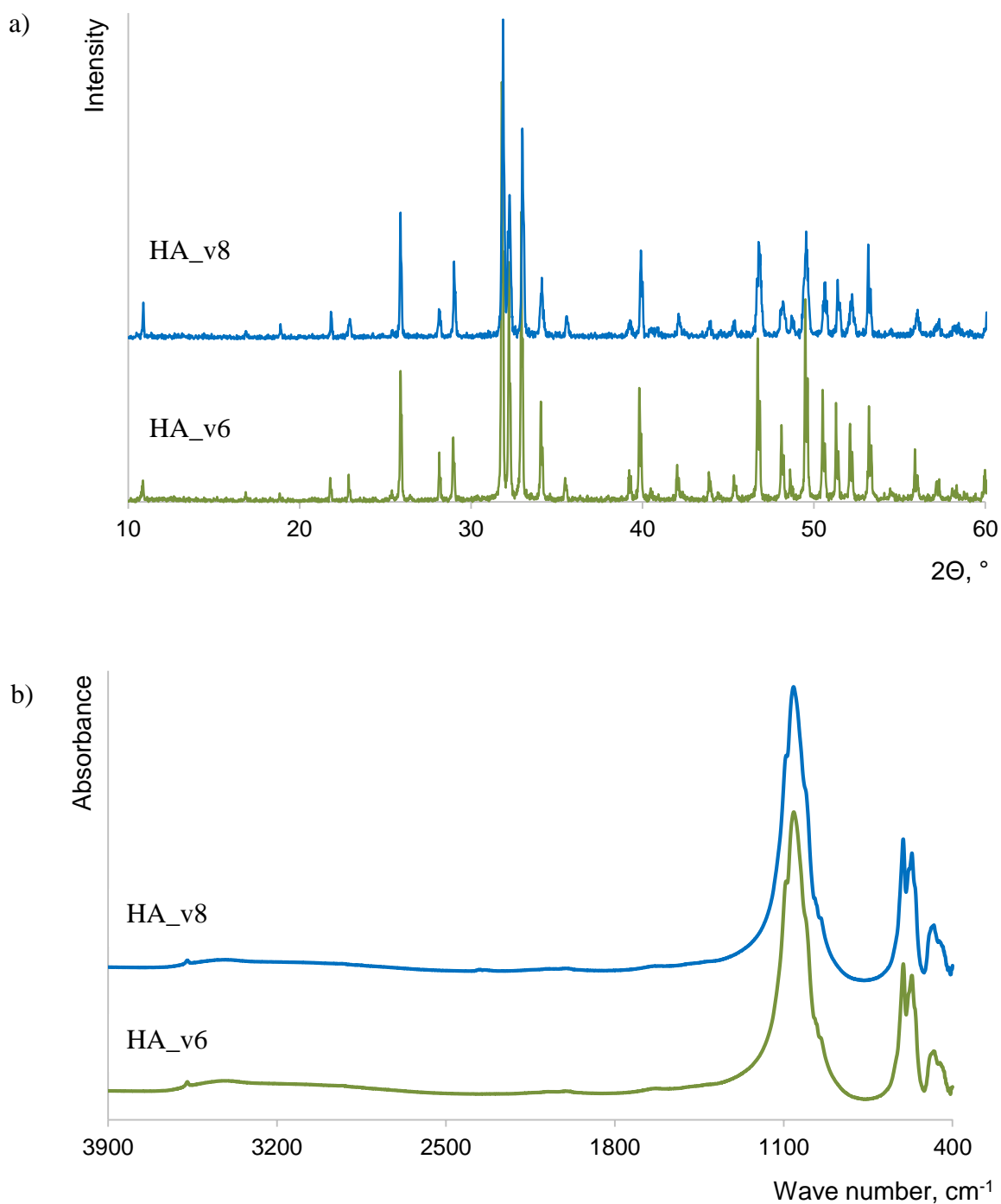
Fig. 3.10. XRD patterns (a) and FTIR spectra (b) of vacuum heated standard hydroxyapatite.

All prepared OHA samples were used to calculate OH⁻ amount. FTIR spectra for at least 3 KBr pellets of the same sample was recorded. Two approaches were used to calculate OH⁻ amount from FTIR spectra:

1. Area of OH⁻ adsorption peak at 632 cm^{-1} relative to the area of ν_4 PO$_4^{3-}$ absorption peaks was calculated. In order to separate adsorption peaks, deconvolution of the spectral range between 500 and 750 cm^{-1} was performed (Fig. 3.11).

2. Area of OH⁻ adsorption peak at 3570 cm^{-1} (spectral range between 3596 and 3541 cm^{-1}) relative to the area of PO$_4^{3-}$ absorption peaks in spectral range between 800 and 1300 cm^{-1} was calculated (Fig. 3.12). The same spectral range was used to calculate all samples.
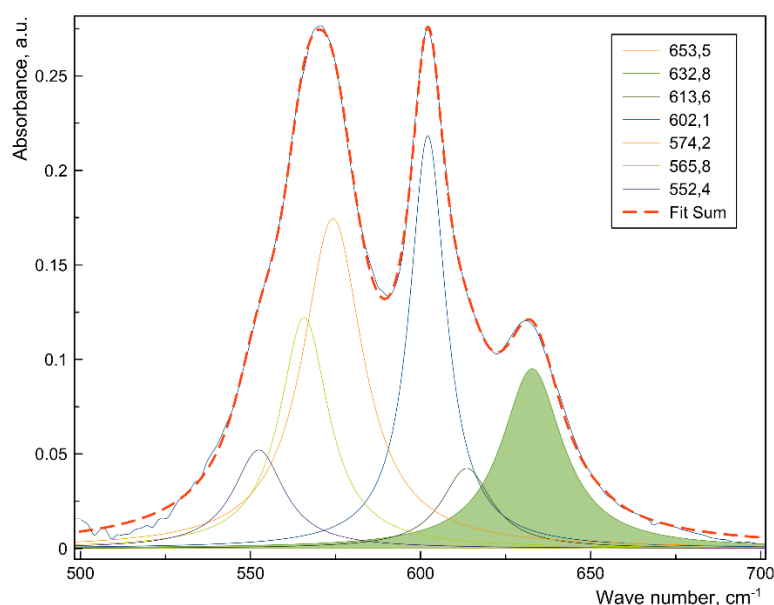
Fig. 3.11. Deconvulated FTIR spectra of HA_v8_reh400-1h sample. For better visualization, OH⁻ peak area used for further calculations is colored.

As a result of deconvolution for the best mathematical fit in total 5 phosphate peaks were separated for OHA samples (Fig. 3. 11). Analyzing deconvoluted peaks some observations can be made (tables with precise locations of each absorption band of deconvuluted FTIR spectra for OHA samples are included in Appendix 5):

- OH⁻ peak location shifts to higher wave number with larger OAp content: 632 cm^{-1} for HA with 100% OH⁻ and ~ 637 cm^{-1} for HA sample with the least amount of OH⁻.
- There is an additional PO$_4^{3-}$ peak at 611 – 614 cm^{-1} for OHA samples (this absorption line was not observed for pure HA samples)
- There is a shift for another PO$_4^{3-}$ peak: ~ 575 cm^{-1} for 100% HA shifts to about 582 cm^{-1} for sample with the largest amount of OAp phase.

Absorption line broadening and shifting due to slight structural and/ or crystallographical changes in substituted apatites has been reported before [187, 188], but above mentioned shifts in oxyhydroxyapatite samples has not been mentioned before. The ratio of the OH^- absorption peak area at 632 cm^{-1} relative to the ν_4 PO_4 absorption peaks area at 565 - 600 cm^{-1} was calculated (Table 3.5).

<div align="right">Table 3.5.</div>

Hydroxyl ion (at 632 cm^{-1}) and phosphate ion (at 565 – 600 cm^{-1}) peak areas* of OHA measured from FTIR spectra

Sample type	OH⁻ peak area, a.u.	Sum of PO_4^{3-} peak areas, a.u.	OH/ PO_4	Average (OH/ PO_4) ± stdev (RSD, %)
Standard HA	9.97	27.30	0.37	0.38 ± 0.012 (3.16)
	9.52	24.15	0.39	
	4.38	11.69	0.38	
	6.66	17.60	0.38	
HA_v8_reh700	12.91	35.01	0.37	0.37 ± 0.003 (0.91)
	10.74	28.64	0.37	
	8.56	22.85	0.37	
HA_v8_reh400-1h	6.10	25.53	0.24	0.26 ± 0.010 (3.88)
	8.71	33.76	0.26	
	8.32	30.92	0.27	
	6.79	27.08	0.25	
	4.00	15.64	0.26	
	4.33	16.74	0.26	
HA_v8_reh400	4.15	19.52	0.21	0.22 ± 0.008 (3.78)
	4.65	20.98	0.22	
	5.26	22.93	0.23	
HA_v8_reh350	3.42	25.56	0.13	0.14 ± 0.009 (6.04)
	3.03	21.76	0.14	
	4.68	31.11	0.15	
HA_v6	1.53	32.85	0.05	0.05 ± 0.004 (8.24)
	2.32	46.40	0.05	

	1.34	31.67	0.04	
HA_v8	1.05	33.73	0.03	0.03 ± 0.001
	1.11	34.31	0.03	(3.21)
	0.80	26.33	0.03	

* Full data about peak parameters and replicate samples are included in Appendix 5.

a)

b)
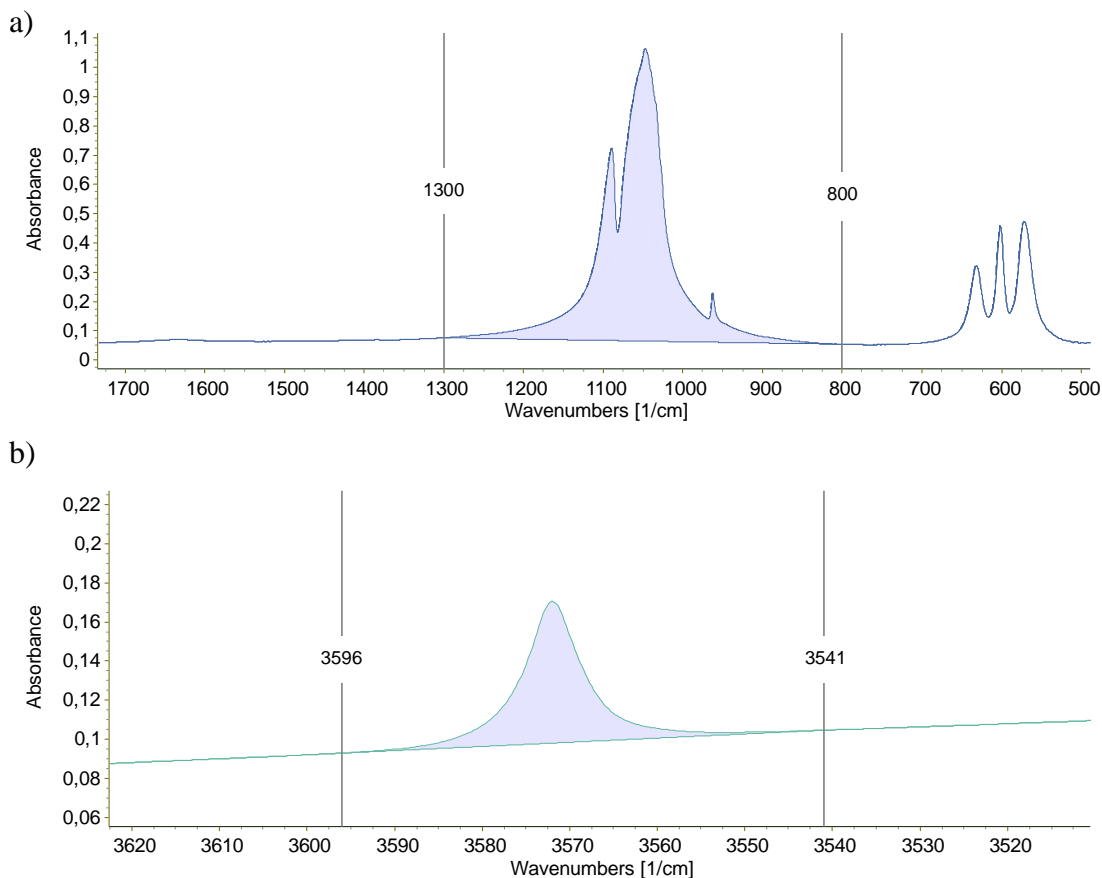
Fig. 3.12. Highlighted (a) PO_4^{3-} and (b) OH^- absorption band areas for the calculation of OH^- amount from FTIR spectra (sample: HA_v8_reh400-1h).

In the second case, both ν_1 and ν_3 PO_4^{3-} absorption lines are used for the calculation without a separation. Many PO_4^{3-} absorption lines overlap in this area, so it is difficult to fully deconvulate it. For a random sample which might contain not only HA and OAp, but also some non-apatitic phosphate groups deconvulation of this area would be even more complicated. As relatively wide range of the spectra was chosen (800 – 1300 cm^{-1}) it is safe to assume that all interference from the phosphate bands is accounted for (Fig. 3.12).

The ratio of the OH^- absorption peak area at 3596 - 3541 cm^{-1} relative to the PO_4 absorption peaks area at 1300 - 800 cm^{-1} was calculated (Table 3.6).

91

Table 3.6.

Hydroxyl ion (at 3596 - 3541 cm^{-1}) and phosphate ion (at 1300 - 800 cm^{-1}) absorption band areas of OHA measured from FTIR spectra

Sample name	OH$^-$ peak area, a.u.	PO$_4^{3-}$ peak areas, a.u.	OH/ PO$_4$	Average (OH/ PO$_4$) ± stdev (RSD, %)
Standard HA	1.03	118.6	0.0087	0.0082 ± 0.0003 (4.00)
	0.91	113	0.0081	
	0.43	53.59	0.0080	
	0.66	83.62	0.0080	
HA_v8_reh700	1.28	150.1	0.0085	0.0085 ± 0.0001 (1.15)
	1.09	128.2	0.0085	
	0.88	101.4	0.0087	
HA_v8_reh400-1h	0.62	110.9	0.0056	0.0057 ± 0.0005 (7.91)
	0.85	147.2	0.0058	
	0.85	129.1	0.0066	
	0.68	125.8	0.0054	
	0.39	71.16	0.0054	
	0.41	76.25	0.0053	
HA_v8_reh400	0.38	86.29	0.0045	0.0048 ± 0.0004 (7.78)
	0.45	93.72	0.0048	
	0.49	94.48	0.0052	
HA_v8_reh350	0.36	107.1	0.0034	0.0036 ± 0.0002 (5.24)
	0.34	90.35	0.0038	
	0.47	132.6	0.0036	
HA_v6	0.23	124.1	0.0018	0.0018 ± 0.0001 (2.36)
	0.33	188.5	0.0018	
	0.22	123.7	0.0017	
HA_v8	0.18	126.2	0.0014	0.0015 ± 0.0001 (6.34)
	0.20	131.2	0.0015	
	0.16	96.52	0.0016	

In the Table 3.7 the calculated OH^- amounts are included. As before, it is assumed that the standard HA contains 100% of OH^- ions, and knowing the OH/PO_4 ratio for the standard sample, OH^- amount for all other samples are calculated. The obtained result (using OH^- absorption line at 632 cm^{-1}) is compared with the OH^- concentration obtained from the calibration curve (described in the section 3.1.3.1). Results show that calculation using the calibration curve gives 1 – 3% larger OH^- concentration, but it must be noted that the standard deviation for the measurements is up to 3%.

The calculations of the hydroxyl amount using the OH^- absorption line at 3570 cm^{-1} coincide with the results using OH^- absorption line at 632 cm^{-1} only for half of the samples where OH^- amount is more than 50%. For samples with less OH^- concentration this method shows 15 – 55 % more OH^- in the structure (15% for HA_v8_reh350; 45% for HA_v6 and 55% for HA_v8). This proves the statement that OH^- absorption line at 3570 cm^{-1} in FTIR spectra is less sensitive to structural changes in sample, as was suggested by *Rapacz-Kmita et al.* [86]. Measurements using OH^- absorption line at 3570 cm^{-1} also have larger standard deviation (up to 6%). The reason for this is that absorption lines for these calculations were not deconvulated. Precise deconvulation of the absorption line at 3570 cm^{-1} is complicated because of the wide absorption lines of the adsorbed water in this area of spectra. Because of the hygroscopic nature of KBr it is very difficult to completely avoid water absorption during sample preparation. To fully eliminate interference from the moisture in the atmosphere samples should be prepared in a dry box and FTIR measurements should be recorded in vacuum.

Table 3.7.

The amount of hydroxyl ions in OHA samples calculated from FTIR spectra

Sample name	OH⁻ (632 cm⁻¹) / v4 PO₄³⁻			OH⁻ (3596 - 3541 cm⁻¹) / PO₄³⁻ (1300 – 800 cm⁻¹)	
	Average (OH/ PO₄)	OH⁻ amount, ± stdev % (RSD, %) *Assuming standard HA is 100%*	OH⁻ amount ± stdev, % (RSD, %) *From HA/FA calibration curve*	Average (OH/ PO₄)	OH⁻ amount, ± stdev % (RSD, %) *Assuming standard HA is 100%*
Standard HA	0.38	100	102.93 ± 3.22 (3.13)	0.0082	100
HA_v8_reh700	0.37	98.57 ± 0.89 (0.91)	101.47 ± 0.91 (0.90)	0.0085	104.54 ± 1.20 (1.15)
HA_v8_reh400-1h	0.26	67.47 ± 2.62 (3.88)	69.69 ± 2.67 (3.84)	0.0057	69.71 ± 5.64 (8.18)
HA_v8_reh400	0.22	58.50 ± 2.21 (3.78)	60.52 ± 2.26 (3.74)	0.0048	59.07 ± 4.59 (7.78)
HA_v8_reh350	0.14	37.34 ± 2.26 (6.04)	38.89 ± 2.31 (5.93)	0.0036	43.69 ± 2.29 (5.24)
HA_v6	0.05	12.22 ± 1.01 (8.24)	13.22 ± 1.03 (7.78)	0.0018	21.72 ± 0.51 (2.36)
HA_v8	0.03	8.30 ± 0.27 (3.22)	9.21 ± 0.27 (2.96)	0.0015	18.67 ± 1.19 (6.36)

The influence of different FTIR equipment on the results was also studied. The same sample pellets (prepared with KBr) was measured on two different FTIR machines (*Nicolet iS50, Thermo Fisher Scientific*, and *Frontier FT-IR/FIR, Perkin Elmer*) using the same measuring parameters. Four KBr pellets of the same sample (standard HA) was measured and averaged. The calculated OH^-/PO_4^{3-} value (using OH^- at 632 cm^{-1}) from *Nicolet* was 0.38 ± 0.012 and OH^-/PO_4^{3-} from *Frontier* was $0,39 \pm 0,010$. OH^- concentration measured by *Frontier* was 3% larger than using *Nicolet*. This also explains the difference in results when calculating OH^- amount using a calibration curve or just assuming that standard HA is 100% hydroxylated, because all FTIR measurements of OHA samples were done using *Nicolet* while HA/FA samples were measured by *Frontier*. It is therefore recommended to use the same equipment to ensure the validity of the results, or to make additional experiments to understand the differences in the measured values. It must be also mentioned that the standard deviation of the measurements from both machines is up to 3% with relative standard deviation up to 8%. Although the tendency of slightly different results depending on the equipment used was observed, it could be neglected because of the measurement error.

Sample preparation technique mixing powder with paraffin oil 'Nujol' was also tested. This technique is faster and avoids moisture adsorption from the atmosphere. However, some of absorption lines from 'Nujol' (sourced from *Sigma-Aldrich (Lot BCBJ1469V)*) aligns with absorption lines of HA (Fig. 3.13-a). Even after subtracting Nujol spectra as a background, obtained sample spectra was distorted and could not be used for precise calculations of OH^- ions (Fig. 3.13-b).

The accuracy of OH^- measurement depends on drying the sample and KBr, and also the trituration method. Sample must be dried before the FTIR measurements in order to avoid or lessen the adsorption bands from absorbed water. It is also necessary to dry KBr as it is very hygroscopic. Previous experiments in Master thesis [57] showed that fluorapatite mixed with vacuum heated KBr has smaller peak at 3537 cm^{-1} (from an F$\cdots$OH$\cdots$F bond [183]) compared to the oven heated KBr powder. The second important factor was trituration with a preference to lightly combining KBr with the already milled powder. Mechanical milling of sample and KBr can more easily introduce water molecules in the sample and even lead to the changes of OH^- amount [34]. Homogeneous sample distribution in KBr pellet is another factor influencing the result, and it is almost impossible to prepare two identical pellets. Thereby for more precise quantitative results at least 3 sample pellets should be prepared and the average result calculated.
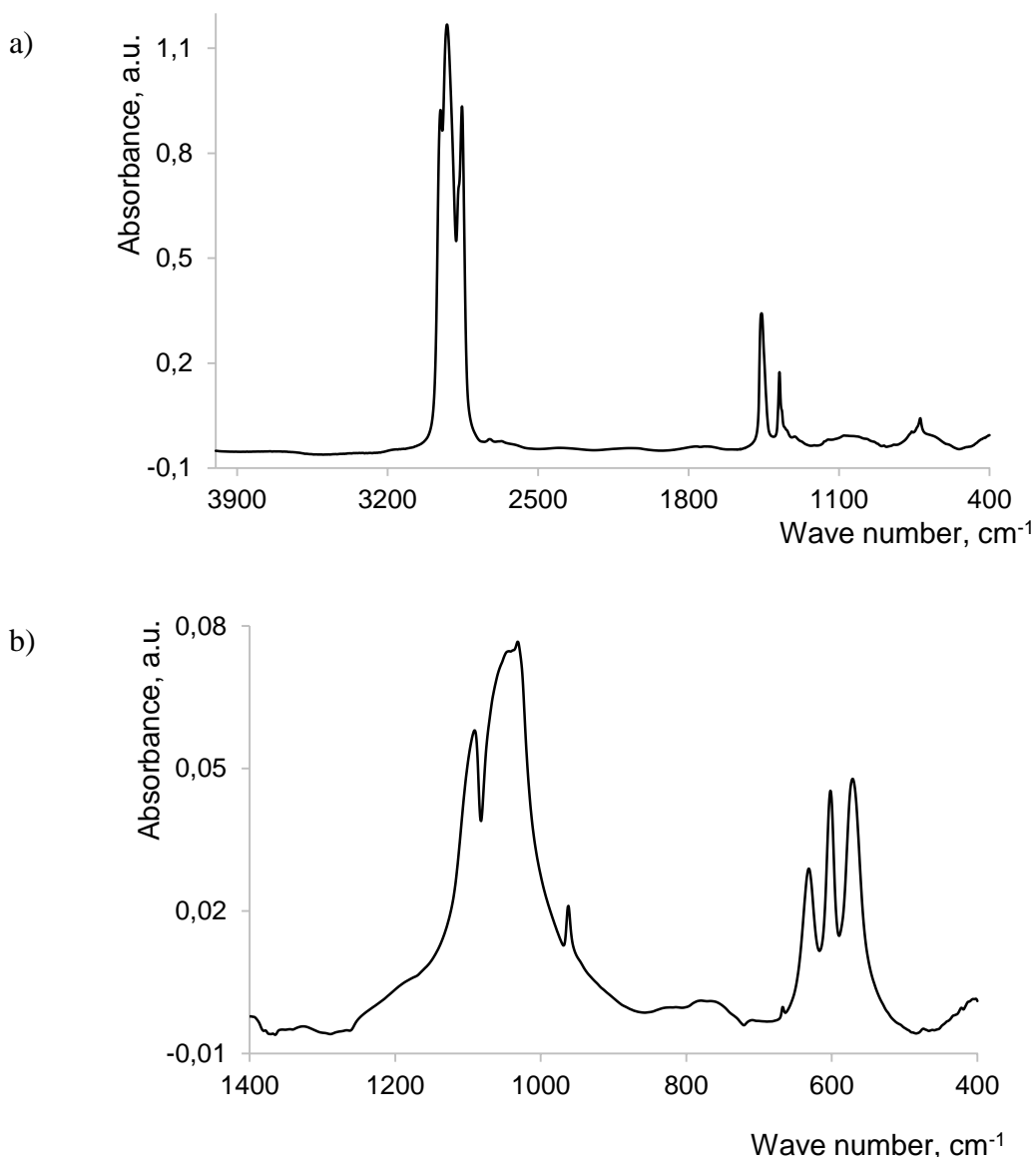
Fig. 3.13. FTIR spectra of (a) Nujol, and (b) standard HA prepared with Nujol.

Any disturbance to the crystal structure around the OH^- ion may potentially affect the absorption peak area. When the surrounding ions become disordered then the OH^- vibration or libration will be disrupted, and the absolute peak intensity will change [16]. Where some OH^- are in a disordered state, then there would be a reduction in the OH^- absorption peak intensity. One such case is with a decrease in crystal size. For a given mass, smaller crystals will present more ions close to the crystal surface, where there is more disorder. Similarly, in a solid material with finer grain size, more ions will be confined to the grain boundary. In both situations, a larger proportion of ions on the surface or in the grain boundary will affect the intensity of the molecular ion absorption band, giving possibly variable intensity ratios for similar contents.

For measuring the OH⁻ content, it is therefore recommended to heat-treat the hydroxyapatite for a high crystallinity, similar to the reference used for making the calibration curve.

3.1.4. Raman spectroscopy

Quantification of the hydroxyl ion concentration can also be achieved with Raman spectroscopy. Advantage of this method compared to FTIR is the absence of time-consuming sample preparation, also no additional reagents (as hygroscopic KBr) are needed. Using micro-Raman spectroscopy even microsized areas of the sample (for example HA coating) could be studied, which opens doors to mapping the hydroxyl concentration across a surface.

The same OH⁻ calculation technique as described in previous section was used: area of OH⁻ vibrational peak at 3570 cm⁻¹ (spectral range between 3560 and 3590 cm⁻¹) relative to the area of ν_1 PO_4^{3-} vibrational peaks in spectral range between 920 and 990 cm⁻¹ was calculated (Fig. 3.14). The same spectral range was used to calculate all samples. Dehydroxylation leads to the distortion of the apatite structure as can be observed by the broader peaks for a sample with lower OH⁻ concentration (Raman spectra of all OHA samples are included in Appendix 6). The splitting of ν_1 PO_4^{3-} vibrational line for oxyhydroxyapatites has already been reported suggesting that additional bands at 950 and 972 cm⁻¹ are characteristic to oxyapatite [93]. Table 3.8 summarizes the calculated ratio of the OH⁻ peak area relative to the PO_4^{3-} peak area.
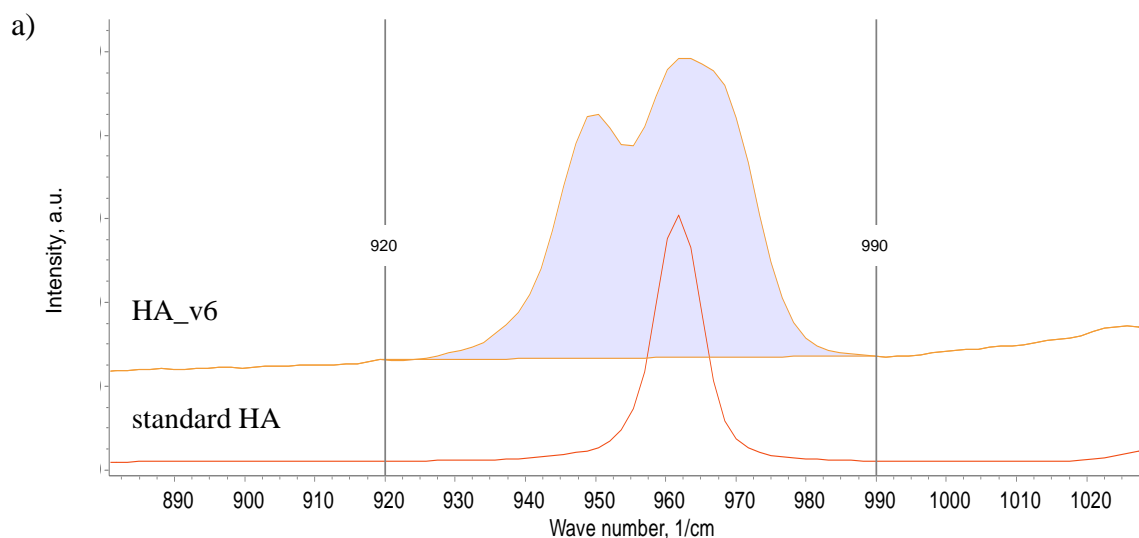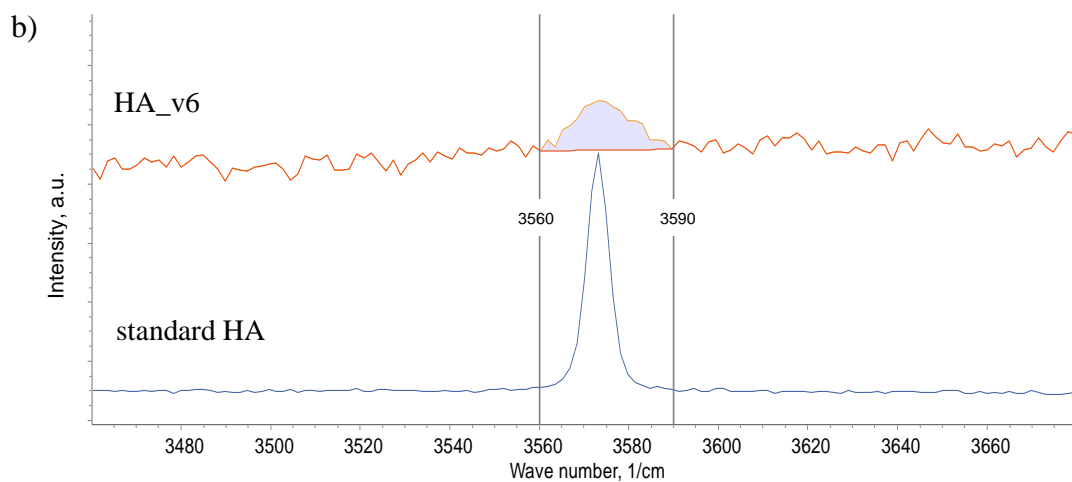
Fig. 3.14. Highlighted (a) PO_4^{3-} and (b) OH^- vibrational peak areas for the calculation of OH^- amount from Raman spectra.

Table 3.8.

Hydroxyl ion (at 3590 - 3560 cm^{-1}) and phosphate ion (at 990 - 920 cm^{-1}) absorption band areas of OHA measured from Raman spectra

Sample name	OH^- peak area, a.u.	ν_1 PO_4^{3-} peak area, a.u.	OH/ PO_4	Average (OH/ PO_4) ± stdev (RSD, %)
Standard HA	27020	138300	0.20	0.20 ± 0.012 (6.21)
	26350	138900	0.19	
	12770	69170	0.18	
	5564	25450	0.22	
	6512	31490	0.21	
	11200	54830	0.20	
HA_v8_reh700	63900	335600	0.19	0.19 ± 0.002 (0.80)
	70600	367900	0.19	
	59730	308700	0.19	
HA_v8_reh400-1h	76170	756500	0.10	0.10 ± 0.002 (1.51)
	48580	488200	0.10	
	38900	398100	0.10	
HA_v8_reh400	39440	451900	0.09	0.08 ± 0.003 (3.05)
	63200	769700	0.08	
	37680	444000	0.08	

HA_v8_reh350	49370	846900	0.06	0.06 ± 0.006
	36100	715600	0.05	(10.76)
	39380	629500	0.06	
HA_v6	3855	219400	0.02	0.02 ± 0.007
	4785	384500	0.01	(38.35)
	13100	489300	0.03	
HA_v8	7048	439300	0.02	0.01 ± 0.003
	8805	748900	0.01	(25.97)
	4035	416800	0.01	

The OH^- concentration calculated assuming that the standard HA is fully hydroxylated was compared between Raman and FTIR methods (Table 3.9). It was noticed that Raman results show about 20 – 30 % less OH^- in the samples compared to FTIR results. This observation is consistent for all samples. The relative stnadard deviation is also very large for the samples with low amount of hydroxyl groups (up to 38%). Although this result fits with the theory - polar bands have weak Raman scattering signal [94], a quantitative representation has not been showed before. This is an important finding especially because many apatite researchers use Raman spectroscopy to charectarize hydroxyl ions in materials [16, 46, 189].

Table 3.9.

The amount of hydroxyl ions in OHA samples calculated from Raman and FTIR spectra

Sample name	from Raman	from FTIR	OH^- (Raman)/
	OH^- amount ± stdev, % (RSD, %)		OH^- (FTIR)
	Assuming standard HA is 100%		
Standard HA	100	100	
HA_v8_reh700	96.02 ± 0.77 (0.80)	98.57 ± 0.89 (0.91)	0.97
HA_v8_reh400-1h	49.68 ± 0.75 (1.51)	67.47 ± 2.62 (3.88)	0.74
HA_v8_reh400	42.40 ± 1.29 (3.05)	58.50 ± 2.21 (3.78)	0.72
HA_v8_reh350	28.56 ± 3.07 (10.76)	37.34 ± 2.26 (6.04)	0.76
HA_v6	9.47 ± 3.63 (38.35)	12.22 ± 1.01 (8.24)	0.77

HA_v8	6.25 ± 1.62 (25.97)	8.30 ± 0.27 (3.22)	0.75

The unstable nature of oxyapatite has been previously reported [41], and some concerns have been raised about possible sample degradation and decomposition during a long-term laser irradiation [84, 95]. To evaluate the influence of laser irradiation on the stability of oxyapatite sample, an experiment was performed irradiating HA_v8 and HA_v8_reh350 samples for 100 min with a 514.5 nm laser (100% power) and recording a Raman spectrum every 20 min. Results are summarized in the Table 3.10 and it can be seen that no significant difference for either of the samples was detected (standard deviation for Raman results is up to 4%). To statistically evaluate the results one sample t-test (using *GraphPad Prism* software) was also performed. P value was 0.989 for sample HA_v8 and 0.997 for sample HA_v8_reh350, which indicates that the results were not significantly different. That allows to conclude that the heat produced from the laser does not influence the OH$^-$ amount of the sample, and the produced oxyhydroxyapatite samples are stable under normal ambient conditions.

Table 3.10.

The amount of hydroxyl ions in OHA samples calculated from Raman spectra with different laser irradiation times

Irradiation time, min	HA_v8		HA_v8_reh350	
	OH$^-$/PO$_4^{3-}$	OH$^-$, %	OH$^-$/PO$_4^{3-}$	OH$^-$, %
0	0.015	7.709	0.057	28.510
20	0.012	5.775	0.054	26.876
40	0.014	7.147	0.056	27.898
60	0.013	6.274	0.048	24.113
80	0.014	7.029	0.054	27.012
100	0.014	7.252	0.057	28.537

3.1.5. Guidelines for the quantification of hydroxyl ions in hydroxyapatite

Thermal gravimetric analysis can indicate the OH$^-$ ion concentration from water loss by heating hydroxyapatite or in a thermal reaction that encourages release of water at lower temperatures. The thermal reaction can be made between hydroxyapatite and calcium pyrophosphate or calcium fluoride if hydroxyapatite does not contain any other volatile phases, such as carbonate. The following steps are required to determine the OH$^-$ content:

- the sample should be characterized with other methods (at least XRD and FTIR) to make sure that it does not contain other phases or elements which might interact with reagents used for thermal reaction and/or have an additional weight loss in the same temperature range as the removal of hydroxyl ions;
- the sample and reactant (CPP or CaF_2) must be dried before mixing together to minimize the amount of adsorbed water;
- the reactant should be used in excess to ensure that the hydroxyapatite was completely reacted with the thermal reaction powder;
- larger amount of mixture than needed for the TGA experiment should be prepared to ensure better homogenization during grinding;
- a homogeneous mixture must be prepared, sufficient time and care must be given to the grinding process;
- thermal gravimetric analysis should be performed in a moisture free atmosphere to avoid rehydroxylation of the sample;
- two mass losses should be calculated and separated from the TGA results: mass loss till 400 °C corresponds to the water, mass loss from 400 °C corresponds to the removal of hydroxyl ions;
- dry mass of hydroxyapatite in the mixture must be calculated, using HA/reactant ratio used for the reaction and the mass loss due to the adsorbed water (from TGA curve);

$$dry\ mass\ of\ HA = \frac{dry\ mass\ of\ mixture\ \times mass\ of\ HA\ in\ mixture}{mass\ of\ mixture}$$

$$dry\ mass\ of\ mixture = mass\ of\ mixture - mass\ loss\ of\ water$$

- the loss of hydroxyl groups in hydroxyapatite can be calculated as a percentage using the mass loss of the reaction from the TGA results (mass loss of adsorbed water should not be included here);

$$mass\ loss\ of\ OH^- = \frac{mass\ loss\ of\ reaction}{dry\ mass\ of\ HA}$$

- the amount of OH^- in the sample as a percentage can be calculated using molar mass of HA (M_{HA}) and molar mass of hydroxyl ions (M_{OH});

$$OH^-(\%) = \frac{mass\ loss\ of\ OH^-\ \times\ M_{HA}}{M_{OH}}$$

- the sample after TGA reaction should be tested with other methods (at least XRD and FTIR) to make sure that the reaction was complete (no HA phase should be detected).

Fourier transform infrared spectroscopy will directly identify the presence of OH⁻. FTIR offers a faster and easier quantification of hydroxyl groups compared to thermal gravimetric analysis. As the hydroxyl ions have a separate absorption line it is not influenced by other phases. The following steps are recomended to obtain precise results:

- the sample and KBr must be dried to minimize the effect of adsorbed water;
- the sample should be well ground in a mortar before adding KBr;
- small amount of the ground sample should be lightly mixed with KBr (200 mg was used in this research) to form a homogeneous mixture, and pellet should be made by uniaxial pressing. Mechanical mixing of the sample with KBr should be avoided as it can disturb the crystal lattice of the sample or even change the hydroxyl ion concentration;
- the amount of the sample in the KBr pellet should be similar for all measurements, it can be checked by the absorption intensity of the recorded spectra, the maximum intensity should be in range 0.8 to 1.2 a.u.;
- at least 3 replicate samples (3 individual samples taken from the ground powder mixture) should be analyzed and the calculations averaged;
- the same equipment parameters should be used for all measurements (in this research a resolution of 4 cm⁻¹ was used and a total of 64 scans per measurement were taken);
- if different equipment is used additional experiments should be made to understand the differences in the measured values;
- hydroxyl ion absorption peak at 632 cm⁻¹ should be used (instead of OH⁻ absorption peak at 3570 cm⁻¹), as it is more sensitive;
- to separate the hydroxyl ion absorption peak from the phosphate peaks, deconvolution of the spectral range 500 – 700 cm⁻¹ should be performed. The same deconvolution model should be used for all samples;
- area of the OH⁻ absorption peak at 632 cm⁻¹ and the sum of ν_4 phosphate absorption peaks should be measured;
- the ratio of the peak areas (OH⁻/PO_4^{3-}) should be calculated;
- to calculate the amount of OH⁻ in the sample, a calibration curve should be used or the calculated value should be compared to the OH⁻/PO_4^{3-} ratio of a hydroxyapatite with 100% OH⁻ (standard hydroxyapatite). In this research:
  - the equation from the calibration curve: $x = \frac{y + 0,0027}{0,0037}$, where x is the concentration of OH⁻ in the sample (%) and y is the OH⁻/PO_4^{3-} ratio

- OH$^-$/PO$_4$$^{3-}$ ratio for a 100% OH$^-$ containing hydroxyapatite is 0.38 ± 0.012

- the calculated average accuracy of the method is 6%, while the average precision is 2%.

3.2. PART 2 Influence of the hydroxyl ion content on the biological response of hydroxyapatite coatings

3.2.1. Preparation and characterization of hydroxyapatite coatings

XRD pattern (Fig. 3.15-a) demonstrated the phase composition of the commercial powder used for preparing HA coatings. Diffraction peaks confirmed a hydroxyapatite phase. Results from ICDD database also detected small diffraction peaks (almost at background level) characteristic of tetracalcium phosphate. Chemical bonding of HA powder revealed by FTIR spectroscopy (Fig. 3.15-b) showed vibrations characteristic of hydroxyapatite. Low intensities of OH$^-$ absorption peaks allowed to conclude that HA during commercial synthesis and thermal processing had lost most of its hydroxyl ions. Some additional absorption peaks at 427, 497 and 940 cm^{-1} were detected. Although absorption lines at 427 and 940 cm^{-1} might arise from both oxyapatite and/or tetracalcium phosphate, the presence of absorption line at 497 cm^{-1} undoubtedly proved the presence of tetracalcium phosphate [190]. Concentration of hydroxyl ions was measured from deconvulated spectral area at 500 – 750 cm^{-1}. The measurement of OH$^-$/PO$_4$$^{3-}$ was 0.08, which gives the OH$^-$ concentration of 22 ± 2% (full data about peak areas are included in Appendix 7).

The analysis of FTIR spectra and calculated OH$^-$ amount shows the lack of good quality control technique and detailed characterization of commercial products. Although the product was sold as hydroxyapatite powder for thermal spraying, analysis showed that it was an oxyhydroxyapatite with a small amount of decomposition phase.
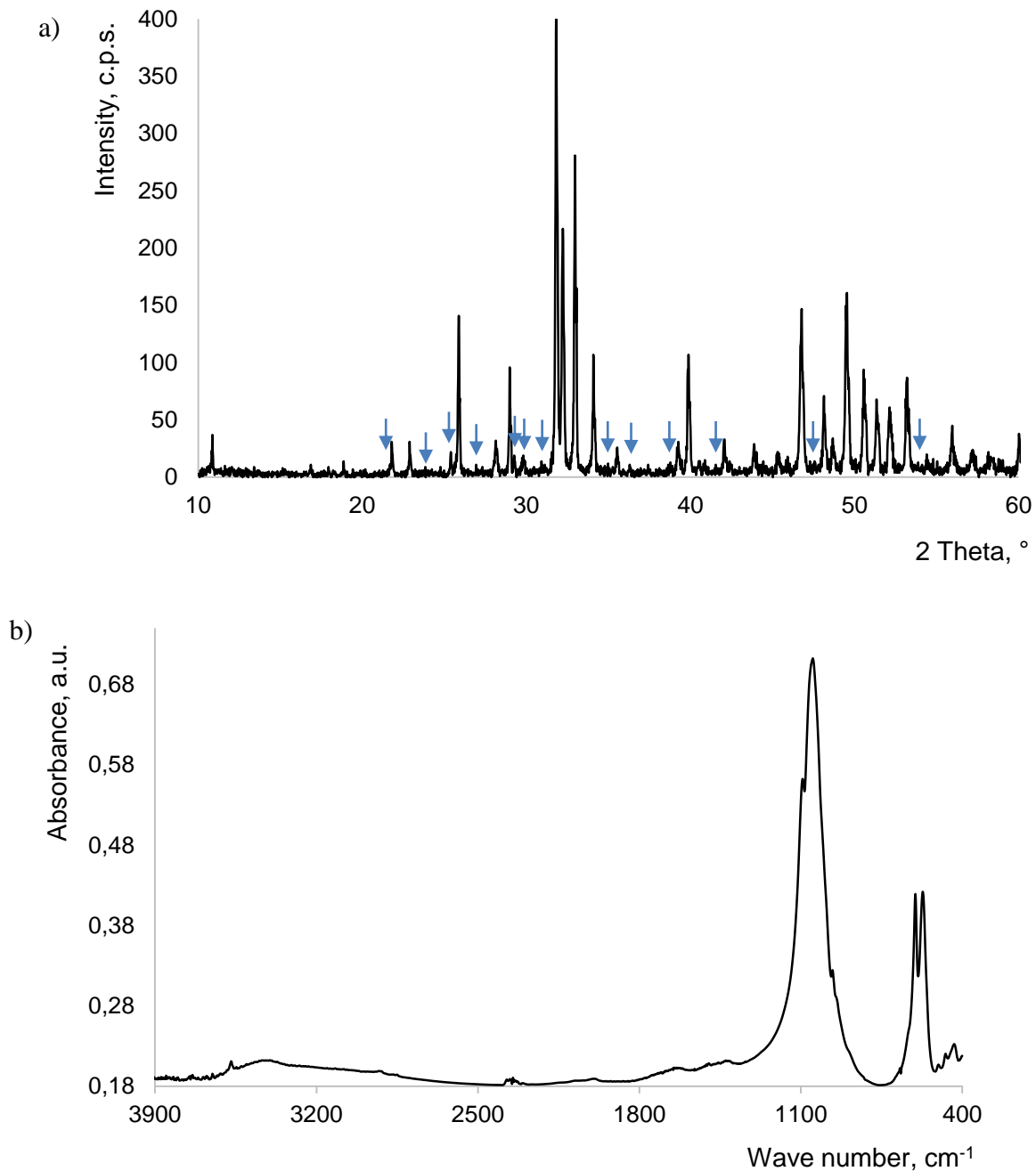
Fig. 3.15. XRD pattern (a) and FTIR spectrum (b) of the commercial HA powder. Blue arrows in XRD pattern indicates the presence of TTCP phase.

Two types of coatings were prepared to evaluate the influence of hydroxyl groups on the biological response – a conventional HA coating (cHA) and a hydrothermally processed HA coating (ht-cHA). Both type of coatings exhibited preferred <001> crystal orientation, as seen by the high intensity (002) and (004) diffraction peaks (Fig. 3.16-a). The phase composition examined by conducting X-ray diffraction on crushed coatings to reveal all peaks showed that all peaks are characteristic of hydroxyapatite (Fig. 3.16-b), although the high background noise

prevented to detect small quantities of decomposition phases if any were present. The lifted background around 20 – 30 °2Θ also indicated the presence of the amorphous phase. Nevertheless, the X-ray diffraction was able to show that hydroxyapatite was still present after spraying, and the parameters chosen for the spraying process was suitable to make a coating with oriented crystals.
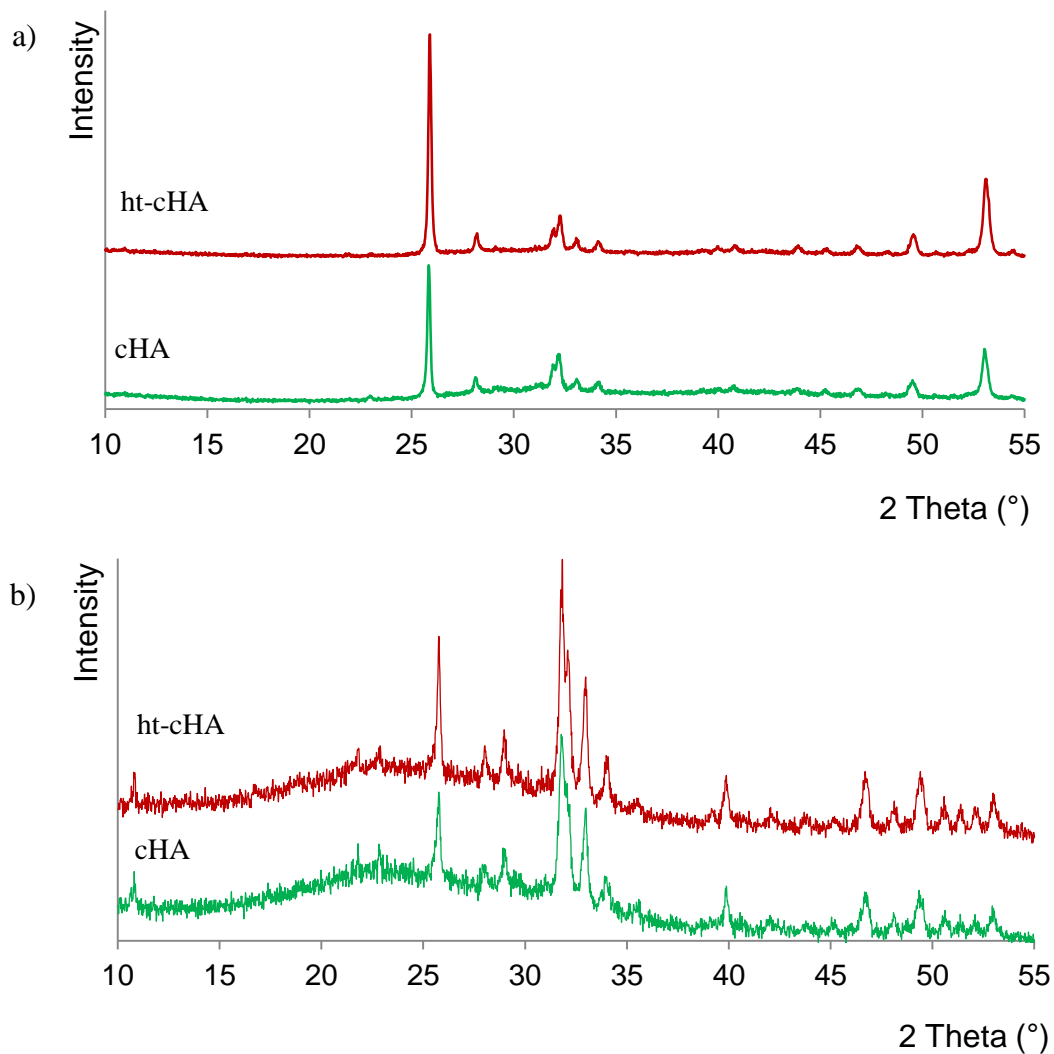
Fig. 3.16. X-ray diffraction of the as-sprayed (a) and the crushed (b) HA coatings.

Half of the coatings were hydrothermally processed to restore hydroxyl ions that were depleted during thermal spraying of HA. FTIR results of as-sprayed and hydrothermally treated coatings are shown in Fig. 3.17. Similar as with the commercial powder, absorption bands characteristic to HA, OAp and TTCP were observed. Deconvolution of the spectral range at 750 – 500 cm^{-1} was performed to calculate the amount of hydroxyl ions. The calculated OH^- /PO_4^{3-} ratio for cHA coatings was 0.04, and for ht-cHA coatings it was 0.16 (full data about

peak areas are included in Appendix 7). Comparing the calculated OH^-/PO_4^{3-} ratio to the standard HA gave the hydroxyl ion concentration, which is $11 \pm 2\%$ for cHA and $41 \pm 4\%$ for ht-cHA.

Although the hydrothermal treatment had not only restored the OH^- which was lost during the thermal spraying, but also had increased the hydroxyl ion concentration compared to the initial commercial powder, the overall OH^- concentration for the coatings was still low. The reason for that is the distorted structure of hydroxyapatite after thermal spraying. As a result of a very high temperature during the spraying process HA powder particles become partially or fully melted. When they hit the substrate, quenching and crystallization process starts. Depending on the quenching speed and the level of dehydroxylation or even decomposition of the particle, crystalline and amorphous phases forms [61]. The presence of amorphous phase prohibits to calculate the true value of hydroxyl ions in the coating. The partial decomposition of HA is another reason for smaller amount of OH^- in the coating.
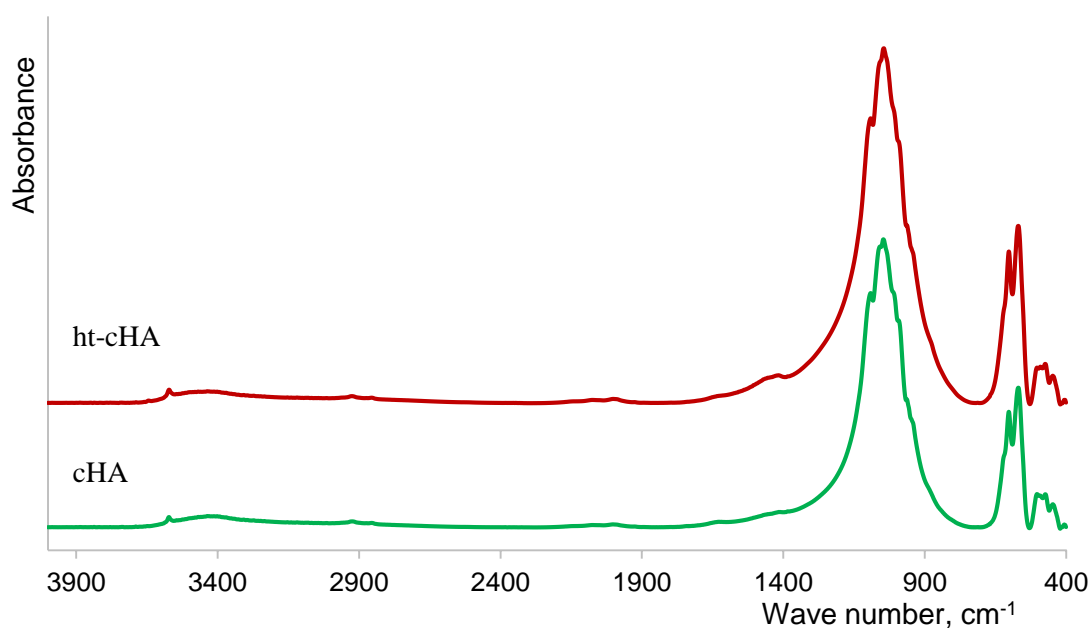
Fig. 3.17. FT-IR spectra of cHA and ht-cHA coatings.

As it is believed that the hydroxyl ions have an important role in the ionic conductivity of HA [138], and some studies have shown that the post treatment of HA ceramics in water vapour increase the conductivity of the material (no information about the actual OH^- amount was given) [136, 137, 150], for the full characterization of the HA coatings surface potential was also measured. To ascertain whether the concentration of hydroxyl ions in HA structure influenced the surface potential it was first necessary to align the OH^- groups in one direction.

Polarization at elevated temperature under the electric field supplied sufficient energy to reorient OH$^-$ ions from all columns within one direction [135]. Kelvin probe AFM measurements showed that hydroxyapatite coating with more OH$^-$ ions in the structure possessed a higher surface electric potential (Fig 3.18). In order to determine the statistical significance, unpaired t-test was performed (using *GraphPad Prism* software).
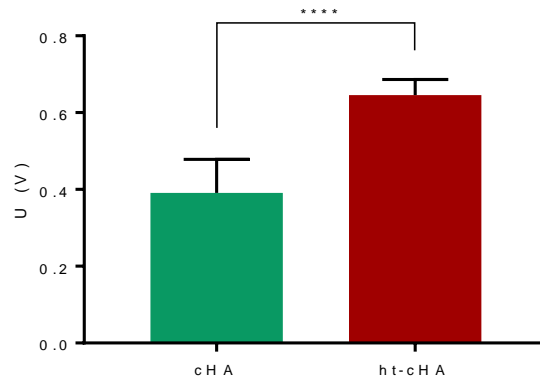
Fig. 3.18. Electrical surface potential of the conventional and hydrothermally treated HA coatings (**** P < 0.0001).

The surface of the coating is showed in SEM images (Fig. 3.19). HA coating showed smooth surface from well-molten round HA particles which are obtained by spraying onto a preheated substrate [118]. Some micro cracks can also be observed.
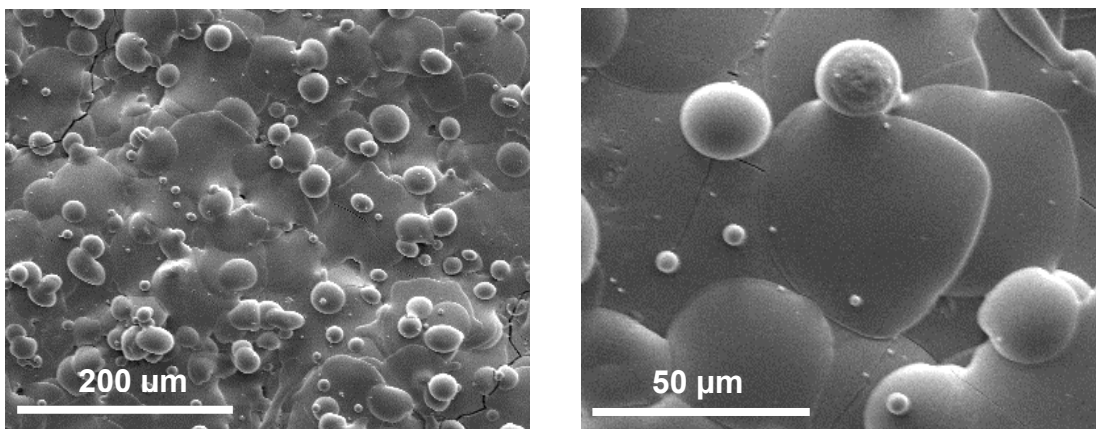
Fig. 3.19. SEM images of the surface of hydroxyapatite coating.

Profilometry measurements gave information about the surface roughness and average thickness of the coatings (Fig. 3.20). Calculated surface average roughness S_a was 9.56 µm. This corresponds to other results where coatings were prepared using similar spraying parameters [118]. The average thickness of the coating is 55 µm, it varies mostly between 35

and 70 μm. The distribution of the thickness is even along the surface, which can be seen from the surface roughness distribution graph (Fig. 3.20-b), and the isotropy measurement S_{tr} which is 0.78.

a)

b)
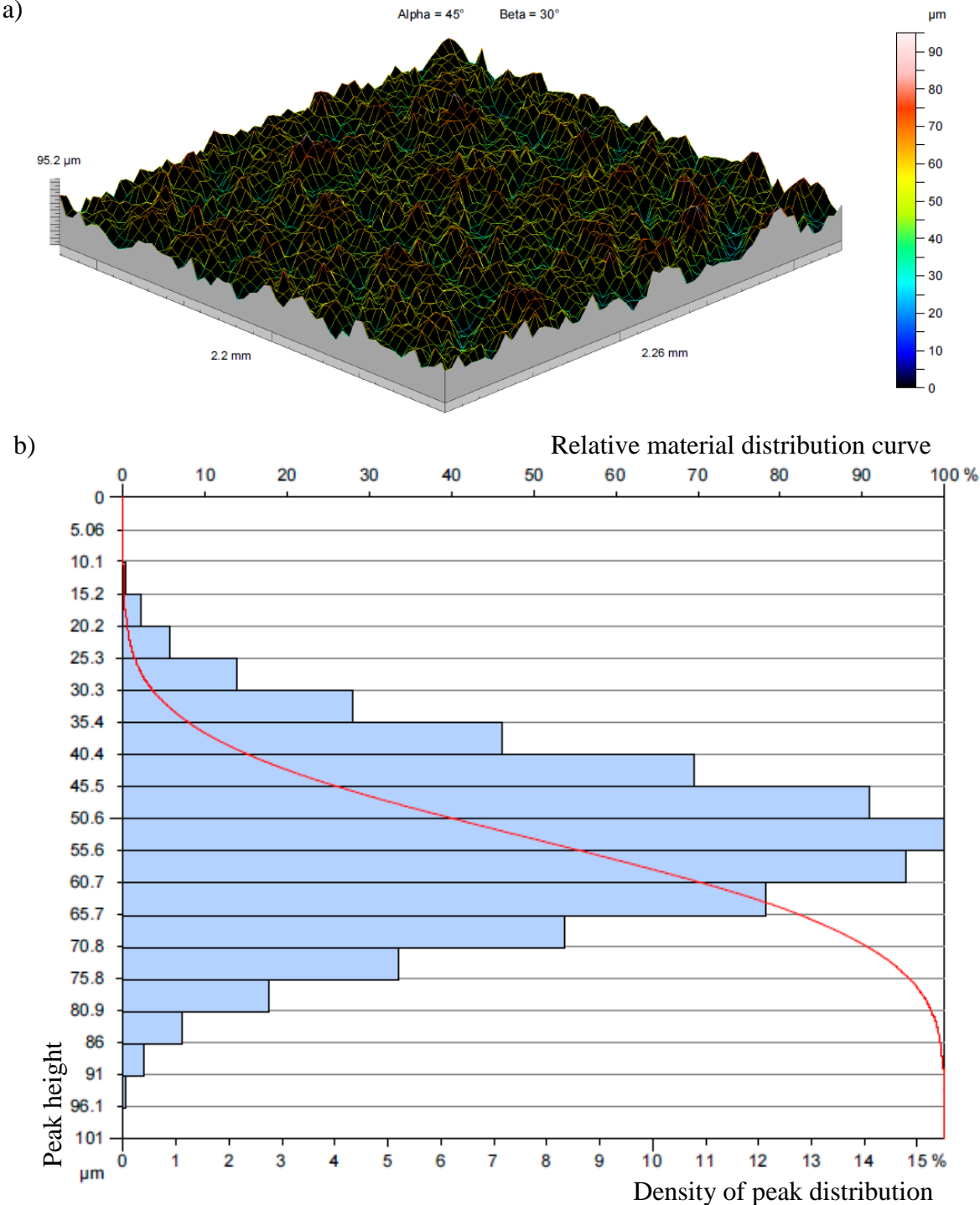
Fig. 3.20. 3D model of the separated roughness (a) and surface roughness distribution graph (b) of hydroxyapatite coating.

Hydroxyapatite coatings used for this study had been designed to have as organized structure as possible. This was achieved in three steps. Firstly, the coatings were sprayed onto pre-heated metal to orient the crystals. Secondly, after spraying, vacant hydroxyl ion sites were filled, by placing the coating in water vapour, and, finally, orientating the OH$^-$ ions under an electric field. The combined use of crystal orientation and hydroxyl ion orientation achieves the maximum charge possible. A material design from the core to the surface is seldom found in orthopaedic biomaterials.

3.2.2. Evaluation of the biological properties of hydroxyapatite coatings

Bone forming cells – osteoblasts – were grown on HA coated discs and *in-vitro* tests were carried out as described in the methods. Performed tests validated the ability of both coatings to act as a suitable support platform for attachment and growth of osteoblasts. Figure 3.21 shows the representative image of a cell on conventional and hydrothermally treated HA coatings. Stretched cell protrusions on the ht-cHA coating suggested that the cells were healthier and more active compared to the cells on the cHA coating. Confocal image reveals cell nucleus and cell morphology and cytoskeletal features. It can be seen that already after 1-day cell culture osteoblasts were spread out and binding with one another. On a larger scale this is demonstrated in Figure 3.22, which also shows elevated cell adhesion on the ht-cHA coating after 1-day cell culture compared to cHA. A significant increase in the number of cells on both coatings after 14-day cell culture was observed.
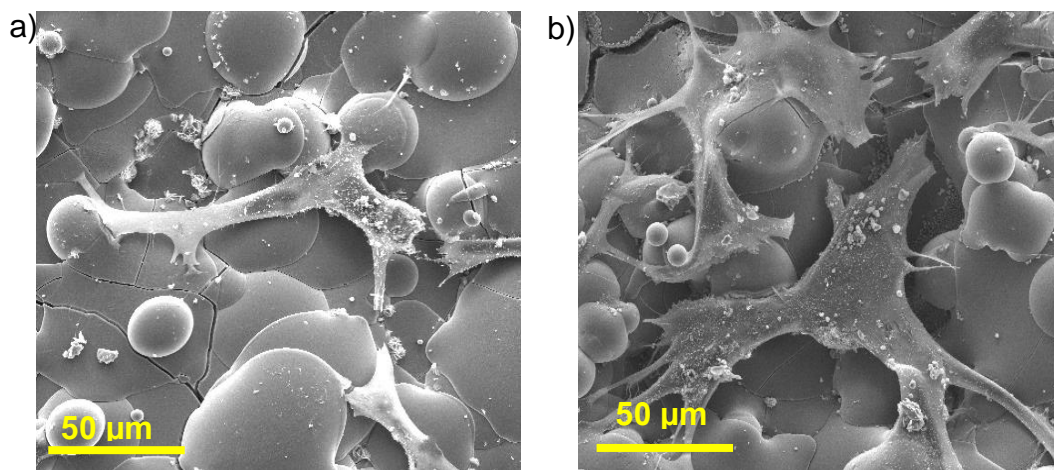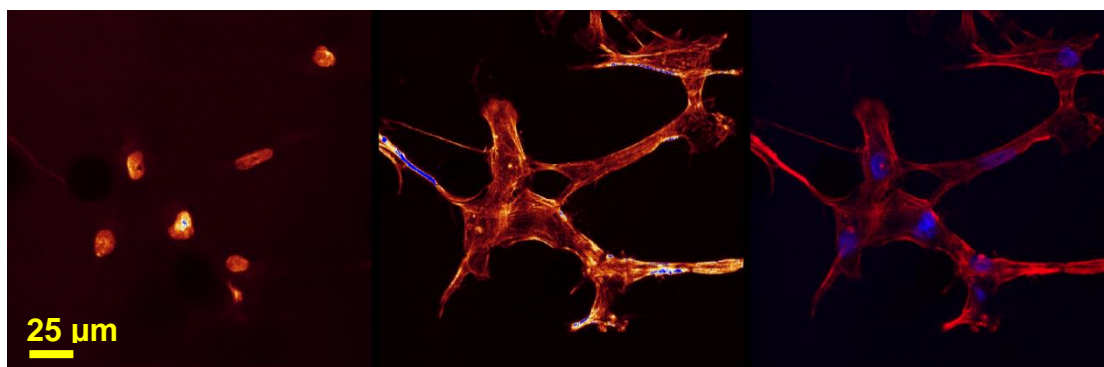
Fig. 3.21. SEM images of osteoblast coverage on the conventional (a) and hydrothermally treated (b) HA coating after 1 day, and confocal image of osteoblast coverage on the hydrothermally treated HA coating after 1 day (cell nuclei on the left, cytoskeleton in the middle and combined image on the right).

SEM and confocal images were used to calculate the cell coverage and cell count on the coatings. The calculation principle is described in the methods section, and the results are summarized in the Table 3.11 including the calculated standard error for each sample. Both, the cell count and cell coverage results show the same tendency – there are more attached cells on the HA coating with higher OH^- amount after 1-day cell culture. Both measurements demonstrate about 50% more cells on the ht-cHA. However, in the course of time the cell number on both samples equalizes as evidenced by the results after 14-day cell culture.

There are several reasons for the big standard error in the cell count and cell coverage calculations. The cells were counted manually, based on the visible information – the approximate area of cells in SEM images, and the visible cell nuclei in confocal images. Because of the roughness of the samples, not all areas of the sample surface were in a good focus (especially for confocal images). After 14 days cell culture, cells were growing on top of each other, which made it impossible to see all cell nuclei. Some of the samples did not have a uniform cell distribution along the surface, but this impact was reduced by taking several images in randomly chosen places from one sample. Another and probably the most significant reason for the large differences in the results are the differences in the cell performance from different donors. For better statistical results at least 6 donors should be used.
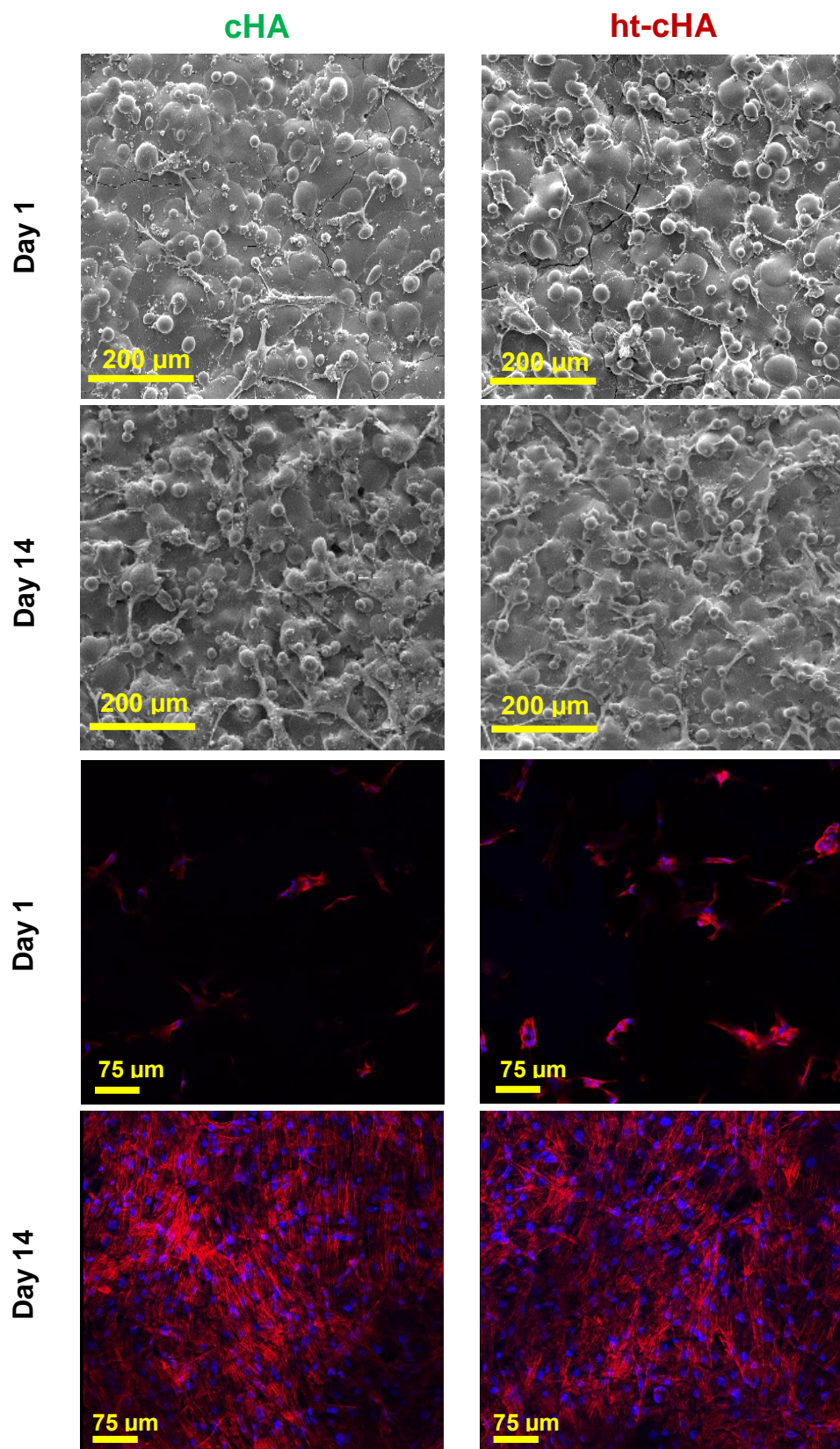
Fig. 3.22. SEM and confocal images of osteoblast coverage on the conventional and hydrothermally treated HA coatings after 1 and 14 days.

Table 3.11.

Osteoblast cell count per 1 mm^2 and cell coverage (% of total area) on conventional and hydrothermally treated HA coatings after 1 day and 14 days cell culture

Sample type	Cell count, cells/mm^2		Cell coverage, %	
	day 1	day 14	day 1	day 14
cHA	35.2 ± 5.21	608 ± 284	4.40 ± 1.03	39.6 ± 6.39
ht-cHA	73.7 ± 20.9	611 ± 234	7.40 ± 1.36	32.2 ± 6.47

Cell count based on visible nucleus from confocal images. Cell coverage calculations based on SEM images.

Gene expression profiling was performed to assess transcriptional activity, in terms of mRNA[4] encoding markers associated with osteoblast differentiation and bone matrix formation. PCR analysis of mRNA expression after osteoblast were grown for 7 days on the HA coatings showed an increase in the expression of genes related to osteoblast growth, maturation and transition into the osteocyte phenotype on hydrothermally treated coatings (Fig. 3.23). Collagen type I (Col1a1), runt-related transcription factor 2 (RUNx2), osteocalcin (OCN) and osteopontin (OPN) are some of the most important genes expressed by osteoblasts which contribute to the formation of the osseous matrix and controlled calcification. Different bone matrix proteins have different functions in bone formation.

The Col1a1 marker, essential for osteoid formation and subsequent mineralization, is expressed from the early stages of osteoblast differentiation. It is the major bone matrix protein, which binds to hydroxyapatite crystal to provide bone with enough biomechanical strength [191]. PCR results show no difference in the expression of this marker for both types of coatings after 7 days, but higher expression of Col1a1 after 14 days indicates that ht-cHA coatings might enhance osteoid deposition.

Hydrothermally treated coating showed increased expression of RUNx2 marker after both, 7 and 14 days cell culture. This marker is also essential for bone formation as it triggers the expression of major bone matrix genes during the early stages of osteoblast differentiation. This allows osteoblasts to undergo differentiation into mature osteoblasts that have increased expression of other important bone genes – osteocalcin and osteopontin. OCN is a major noncollagenous protein component of bone extracellular matrix, synthesized and secreted exclusively by osteoblastic cells in the late stage of maturation, and is considered indicator of

---

[4] Messenger RNA (mRNA) is a large family of RNA molecules that convey genetic information from DNA to the ribosome, where they specify the amino acid sequence of the protein products of gene expression.

osteoblasts differentiation. Osteocalcin is believed to play positive role in controlling nucleation of hydroxyapatite crystals [192]. OPN is a marker for osteoblastic differentiation and is expressed in early stages as well as in the post-proliferative period of osteoblastic growth. The expression of this gene also provides evidence of osteoblastic differentiation in these cells. Moreover, OPN promotes cell attachment to bone matrix [193].

Both, osteocalcin and osteopontin expression was enhanced on ht-cHA after 7 day cell culture, but it slightly decreased after 14 day incubation. It must be noted that compared to the other two markers (Col1a1 and RUNx2), the expression of OCN and OPN is smaller (values in 10^{-3} order), which was expected because these are the late stage markers.

The main reason for large standard errors, similarly to the cell attachment results, was the use of osteoblasts from just 3 donors. As the donor age and gender is not known, different cell activity can be expected. This was also observed from gene expression results, where some donors showed significantly different response (see Appendix 8). Nevertheless, similar tendency was observed from all biological tests indicating enhanced initial osteoblast activity for the HA coatings with larger amount of hydroxyl ions. Faster cell attachment and maturation could be an important factor to improve the implantation process by faster implant acceptance into the body, thus reducing risks of inflammation and implant rejection.
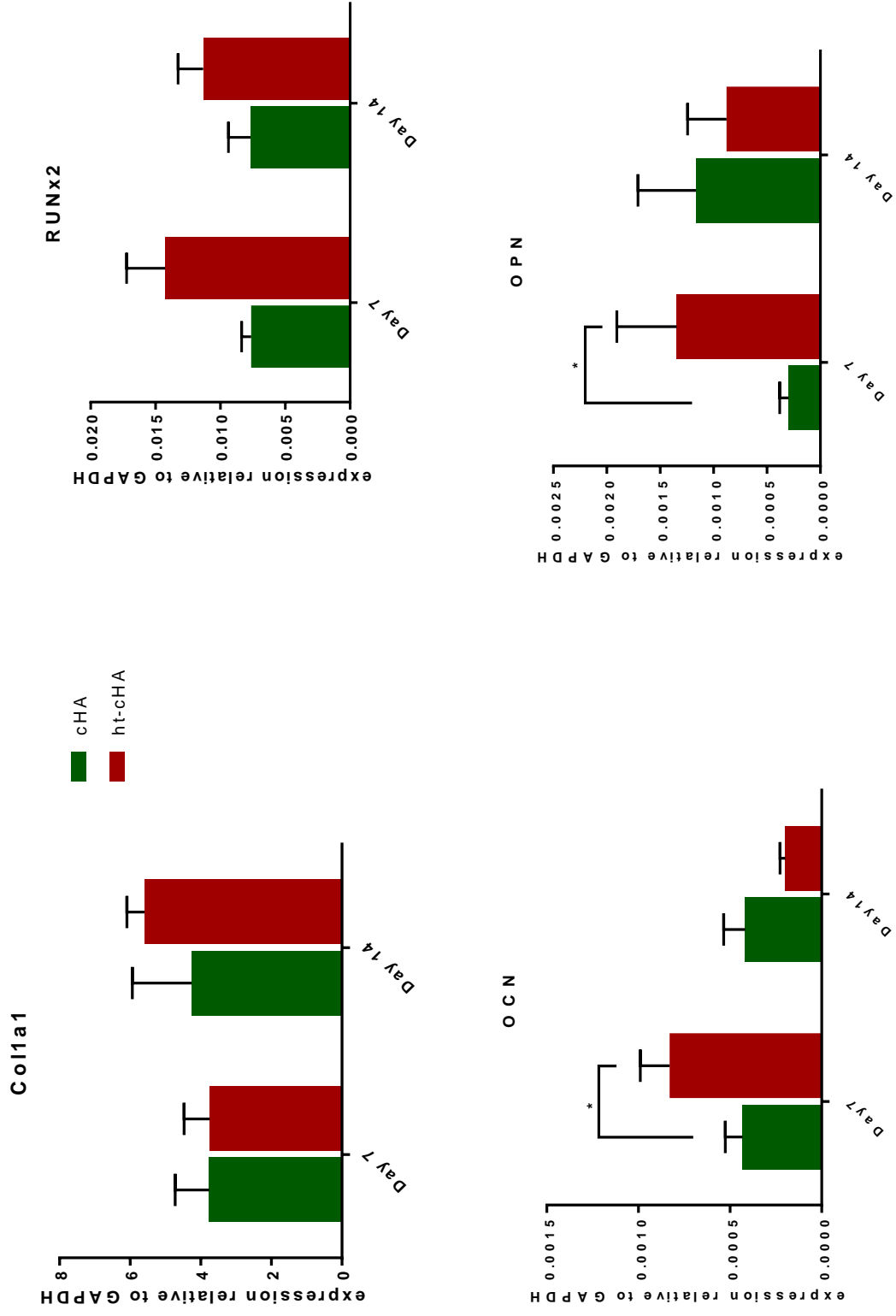
Fig. 3.23. Expression of bone cell markers in osteoblasts grown on conventional (cHA, green) and hydrothermally treated (ht-cHA, red) HA coatings after 7 and 14 days cell culture (* P ≤ 0.05).

CONCLUSIONS

PART 1 MEASUREMENT OF HYDROXYL ION CONTENT IN HYDROXYAPATITE

1. Thermal gravimetric analysis using hydroxyapatite thermal reaction with calcium pyrophosphate or calcium fluoride can be used for quantification of hydroxyl ions in hydroxyapatite if it does not contain other volatile phases.

2. Calibration curve for determination of hydroxyl ion content in hydroxyapatite has been developed using Fourier transform infrared spectroscopy. This method is linear in the range of the hydroxyl ion concentration of 0 % to 100% with a coefficient of determination of 0.9921, and allows quantifying the hydroxyl ion amount with an average precision of 2% and average accuracy 6%.

3. Both hydroxyl ion absorption lines in Fourier transform infrared spectra (at 632 and 3570 cm^{-1}) can be used for the quantification of hydroxyl ion amount in hydroxyapatite with more than 50% hydroxyl ions, but only the absorption line at 632 cm^{-1} gives precise quantitative results if the sample contains less than 50% hydroxyl ions.

4. Raman spectroscopy is less sensitive for the detection of hydroxyl ions, and shows about 20 – 30% less hydroxyl ions in oxyhydroxyapatite samples compared to FTIR results.

5. Laser irradiation (up to 100 min using 100% power of 514.5 nm laser) by Raman spectrometer did not influence the hydroxyl ion amount in hydroxyapatite samples.

PART 2 INFLUENCE OF HYDROXYL ION CONTENT ON THE BIOLOGICAL RESPONSE OF HYDROXYAPATITE COATINGS

6. Increasing the hydroxyl ions concentration in hydroxyapatite coating for 30 % increased its surface electric potential 1.7 times.

7. Hydroxyapatite coatings with more hydroxyl ions increase the initial osteoblast adhesion for about 50% (based on the cell count and cell coverage measurements) and promote the initial maturation and differentiation of osteoblasts (based on RUNx2, OCN, OPN gene marker expression after 7-day cell culture).

8. The influence of hydroxyl ions content on the biological response of hydroxyapatite coating decreases over time, and after 2-week cell culture no significant difference can be observed.

APPROBATION OF THE THESIS

Book chapter

1. K.A. Gross, <u>L. Pluduma</u>. Putting oxyhydroxyapatite into perspective: A pathway to oxyapatite and its applications. Calcium Phosphates: Structure, Synthesis, Properties and Applications (Ed. R.B. Heimann), 2012, p.95-120, Nova Science Publishers. *SCOPUS*

Journal papers

1. <u>L. Pluduma</u>, E. Freimanis, K.A. Gross, H. Koivuoloto, K. Algate, D. Haynes, P. Vuoristo. Functionalizing surface electrical potential of hydroxyapatite coatings. Advances in Science and Technology, 102, 2017, p.12–17.

2. K. Tonsuaadu, K.A. Gross, <u>L. Pluduma</u>, M. Veiderma. A review on the thermal stability of calcium apatites. Journal of Thermal Analysis and Calorimetry, 110 (2), 2012, p. 647.- 659. *SCOPUS, Web of Science*

3. <u>L. Pluduma</u>, K. Salma, L. Berzina Cimdina. Thermal characterization of Hap/TCP bioceramics with variable phase reatio. European Cells and Materials, 20 (3), 2010, p.203. *SCOPUS*

Peer-Reviewed publications in conference proceedings

1. D. Ubele, <u>L. Pluduma</u>, A. Brangule, A. Berzina, H. Koivuluoto, P. Vuoristo, R. Juskenas, K.A. Gross. Investigations on the tailorability of hard tissue implant surfaces by printing. European Cells and Materials, 33 (1), 2017, p.203.

2. E. Freimanis, <u>L. Pluduma</u>, K.A. Gross, M. Kylmälahti, Y. Dekhtyar, H. Koivuluoto, P. Vuoristo. Flame sintered HAP adopted to bone properties. European Cells and Materials, 29 (1), 2015. p.9.

International conference presentations with published abstracts

1. D. Ubele, <u>L. Pluduma</u>, A. Brangule, A. Berzina, H. Koivuluoto, P. Vuoristo, R. Juskenas, K.A. Gross. Investigations on the tailorability of hard tissue implant surfaces by printing. Scandinavian Society for Biomaterials 10th Annual Meeting, Hafjell, Norway, March 15-17, 2017.

2. D. Haynes, <u>L. Pluduma</u>, K. Algate, D. Menicanin, K.A. Gross. Optimizing surface charge on hydroxyapatite coatings to promote mesenchymal stem cell development. ANZORS, Melbourne, Australia, October 13-15, 2016.

3. <u>L. Pluduma</u>, K.A. Gross, E. Freimanis, I. Daenke. Functionalizing surface electrical potential of hydroxyapatite coatings. 7th Forum on New Materials (CIMTEC 2016), Perugia, Italy, June 5.-9, 2016.

4. E. Freimanis, <u>L. Pluduma</u>, K.A. Gross, M. Kylmalahti, Y. Dekhtyar, H. Koivuluoto, P. Vuoristo. Flame sintered HAp adopted to bone properties. Scandinavian Society for Biomaterials 8th Conference, Sigulda, Latvia. May 6-8, 2015.

5. K. Gross, <u>L. Pluduma</u>, A. Ubelis, A. Kapralovs, P. Brangulis, G. Darut, G. Montavon. The unstable hydroxyl content in thermally processed hydroxyapatite. Bioceramics 26, Barcelona, Spain, November 6-8, 2014.

6. <u>L. Pluduma</u>, K.A. Gross. Producing a true hydroxyapatite with the necessary OH content. International Symposium on Apatite and Correlative Biomaterials (ISACB 6), Nantes, France, June 5.–8., 2013.

7. <u>L. Pluduma</u>, K.A. Gross. Develpment of new analysis tools for thermally sprayed hydroxyapatite. 5th Les Rencontres Internationales sur la Projection Thermique (RIPT), Limoge, France, December 7.-9., 2011.

8. <u>L. Pluduma</u>, K.A. Gross, L. Bērziņa-Cimdiņa, C. Rey. Scoping different approaches for the measurement of OH in hydroxyapatite. 23rd Symposium and Annual Meeting of International Society for Ceramics in Medicine, Istanbul, Turkey, November 6.–9., 2011. *Best Student Podium Award (presented by Acta Biomaterialia).*

9. <u>L. Pluduma</u>, K.A. Gross, L. Bērziņa-Cimdiņa. The Effects of Heating Atmosphere on the Stability of HAp. 52nd International Scientific Conference of Riga Technical University, Material Science and Applied Chemistry, Latvia, Riga, October 13.–15., 2011.

REFERENCES

[1] OECD/EU. Health at a Glance: Europe 2016 – State of Health in the EU Cycle. OECD Publishing, Paris2016. p. 200.

[2] Eurostat EC. Surgical operations and procedures statistics. http://eceuropaeu/eurostat/statistics-explained/indexphp/Surgical_operations_and_procedures_statistics (webpage viewed on 18.04.2017.).

[3] Bourlioufas N. Orthopaedic joint replacement surgery rates jump in developed nation as populations age. http://wwwasosorgau/orthopedic-surgery-rates-jump-in-developed-nation-as-populations-agehtml (webpage viewed on 18.04.2017.).

[4] Victoria G, Petrisor B, Drew B, Dick D. Bone stimulation for fracture healing: What′s all the fuss? Indian Journal of Orthopaedics 2009;43:117-20.

[5] Elliott JC. Structure and chemistry of the apatites and other calcium orthophosphates. Elsevier Inc, Amsterdam 1994:387.

[6] Emara KM, Diab RA, Emara AK. Recent biological trends in management of fracture non-union. World Journal of Orthopaedics 2015;6:623-8.

[7] Olszta MJ, Cheng X, Jee SS, Kumar R, Kim Y-Y, Kaufman MJ, et al. Bone structure and formation: A new perspective. Materials Science & Engineering R-Reports 2007;58:77-116.

[8] Nudelman F, Pieterse K, George A, Bomans PHH, Friedrich H, Brylka LJ, et al. The role of collagen in bone apatite formation in the presence of hydroxyapatite nucleation inhibitors. Nat Mater 2010;9:1004-9.

[9] Heimann RB. Thermal spraying of biomaterials. Surface & Coatings Technology 2006;201:2012-9.

[10] Baxter FR, Bowen CR, Turner IG, Dent ACE. Electrically active bioceramics: A review of interfacial responses. Annals of Biomedical Engineering 2010;38:2079-92.

[11] Khan WS, Rayan F, Dhinsa BS, Marsh D. An osteoconductive, osteoinductive, and osteogenic tissue-engineered product for trauma and orthopaedic surgery: How far are we? Stem Cells International 2012.

[12] Robling AG, Castillo AB, Turner CH. Biomechanical and molecular regulation of bone remodeling. Annual Review of Biomedical Engineering2006. p. 455-98.

[13] General Introduction to Bone: Collagen and Mineral. http://wwwiupuiedu/~bbml/boneintroshtml (webpage viewed on 13.04.2017.).

[14] Weiner S, Wagner HD. The material bone: Structure-mechanical function relations. Annual Review of Materials Science 1998;28:271-98.

[15] Kini U, Nandeesh BN. Physiology of bone formation, remodeling, and metabolism. Radionuclide and Hybrid Bone Imaging2012. p. 29-57.

[16] Pasteris JD, Wopenka B, Freeman JJ, Rogers K, Valsami-Jones E, van der Houwen JAM, et al. Lack of OH in nanocrystalline apatite as a function of degree of atomic order: implications for bone and biomaterials. Biomaterials 2004;25:229-38.

[17] Introduction to bone biology: All about our bones. https://wwwiofbonehealthorg/introduction-bone-biology-all-about-our-bones (webpage viewed on 13.04.2017.).

[18] LeGeros RZ. Properties of osteoconductive biomaterials: Calcium phosphates. Clinical Orthopaedics and Related Research 2002:81-98.

[19] Dorozhkin SV. Calcium Orthophosphates in Nature, Biology and Medicine. Materials 2009;2:399-498.

[20] Calcium Phosphate Biomaterials - Solubility of Calcium Phosphates. http://wwwazomcom/articleaspx?ArticleID=2140 (webpaged viewed on 13.04.2017.).

[21] A.M. El Kady KRM, G.T. El Bassyouni. Fabrication, characterization and bioactivity evaluation of calcium pyrophosphate/polymeric biocomposites. Ceram Int 2009.

[22] Dorozhkin SV. Calcium Orthophosphate Cements and Concretes. Materials 2009;2:221-91.

[23] Song J, Liu Y, Zhang Y, Jiao L. Mechanical properties of hydroxyapatite ceramics sintered from powders with different morphologies. Materials Science and Engineering: A 2011;528:5421-7.

[24] Nasser A.M. Barakat MSK, A.M. Omran, F.A. Sheikh, H.Y. Kim. Extraction of pure natural hydroxyapatite from the bovine bones biowaste by three different methods. J Mater Process Technol 2008.

[25] Yoshimura M. SH. Hydrothermal processing of hydroxyapatite: past, present and future. Hydroxyapatite and related materials: CRC Press; 1994. p. 45-72.

[26] D. S. Introduction to biomaterials: World Scientific Publishing; 2006.

[27] Zhuang Z, Aizawa M. Protein adsorption on single-crystal hydroxyapatite particles with preferred orientation to a(b)- and c-axes. Journal of Materials Science-Materials in Medicine 2013;24:1211-6.

[28] Yamashita K, Kitagaki K, Umegaki T. Thermal Instability and Proton Conductivity of Ceramic Hydroxyapatite at High Temperatures. Journal of the American Ceramic Society 1995;78:1191-7.

[29] Jena H, Rao CV, Eddy FP, Dooley J, Rambabu B. Structural and proton transport studies on nanocrystalline [Ca 10(PO 4) 6(OH) 2] (HAp), HAp-Nafion reg; composite, and natural human bone. Physica Status Solidi (A) Applications and Materials Science 2009;206:2536-41.

[30] Yoder C, Pasteris J, Worcester K, Schermerhorn D, Sternlieb M, Goldenberg J, et al. Dehydration and Rehydration of Carbonated Fluor- and Hydroxylapatite. Minerals 2012;2:100-17.

[31] B.D.Ratner ASH, F.J.Schoen, J.E.Lemons. Biomaterials Science: An Introduction to Materials in Medicine. Elsevier Inc, Amsterdam 2004:162-6.

[32] J. Park RSL. Biomaterials. An Introduction. Springer Science + Business Media, LLC 2007:152-4.

[33] Yoder CH, Pasteris JD, Worcester KN, Schermerhorn DV. Structural Water in Carbonated Hydroxylapatite and Fluorapatite: Confirmation by Solid State H-2 NMR. Calcified Tissue International 2012;90:60-7.

[34] Pajchel L, Kolodziejski W. Solid-state MAS NMR, TEM, and TGA studies of structural hydroxyl groups and water in nanocrystalline apatites prepared by dry milling. Journal of Nanoparticle Research 2013;15.

[35] J.M. Hughes JR. The crystal structure of apatite. Reviews in mineralogy & geochemistry 2002;48:1-12.

[36] Espanol M, Portillo J, Manero J-M, Ginebra M-P. Investigation of the hydroxyapatite obtained as hydrolysis product of alpha-tricalcium phosphate by transmission electron microscopy. Crystengcomm 2010;12:3318-26.

[37] Henning PA, Landa-Canovas AR, Larsson AK, Lidin S. Elucidation of the crystal structure of oxyapatite by high-resolution electron microscopy. Acta Crystallographica, Section B (Structural Science) 1999;B55:170-6.

[38] Kumar D, Gittings JP, Turner IG, Bowen CR, Bastida-Hidalgo A, Cartmell SH. Polarization of hydroxyapatite: Influence on osteoblast cell proliferation. Acta Biomaterialia 2010;6:1549-54.

[39] L. Calderin MJS. Electronic and crystallographic structure of apatites. Physical review B 2003;67:1-7.

[40] Corno M, Busco C, Civalleri B, Ugliengo P. Periodic ab initio study of structural and vibrational features of hexagonal hydroxyapatite Ca-10(PO4)(6)(OH)(2). Phys Chem Chem Phys 2006;8:2464-72.

[41] Gross KA, Berndt CC, Stephens P, Dinnebier R. Oxyapatite in hydroxyapatite coatings. Journal of Materials Science 1998;33:3985-91.

[42] Yang C-W, Lui T-S. Kinetics of hydrothermal crystallization under saturated steam pressure and the self-healing effect by nanocrystallite for hydroxyapatite coatings. Acta Biomaterialia 2009;5:2728-37.

[43] Tonsuaadu K, Gross KA, Pluduma L, Veiderma M. A review on the thermal stability of calcium apatites. Journal of Thermal Analysis and Calorimetry 2012;110:647-59.

[44] Schlosser M, Kleebe H-J. Vapor Transport Sintering of Porous Calcium Phosphate Ceramics. Journal of the American Ceramic Society 2012;95:1581-7.

[45] Saber-Samandari S, Alamara K, Saber-Samandari S, Gross KA. Micro-Raman spectroscopy shows how the coating process affects the characteristics of hydroxylapatite. Acta Biomaterialia 2013;9:9538-46.

[46] Antonakos A, Liarokapis E, Leventouri T. Micro-Raman and FTIR studies of synthetic and natural apatites. Biomaterials 2007;28:3043-54.

[47] LeGeros RZ. Calcium phosphates in demineralization/remineralization processes. Journal of Clinical Dentistry 1999;10:65-73.

[48] Fleet ME. Infrared spectra of carbonate apatites: $v(2)$-Region bands. Biomaterials 2009;30:1473-81.

[49] Penel G, Leroy G, Rey C, Bres E. MicroRaman spectral study of the PO4 and CO3 vibrational modes in synthetic and biological apatites. Calcified Tissue International 1998;63:475-81.

[50] Eichert D, Combes C, Drouet C, Rey C. Formation and evolution of hydrated surface layers of apatites. In: Li P, Zhang K, Colwell CW, editors. Bioceramics, Vol 17. Zurich-Uetikon: Trans Tech Publications Ltd; 2005. p. 3-6.

[51] Rey C, Combes C, Drouet C, Cazalbou S, Grossin D, Brouillet F, et al. Surface properties of biomimetic nanocrystalline apatites; applications in biomaterials. Progress in Crystal Growth and Characterization of Materials 2014;60:63-73.

[52] Rey C, Miquel JL, Facchini L, Legrand AP, Glimcher MJ. HYDROXYL-GROUPS IN BONE-MINERAL. Bone 1995;16:583-6.

[53] Wang T, Dorner-Reisel A, Müller E. Thermogravimetric and thermokinetic investigation of the dehydroxylation of a hydroxyapatite powder. Journal of the European Ceramic Society 2004;24:693-8.

[54] Liao CJ, Lin FH, Chen KS, Sun JS. Thermal decomposition and reconstitution of hydroxyapatite in air atmosphere. Biomaterials 1999;20:1807-13.

[55] 13779-3:2008(E) IsI. Implants for surgery - Hydroxyapatite. Part 3: Chemical analysis and characterization of crystallinity and phase purity. 2008.

[56] White AA, Kinloch IA, Windle AH, Best SM. Optimization of the sintering atmosphere for high-density hydroxyapatite-carbon nanotube composites. Journal of the Royal Society Interface 2010;7:S529-S39.

[57] Pluduma L. Influence of thermal processing on the structure of hydroxyapatite. Riga: Riga Technical University; 2011.

[58] Park HC, Baek DJ, Park YM, Yoon SY, Stevens R. Thermal stability of hydroxyapatite whiskers derived from the hydrolysis of α-TCP. Journal of Materials Science 2004;39:2531-4.

[59] Cihlář J, Buchal A, Trunec M. Kinetics of thermal decomposition of hydroxyapatite bioceramics. Journal of Materials Science 1999;34:6121-31.

[60] de Leeuw NH, Bowe JR, Rabone JAL. A computational investigation of stoichiometric and calcium-deficient oxy- and hydroxy-apatites. Faraday Discussions 2007;134:195-214.

[61] Gross K.A. PL. Putting oxyhydroxyapatite into perspective: A pathway to oxyapatite and its applications. In: Heimann RB, editor. Calcium Phosphates: Structure, Synthesis, Properties, and Applications: Nova Science Publishers; 2012. p. 95-120.

[62] Markovic M, Fowler BO, Tung MS. Preparation and comprehensive characterization of a calcium hydroxyapatite reference material. Journal of Research of the National Institute of Standards and Technology 2004;109:553-68.

[63] Bonte E, Deschamps N, Goldberg M, Vernois V. QUANTIFICATION OF FREE-WATER IN HUMAN DENTAL ENAMEL. Journal of Dental Research 1988;67:880-2.

[64] Rey C, Combes C, Drouet C, Glimcher MJ. Bone mineral: Update on chemical composition and structure. Osteoporosis International 2009;20:1013-21.

[65] Wang T, Dorner-Reisel A, Muller E. Thermogravimetric and thermokinetic investigation of the dehyroxylation of a hydroxyapatite powder. J Eur Ceram Soc 2004;24:693-98.

[66] Henning PA, Adolfsson E, Grins J, Fitch A. Triclinic oxy-hydroxyapatite. J Mater Sci 2001;36:663-68.

[67] Raynaud S, Champion E, Bernache-Assollant D, Thomas P. Calcium phosphate apatites with variable Ca/P atomic ratio I. Synthesis, characterisation and thermal stability of powders. Biomaterials 2002;23:1065-72.

[68] Elliott JC. Structure and chemistry of the apatites and other calcium orthophosphates. Amsterdam: Elsevier Inc.; 1994. p. 387.

[69] García-Tuñón E, Franco J, Dacuña B, Zaragoza G, Guitián F. Chlorapatite conversion to hydroxyapatite under high temperature hydrothermal conditions. Materials Science Forum2010. p. 9-14.

[70] Krajewski A, Mazzocchi M, Buldini PL, Ravaglioli A, Tinti A, Taddei P, et al. Synthesis of carbonated hydroxyapatites: Efficiency of the substitution and critical evaluation of analytical methods. Journal of molecular structure 2005;744-747:221-8.

[71] Tadic D, Epple M. A thorough physicochemical characterisation of 14 calcium phosphate-based bone substitution materials in comparison to natural bone. Biomaterials 2004;25:987-94.

[72] Legeros RZ, Bonel G, Legros R. TYPES OF H2O IN HUMAN ENAMEL AND IN PRECIPITATED APATITES. Calcified Tissue Research 1978;26:111-8.

[73] Mason HE, McCubbin FM, Smirnov A, Phillips BL. Solid-state NMR and IR spectroscopic investigation of the role of structural water and F in carbonate-rich fluorapatite. American Mineralogist 2009;94:507-16.

[74] Kaflak A, Kolodziejski W. Complementary information on water and hydroxyl groups in nanocrystalline carbonated hydroxyapatites from TGA, NMR and IR measurements. Journal of Molecular Structure 2011;990:263-70.

[75] Mkukuma LD, Imrie CT, Skakle JMS, Hukins DWL, Aspden RM. Thermal stability and structure of cancellous bone mineral from the femoral head of patients with osteoarthritis or osteoporosis. Annals of the Rheumatic Diseases 2005;64:222-5.

[76] Zyman ZZ, Rokhmistrov DV, Glushko VI, Ivanov IG. Thermal impurity reactions and structural changes in slightly carbonated hydroxyapatite. Journal of materials science: Materials in Medicine 2009;20:1389-99.

[77] H. Fujimori HT, K. Ioku, S. Goto, M. Yoshimura. In situ observation of defects in hydroxyapatite up to 1200C by ultraviolet Raman spectroscopy. Chemical Physics Letters 2000;325:382-8.

[78] Gross KA, Berndt CC, Stephens P, Dinnebier R. Oxyapatite in hydroxyapatite coatings. J Mater Sci 1998;33:3985-91.

[79] Kolmas J, Kolodziejski W. Concentration of hydroxyl groups in dental apatites: a solid-state H-1 MAS NMR study using inverse P-31 -> H-1 cross-polarization. Chemical Communications 2007:4390-2.

[80] Cho GY, Wu YT, Ackerman JL. Detection of hydroxyl ions in bone mineral by solid-state NMR spectroscopy. Science 2003;300:1123-7.

[81] Hartmann P, Jager C, Barth S, Vogel J, Meyer K. Solid state NMR, X-ray diffraction, and infrared characterization of local structure in heat-treated oxyhydroxyapatite microcrystals: An analog of the thermal decomposition of hydroxyapatite during plasma-spray procedure. Journal of Solid State Chemistry 2001;160:460-8.

[82] R. McPherson NG, T.J. Bastow. Structural characterization of plasma-sprayed hydroxylapatite coatings. Journal of materials science: Materials in Medicine 1995;6:327-34.

[83] Wilson EE, Awonusi A, Morris MD, Kohn DH, Tecklenburg MMJ, Beck LW. Three structural roles for water in bone observed by solid-state NMR. Biophysical Journal 2006;90:3722-31.

[84] Lin SY, Li MJ, Cheng WT. FT-IR and Raman vibrational microspectroscopies used for spectral biodiagnosis of human tissues. Spectroscopy-an International Journal 2007;21:1-30.

[85] Smith BC. Fundamentals of Fourier transform infrared spectroscopy: CRC Press; 2011.

[86] Rapacz-Kmita A, Paluszkiewicz C, Slosarczyk A, Paszkiewicz Z. FTIR and XRD investigations on the thermal stability of hydroxyapatite during hot pressing and pressureless sintering processes. Journal of Molecular Structure 2005;744:653-6.

[87] Cazalbou S, Bertrand G, Drouet C. Tetracycline-loaded biomimetic apatite: An adsorption study. Journal of Physical Chemistry B 2015;119:3014-24.

[88] Demnati I, Grossin D, Marsan O, Bertrand G, Collonges G, Combes C, et al. Comparison of physical-chemical and mechanical properties of chlorapatite and hydroxyapatite plasma sprayed coatings. Open Biomedical Engineering Journal 2015;9:42-55.

[89] Dasarathy H, Riley C, Coble HD. Analysis of apatite deposits on substrates. Journal of Biomedical Materials Research 1993;27:477-82.

[90] Eichert D, Drouet C, Sfihi H, Rey C, Combes C. Nanocrystalline apatite-based biomaterials: Synthesis, processing and characterization. Nanotechnology Research Progress2009. p. 143-92.

[91] Ranz X. Developpement et caracterisation de depots d'apatite obtenus par projection plasma sur protheses orthopediques. PhD thesis Institut National Polytechnique, Toulouse, France 1996.

[92] J.C.Trombe. Contribution a l'etude de la decomposition et de la reactivite de certaines apatites hydroxylees et carbonatees. Annales des Chimie 1973;8:251-69.

[93] Demnati I, Parco M, Grossin D, Fagoaga I, Drouet C, Barykin G, et al. Hydroxyapatite coating on titanium by a low energy plasma spraying mini-gun. Surface and Coatings Technology 2012;206:2346-53.

[94] Peeran M. Comparison of Raman and IR Spectroscopy. http://wwwchemvistaorg/ramanIR4html (webpage viewed on 15.04.2017).

[95] Choo-Smith LP, Maquelin K, Van Vreeswijk T, Bruining HA, Puppels GJ, Ngo Thi NA, et al. Investigating Microbial (Micro)colony Heterogeneity by Vibrational Spectroscopy. Applied and Environmental Microbiology 2001;67:1461-9.

[96] NIST Material Measurement Laboratory: Water. http://webbooknistgov/cgi/cbookcgi?ID=C7732185&Type=IR-SPEC&Index=1 (webpage viewed on 15.04.2017).

[97] Henning PA, Landa-Canovas AR, Larsson AK, Lidin S. Elucidation of the crystal structure of oxyapatite by high-resolution electron microscopy. Acta Cryst 1999;B55:170-76.

[98] McCubbin FM, Nekvasil H. Maskelynite-hosted apatite in the Chassigny meteorite: Insights into late-stage magmatic volatile evolution in martian magmas. American Mineralogist 2008;93:676-84.

[99] Boyce JW, Liu Y, Rossman GR, Guan Y, Eiler JM, Stolper EM, et al. Lunar apatite with terrestrial volatile abundances. Nature 2010;466:466-U2.

[100] Wang KL, Zhang Y, Naab FU. Calibration for IR measurements of OH in apatite. American Mineralogist 2011;96:1392-7.

[101] Surmenev RA, Surmeneva MA, Ivanova AA. Significance of calcium phosphate coatings for the enhancement of new bone osteogenesis - A review. Acta Biomaterialia 2014;10:557-79.

[102] Sun L, Berndt CC, Gross KA, Kucuk A. Material fundamentals and clinical performance of plasma-sprayed hydroxyapatite coatings: A review. Journal of Biomedical Materials Research 2001;58:570-92.

[103] Gross KA, Saber-Samandari S, Heemann KS. Evaluation of commercial implants with nanoindentation defines future development needs for hydroxyapatite coatings. Journal of Biomedical Materials Research - Part B Applied Biomaterials 2010;93:1-8.

[104] Shepperd JAN, Apthorp H. A contemporary snapshot of the use of hydroxyapatite coating in orthopaedic surgery. Journal of Bone and Joint Surgery - Series B 2005;87:1046-9.

[105] Gadow R, Killinger A, Stiegler N. Hydroxyapatite coatings for biomedical applications deposited by different thermal spray techniques. Surface and Coatings Technology 2010;205:1157-64.

[106] Lynn AK, DuQuesnay DL. Hydroxyapatite-coated Ti-6Al-4V: Part 1: The effect of coating thickness on mechanical fatigue behaviour. Biomaterials 2002;23:1937-46.

[107] Cao Y, Weng J, Chen JY, Feng JM, Yang ZJ, Zhang XD. Water vapour-treated hydroxyapatite coatings after plasma spraying and their characteristics. Biomaterials 1996;17:419-24.

[108] Ellies LG, Nelson DGA, Featherstone JDB. CRYSTALLOGRAPHIC CHANGES IN CALCIUM PHOSPHATES DURING PLASMA-SPRAYING. Biomaterials 1992;13:313-6.

[109] Lin FH, Liao CJ, Chen KS, Sun JS. Thermal reconstruction behavior of the quenched hydroxyapatite powder during reheating in air. Materials Science & Engineering C-Biomimetic and Supramolecular Systems 2000;13:97-104.

[110] Wang BC, Chang E, Yang CY. CHARACTERIZATION OF PLASMA-SPRAYED BIOACTIVE HYDROXYAPATITE COATINGS IN-VITRO AND IN-VIVO. Materials Chemistry and Physics 1994;37:55-63.

[111] Zhuang Z, Fujimi TJ, Nakamura M, Konishi T, Yoshimura H, Aizawa M. Development of a,b-plane-oriented hydroxyapatite ceramics as models for living bones and their cell adhesion behavior. Acta Biomaterialia 2013;9:6732-40.

[112] Kim H, Camata RP, Chowdhury S, Vohra YK. In vitro dissolution and mechanical behavior of c-axis preferentially oriented hydroxyapatite thin films fabricated by pulsed laser deposition. Acta Biomaterialia 2010;6:3234-41.

[113] Kim H, Camata RP, Lee S, Rohrer GS, Rollett AD, Vohra YK. Crystallographic texture in pulsed laser deposited hydroxyapatite bioceramic coatings. Acta Materialia 2007;55:131-9.

[114] Manso M, Herrero P, Fernandez M, Langlet M, Martinez-Duart JM. Textured hydroxyapatite interface onto biomedical titanium-based coatings. Journal of Biomedical Materials Research Part A 2003;64A:600-5.

[115] Filgueiras MRT, Mkhonto D, de Leeuw NH. Computer simulations of the adsorption of citric acid at hydroxyapatite surfaces. Journal of Crystal Growth 2006;294:60-8.

[116] de Leeuw NH, Rabone JAL. Molecular dynamics simulations of the interaction of citric acid with the hydroxyapatite (0001) and (01(1)over-bar0) surfaces in an aqueous environment. Crystengcomm 2007;9:1178-86.

[117] Dong X-L, Zhou H-L, Wu T, Wang Q. Behavior regulation of adsorbed proteins via hydroxyapatite surface texture control. Journal of Physical Chemistry B 2008;112:4751-9.

[118] Gross KA, Muller D, Lucas H, Haynes DR. Osteoclast resorption of thermal spray hydoxyapatite coatings is influenced by surface topography. Acta Biomaterialia 2012;8:1948-56.

[119] Dinda GP, Shin J, Mazumder J. Pulsed laser deposition of hydroxyapatite thin films on Ti-6Al-4V: Effect of heat treatment on structure and properties. Acta Biomaterialia 2009;5:1821-30.

[120] Sato K, Kogure T, Kumagai Y, Tanaka J. Crystal orientation of hydroxyapatite induced by ordered carboxyl groups. Journal of Colloid and Interface Science 2001;240:133-8.

[121] Zhang W, Chai Y, Xu X, Wang Y, Cao N. Rod-shaped hydroxyapatite with mesoporous structure as drug carriers for proteins. Applied Surface Science 2014;322:71-7.

[122] Ashok M, Kalkura SN, Sundaram NM, Arivuoli D. Growth and characterization of hydroxyapatite crystals by hydrothermal method. Journal of Materials Science-Materials in Medicine 2007;18:895-8.

[123] Chen W, Long T, Guo YJ, Zhu ZA, Guo YP. Hydrothermal synthesis of hydroxyapatite coatings with oriented nanorod arrays. RSC Adv 2014;4:185-91.

[124] Ban S, Hasegawa J. Morphological regulation and crystal growth of hydrothermal-electrochemically deposited apatite. Biomaterials 2002;23:2965-72.

[125] Inagaki M, Kameyama T. Phase transformation of plasma-sprayed hydroxyapatite coating with preferred crystalline orientation. Biomaterials 2007;28:2923-31.

[126] Xixue H, Hong S, Yan C, Xiaoling X, Shenguo W, Jing F, et al. One-step modification of nano-hydroxyapatite coating on titanium surface by hydrothermal method. Surface & Coatings Technology 2010;205:2000-6.

[127] Chung-Wei Y, Truan-Sheng L. Kinetics of hydrothermal crystallization under saturated steam pressure and the self-healing effect by nanocrystallite for hydroxyapatite coatings. Acta Biomaterialia 2009;5:2728-37.

[128] Yang CY, Lee TM, Yang CW, Chen LR, Wu MC, Lui TS. In vitro and in vivo biological responses of plasma-sprayed hydroxyapatite coatings with posthydrothermal treatment. Journal of Biomedical Materials Research Part A 2007;83A:263-71.

[129] Han Y, Xu KW, Lu JA. Morphology and composition of hydroxyapatite coatings prepared by hydrothermal treatment on electrodeposited brushite coatings. Journal of Materials Science-Materials in Medicine 1999;10:243-8.

[130] Weng J, Liu X, Zhang X, Ma Z, Ji X, Zyman Z. FURTHER-STUDIES ON THE PLASMA-SPRAYED AMORPHOUS PHASE IN HYDROXYAPATITE COATINGS AND ITS DEAMORPHIZATION. Biomaterials 1993;14:578-82.

[131] Tofail SAM, Gandhi AA, Gregor M, Bauer J. Electrical properties of hydroxyapatite. Pure and Applied Chemistry 2015;87:221-9.

[132] Kohata K, Itoh S, Horiuchi N, Yoshioka T, Yamashita K. Influences of osteoarthritis and osteoporosis on the electrical properties of human bones as in vivo electrets produced due to Wolff's law. Bio-Medical Materials and Engineering 2017;28:65-74.

[133] Yamashita K, Oikawa N, Umegaki T. Acceleration and deceleration of bone-like crystal growth on ceramic hydroxyapatite by electric poling. Chemistry of Materials 1996;8:2697-&.

[134] Arends J, Royce BSH, Siegel J, Smoluchowski R. Dielectric relaxation in hydroxy apatite. Physics Letters A 1968;27:720-1.

[135] Hitmi N, Lacabanne C, Young RA. OH- DIPOLE REORIENTABILITY IN HYDROXYAPATITES - EFFECT OF TUNNEL SIZE. Journal of Physics and Chemistry of Solids 1986;47:533-46.

[136] Nakamura S, Takeda H, Yamashita K. Proton transport polarization and depolarization of hydroxyapatite ceramics. Journal of Applied Physics 2001;89:5386-92.

[137] Gittings JP, Bowen CR, Dent ACE, Turner IG, Baxter FR, Cartmell S, et al. Influence of Porosity on Polarisation and Electrical Properties of Hydroxyapatite Based Ceramics. Ferroelectrics 2009;390:168-76.

[138] Gittings JP, Bowen CR, Dent ACE, Turner IG, Baxter FR, Chaudhuri JB. Electrical characterization of hydroxyapatite-based bioceramics. Acta Biomaterialia 2009;5:743-54.

[139] Harding IS, Rashid N, Hing KA. Surface charge and the effect of excess calcium ions on the hydroxyapatite surface. Biomaterials 2005;26:6818-26.

[140] Truchly M, Plecenik T, Secianska K, Gregor M, Zahoran M, Vargova M, et al. Surface potential patterning of hydroxyapatite films by focused electron beam: Influence of the electron energy. Applied Surface Science 2013;269:184-7.

[141] Aronov D, Rosen R, Ron EZ, Rosenman G. Tunable hydroxyapatite wettability: Effect on adhesion of biological molecules. Process Biochemistry 2006;41:2367-72.

[142] Tan F, O'Neill F, Naciri M, Dowling D, Al-Rubeai M. Cellular and transcriptomic analysis of human mesenchymal stem cell response to plasma-activated hydroxyapatite coating. Acta Biomaterialia 2012;8:1627-38.

[143] Yeung WK, Reilly GC, Matthews A, Yerokhin A. In vitro biological response of plasma electrolytically oxidized and plasma-sprayed hydroxyapatite coatings on Ti-6Al-4V alloy. Journal of Biomedical Materials Research - Part B Applied Biomaterials 2013;101 B:939-49.

[144] Mwale F, Wang HT, Nelea V, Luo L, Antoniou J, Wertheimer MR. The effect of glow discharge plasma surface modification of polymers on the osteogenic differentiation of committed human mesenchymal stem cells. Biomaterials 2006;27:2258-64.

[145] Huang Y, Qu Y, Yang B, Li W, Zhang B, Zhang X. In vivo biological responses of plasma sprayed hydroxyapatite coatings with an electric polarized treatment in alkaline solution. Materials Science and Engineering C 2009;29:2411-6.

[146] Lee WH, Loo CY, Van KL, Zavgorodniy AV, Rohanizadeh R. Modulating protein adsorption onto hydroxyapatite particles using different amino acid treatments. Journal of the Royal Society Interface 2012;9:918-27.

[147] Nakamura M, Kobayashi A, Nozaki K, Horiuchi N, Nagai A, Yamashita K. Improvement of Osteoblast Adhesion Through Polarization of Plasma-Sprayed Hydroxyapatite Coatings on Metal. Journal of Medical and Biological Engineering 2014;34:44-8.

[148] Nakamura S, Kobayashi T, Yamashita K. Extended bioactivity in the proximity of hydroxyapatite ceramic surfaces induced by polarization charges. Journal of Biomedical Materials Research 2002;61:593-9.

[149] Bodhak S, Bose S, Bandyopadhyay A. Role of surface charge and wettability on early stage mineralization and bone cell-materials interactions of polarized hydroxyapatite. Acta Biomaterialia 2009;5:2178-88.

[150] Bodhak S, Bose S, Bandyopadhyay A. Electrically polarized HAp-coated Ti: In vitro bone cell-material interactions. Acta Biomaterialia 2010;6:641-51.

[151] Iwasaki T, Tanaka Y, Nakamura M, Nagai A, Hashimoto K, Toda Y, et al. Rate of bonelike apatite formation accelerated on polarized porous hydroxyapatite. Journal of the American Ceramic Society 2008;91:3943-9.

[152] Cartmell SH, Thurstan S, Gittings JP, Griffiths S, Bowen CR, Turner IG. Polarization of porous hydroxyapatite scaffolds: Influence on osteoblast cell proliferation and extracellular matrix production. Journal of Biomedical Materials Research Part A 2014;102:1047-52.

[153] Nagai A, Tanaka K, Tanaka Y, Nakamura M, Hashimoto K, Yamashita K. Electric polarization and mechanism of B-type carbonated apatite ceramics. Journal of Biomedical Materials Research - Part A 2011;99 A:116-24.

[154] Takeda H, Seki Y, Nakamura S, Yamashita K. Evaluation of electrical polarizability and in vitro bioactivity of apatite Sr5(PO4)3OH dense ceramics. Journal of Materials Chemistry 2002;12:2490-5.

[155] Tarafder S, Banerjee S, Bandyopadhyay A, Bose S. Electrically polarized biphasic calcium phosphates: Adsorption and release of bovine serum albumin. Langmuir 2010;26:16625-9.

[156] Itoh S, Nakamura S, Kobayashi T, Shinomiya K, Yamashita K, Itoh S. Effect of electrical polarization of hydroxyapatite ceramics on new bone formation. Calcified Tissue International 2006;78:133-42.

[157] Zreiqat H, Akin FA, Howlett CR, Markovic B, Haynes D, Lateef S, et al. Differentiation of human bone-derived cells grown on GRGDSP-peptide bound titanium surfaces. Journal of Biomedical Materials Research Part A 2003;64A:105-13.

[158] Zhang BGX, Myers DE, Wallace GG, Brandt M, Choong PFM. Bioactive Coatings for Orthopaedic Implants-Recent Trends in Development of Implant Coatings. International Journal of Molecular Sciences 2014;15:11878-921.

[159] Yi H, Yang Q, Bangcheng Y, Wei L, Bo Z, Xingdong Z. In vivo biological responses of plasma sprayed hydroxyapatite coatings with an electric polarized treatment in alkaline solution. Materials Science & Engineering: C (Materials for Biological Applications) 2009;29:2411-16.

[160] Ohgaki M, Kizuki T, Katsura M, Yamashita K. Manipulation of selective cell adhesion and growth by surface charges of electrically polarized hydroxyapatite. Journal of Biomedical Materials Research 2001;57:366-73.

[161] Kato R, Nakamura S, Katayama K, Yamashita K. Electrical polarization of plasma-spray-hydroxyapatite coatings for improvement of osteoconduction of implants. Journal of Biomedical Materials Research Part A 2005;74A:652-8.

[162] Nakamura S, Kobayashi T, Yamashita K. Numerical osteobonding evaluation of electrically polarized hydroxyapatite ceramics. Journal of Biomedical Materials Research Part A 2004;68A:90-4.

[163] Redey SA, Nardin M, Bernache-Assolant D, Rey C, Delannoy P, Sedel L, et al. Behavior of human osteoblastic cells on stoichiometric hydroxyapatite and type A carbonate apatite: Role of surface energy. Journal of Biomedical Materials Research 2000;50:353-64.

[164] Thian ES, Ahmad Z, Huang J, Edirisinghe MJ, Jayasinghe SN, Ireland DC, et al. The role of surface wettability and surface charge of electrosprayed nanoapatites on the behaviour of osteoblasts. Acta Biomaterialia 2010;6:750-5.

[165] Wanlei Y, Weiqi H, Wei H, Jianlei L, Jirong W, Haotian F, et al. Surface topography of hydroxyapatite promotes osteogenic differentiation of human bone marrow mesenchymal stem cells. Materials Science and Engineering: C (Materials for Biological Applications) 2016;60:45-53.

[166] Costa-Rodrigues J, Fernandes A, Lopes MA, Fernandes MH. Hydroxyapatite surface roughness: Complex modulation of the osteoclastogenesis of human precursor cells. Acta Biomaterialia 2012;8:1137-45.

[167] Ripamonti U, Roden LC, Renton LF. Osteoinductive hydroxyapatite-coated titanium implants. Biomaterials 2012;33:3813-23.

[168] Freimanis E. Hydroxyapatite surface electric potential dependence on surface roughness properties: Riga Technical University; 2016.

[169] del Valle LJ, Bertran O, Chaves G, Revilla-Lopez G, Rivas M, Casas MT, et al. DNA adsorbed on hydroxyapatite surfaces. Journal of Materials Chemistry B 2014;2:6953-66.

[170] Nagai A, Yamashita K, Imamura M, Azuma H. Hydroxyapatite electret accelerates reendothelialization and attenuates intimal hyperplasia occurring after endothelial removal of the rabbit carotid artery. Life Sciences 2008;82:1162-8.

[171] Okabayashi R, Nakamura M, Okabayashi T, Tanaka Y, Nagai A, Yamashita K. Efficacy of Polarized Hydroxyapatite and Silk Fibroin Composite Dressing Gel on Epidermal Recovery From Full-Thickness Skin Wounds. Journal of Biomedical Materials Research Part B-Applied Biomaterials 2009;90B:641-6.

[172] Han YC, Wang XY, Dai HL, Li SP. Nanosize and Surface Charge Effects of Hydroxyapatite Nanoparticles on Red Blood Cell Suspensions. ACS Appl Mater Interfaces 2012;4:4616-22.

[173] Del Pozo JL, Rouse MS, Mandrekar JN, Sampedro MF, Steckelberg JM, Patel R. Effect of electrical current on the activities of antimicrobial agents against Pseudomonas aeruginosa, Staphylococcus aureus, and Staphylococcus epidermidis biofilms. Antimicrobial Agents and Chemotherapy 2009;53:35-40.

[174] Sultana ST, Babauta JT, Beyenal H. Electrochemical biofilm control: A review. Biofouling 2015;31:745-58.

[175] Atkins GJ, Kostakis P, Pan BQ, Farrugia A, Gronthos S, Evdokiou A, et al. RANKL expression is related to the differentiation state of human osteoblasts. Journal of Bone and Mineral Research 2003;18:1088-98.

[176] I. Smičiklas AO, S. Raičevic. Experimental design approach in the synthesis of hydroxyapatite by neutralization method. Sep Purif Technol 2005;44:97-102.

[177] C. Kothapalli MW, A. Vasiliev, M.T. Shaw. Influence of temperature and concentration on the sintering behavior and mechanical properties of hydroxyapatite. Acta Materialia 2004;52:5655-63.

[178] Wang P, Li C, Gong H, Jiang X, Wang H, Li K. Effects of synthesis conditions on the morphology of hydroxyapatite nanoparticles produced by wet chemical process. Powder Technology 2010;203:315-21.

[179] 13779-1:2008(E) IsI. Implants for surgery - Hydroxyapatite. Part 1: Ceramic hydroxyapatite. 2008.

[180] Alberius-Henning P, Adolfsson E, Grins J, Fitch A. Triclinic oxy-hydroxyapatite. Journal of Materials Science 2001;36:663-8.

[181] Moreno E.C. K, M., Zahradnik, R.T. Fluoridated hydroxyapatite solubility and caries formation. Nature 1974;247:64-5.

[182] Negas T RRS. High temperature dehydroxylation of apatitic phosphates. Journal of Research of the National Bureau of Standards - A Physics and Chemistry 1968;72A:783-7.

[183] Rodriguez-Lorenzo LM, Hart JN, Gross KA. Influence of fluorine in the synthesis of apatites. Synthesis of solid solutions of hydroxy-fluorapatite. Biomaterials 2003;24:3777-85.

[184] Rintoul L, Wentrup-Byrne E, Suzuki S, Grøndahl L. FT-IR spectroscopy of fluoro-substituted hydroxyapatite: Strengths and limitations. Journal of materials science: Materials in Medicine 2007;18:1701-9.

[185] Wei M, Evans JH, Bostrom T, GrØndahl L. Synthesis and characterization of hydroxyapatite, fluoride-substituted hydroxyapatite and fluorapatite. Journal of materials science: Materials in Medicine 2003;14:311-20.

[186] Bianco A, Cacciotti I, Lombardi M, Montanaro L, Bemporad E, Sebastiani M. F-substituted hydroxyapatite nanopowders: Thermal stability, sintering behaviour and mechanical properties. Ceramics International 2010;36:313-22.

[187] Balan E, Delattre S, Roche D, Segalen L, Morin G, Guillaumet M, et al. Line-broadening effects in the powder infrared spectrum of apatite. Physics and Chemistry of Minerals 2011;38:111-22.

[188] Engel G, Klee WE. INFRARED-SPECTRA OF HYDROXYL IONS IN VARIOUS APATITES. Journal of Solid State Chemistry 1972;5:28-&.

[189] M. Weinlaender JBI, E.B. Kenney, P.K. Moy. Raman microprobe investigation of the calcium phosphate phases of three commercially available plasma-flame-sprayed hydroxyapatite-coated dental implants. Journal of materials science: Materials in Medicine 1992;3:397-401.

[190] Posset U, Löcklin E, Thull R, Kiefer W. Vibrational spectroscopic study of tetracalcium phosphate in pure polycrystalline form and as a constituent of a self-setting bone cement. Journal of Biomedical Materials Research 1998;40:640-5.

[191] Wang CY, Duan YR, Markovic B, Barbara J, Howlett CR, Zhang XD, et al. Proliferation and bone-related gene expression of osteoblasts grown on hydroxyapatite ceramics sintered at different temperature. Biomaterials 2004;25:2949-56.

[192] Sila-Asna M, Bunyaratvej A, Maeda S, Kitaguchi H, Bunyaratavej N. Osteoblast differentiation and bone formation gene expression in strontium-inducing bone marrow mesenchymal stem cell. The Kobe journal of medical sciences 2007;53:25-35.

[193] Crespi R, Mariani E, Benasciutti E, Cappare P, Cenci S, Gherlone E. Magnesium-Enriched Hydroxyapatite Versus Autologous Bone in Maxillary Sinus Grafting: Combining Histomorphometry With Osteoblast Gene Expression Profiles Ex Vivo. Journal of Periodontology 2009;80:586-93.

APPENDICES

Appendix 1

TGA analysis of HA, HA and CPP mixture, and HA and CaF$_2$ mixture

HA + CPP

HA + CaF$_2$
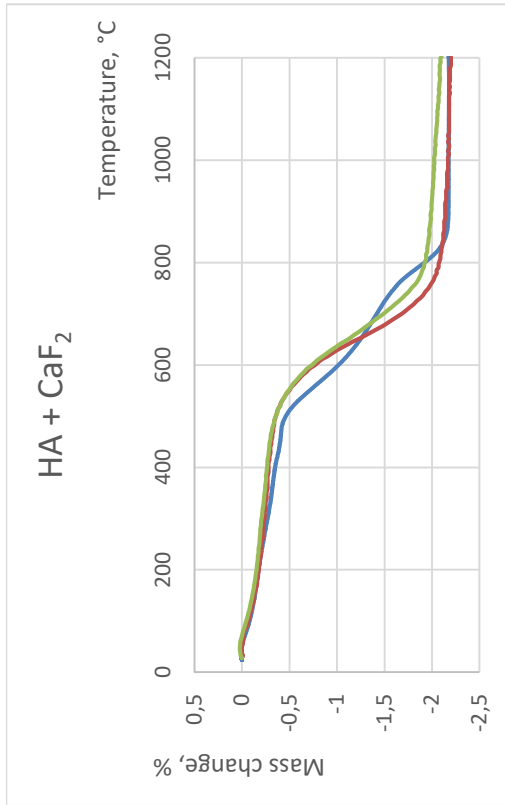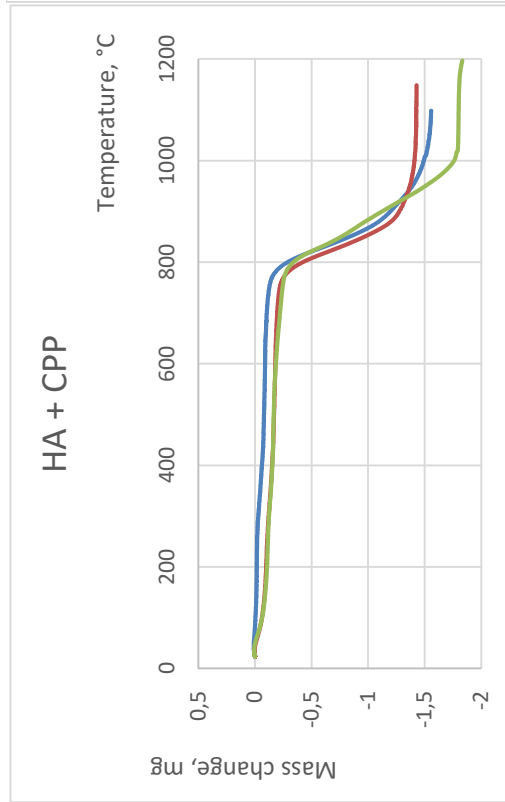
Standard HA
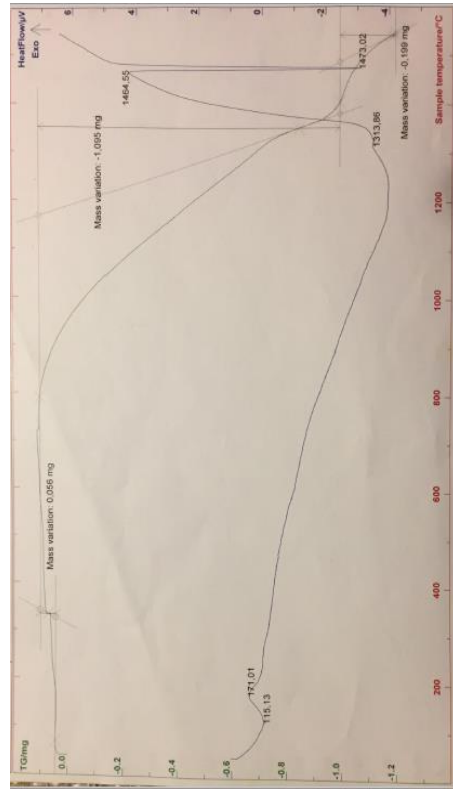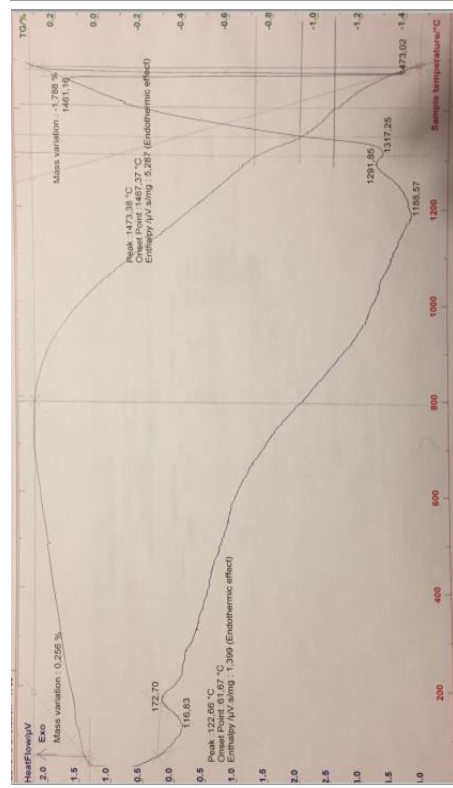
OH⁻ calculations using TGA results

Reaction type	mass HA, mg	mass reactant, mg	reactant/ HA	mass of mixture, mg	loss before r-tion, mg	start t	end t	loss after r-tion, mg	loss of reaction, mg	dry mass, mg	dry HA in mixture, mg	% loss due to OH⁻	ratio of OH⁻	% of OH⁻
HA + CPP	507,500	154	0,303	110	0,088	600	1100	1,555	1,467	110,000	84,392	1,738	0,970	96,960
	265,000	85,9	0,324	93,3	0,181	600	1150	1,427	1,246	93,119	70,324	1,772	0,988	98,828
	99,9	29,5	0,295295	108,1	0,18501	600	1050	1,7972	1,61219	107,915	83,31304	1,935099	1,079355	107,9355
	98,9	30	0,303337	98,3	0,14547	600	1050	1,56008	1,41461	98,15453	75,31019	1,878378	1,047718	104,7718
HA + CaF₂	201,000	20,200	0,100	93,300	0,345	460	1050	1,840	1,495	92,955	84,466	1,770	0,987	98,705
	100,8	11,088	0,11	75,8	0,29%	460	1050	1,99%	1,70%	74,5114	67,127	1,7	0,948	94,82221
	101,2	10,4236	0,103	83,2	0,31%	460	1050	2,21%	1,90%	81,6192	73,997	1,9	1,060	105,9778
HA					0,02%	600	1445	1,65%				1,627	0,908	90,75043
					0,26%	800	1473	1,79%				1,532	0,855	85,45154
				75,07399	0,056	800	1390	1,039	1,039	75,07399	75,074	1,384	0,772	77,195

Appendix 2

OH$^-$ and PO$_4^{3-}$ area data of HA, FA and HA/FA mechanical mixtures from deconvulated 500 – 750 cm^{-1} FTIR spectral range

HA

1		2		3	
cm(-1)	Area	cm(-1)	Area	cm(-1)	Area
668	0,3959	668	2,5516	668	0,9509
653	0,4526	653	1,3047	653	0,8528
632,6592	4,4827	633,0963	12,1696	632,6561	8,6392
604,0493	1,8439	604,758	4,3032	604,1307	3,5601
599,6405	1,4807	599,6812	3,9086	599,6961	2,7549
573,2748	3,8405	572,8685	10,0852	572,7018	7,3741
564,4375	4,8885	561,9109	15,4019	563,4997	11,2344
Sum(PO4)	12,0536	Sum(PO4)	33,6989	Sum(PO4)	24,923

OH/PO4	Average	OH%
0,371897	0,359884	100
0,361128		
0,346629		

FA

1		2		3	
cm(-1)	Area	cm(-1)	Area	cm(-1)	Area
668	0,0008	668	0,101	668	0,001
653	0,0395	653	0,294	653	0,0392
632	1,0356	632	0,4034	632	0,4252
608,6495	18,9069	608,3471	9,7913	608,3492	9,3897
600,9417	9,6269	600,9738	5,3869	601,0084	5,1677
577,5547	11,0389	577,5032	6,046	577,5275	5,7115
565,3017	31,9143	565,5698	16,674	565,6503	16,0996
Sum(PO4)	71,487	Sum(PO4)	37,8982	Sum(PO4)	36,368

OH/PO4	Average	OH%	Average
0,014487	0,012274	3,89531	3,300401
0,010644		2,862163	
0,011691		3,143728	

HA/FA_25/75

OH/PO4	Average	OH%	Average
0,11748	0,10145	31,58938	27,27912
0,08952		24,07117	
0,097351		26,17681	

corrected against FA

OH/PO4	Average	OH%	Average
0,105206	0,089176	28,28897	23,97872
0,077246		20,77077	
0,085077		22,87641	

1		2		3	
cm(-1)	Area	cm(-1)	Area	cm(-1)	Area
668	0,0028	668	0,139	668	0,098
653	0,0642	653	0,2111	653	0,0731
633,0459	4,7219	632,8451	3,531	632,9709	4,8402
607,4839	8,1074	607,2217	8,4276	607,3801	11,4616
600,9438	5,9912	601,0024	6,1218	601,0231	8,2094
577,0056	6,8306	576,8487	6,2853	576,9077	8,3631
566,4862	19,2622	566,896	18,6096	566,8139	21,6772
Sum(PO4)	40,191	Sum(PO4)	39,444	Sum(PO4)	49,711

FrAp/Fap_50/50

OH/PO4	Average	OH%	Average
0,178253	0,180288	47,93066	48,47799
0,187893		50,52283	
0,174719		46,98048	

corrected against FA

OH/PO4	Average	OH%	Average
0,165979	0,168014	44,63026	45,17759
0,175619		47,22243	
0,162445		43,68008	

1		2		3	
cm(-1)	Area	cm(-1)	Area	cm(-1)	Area
668	0,0048	668	0,1709	668	0,1128
653	0,0576	653	0,2769	653	0,0959
632,6962	4,0796	632,8805	4,6586	632,6419	2,8876
606,3299	4,2443	606,5721	4,5245	606,2196	3,0456
600,836	3,7929	600,7143	3,9012	600,7978	2,6639
575,9434	4,6158	575,8194	4,8712	575,8915	3,094
566,8008	10,2336	565,9995	11,497	566,9919	7,7236
Sum(PO4)	22,8866	Sum(PO4)	24,7939	Sum(PO4)	16,5271

	OH/PO4	Average	OH%	Average
FrAp/Fap_75/25	0,28342		76,20923	82,68876
	0,31004	0,307517	83,36713	
	0,329092		88,48993	
corrected against FA	0,271146		72,90883	79,38836
	0,297766	0,295243	80,06673	
	0,316817		85,18953	

1		2		3	
cm(-1)	Area	cm(-1)	Area	cm(-1)	Area
668	0,1932	668	0,1219	668	0,3211
653	0,449	653	0,6255	653	0,721
632,7414	6,1466	632,8439	6,2137	632,8397	7,3984
604,5596	3,261	604,7627	3,0965	604,6751	3,8135
599,9448	2,4555	599,7524	2,3245	599,8881	2,8806
573,9526	6,8914	574,1071	5,7031	573,8447	6,9863
564,8518	9,0799	563,9078	8,9235	564,0812	8,7999
Sum(PO4)	21,6878	Sum(PO4)	20,0476	Sum(PO4)	22,4803

Appendix 3

OH⁻ and PO₄³⁻ are data of additional HA/FA mixtures from deconvulated 500 - 750 cm⁻¹ spectral range
(OH⁻ amount in % is calculated from the calibration curve)

HA/FA_50/50

1 cm(-1)	1 Area	2 cm(-1)	2 Area	3 cm(-1)	3 Area	4 cm(-1)	4 Area	5 cm(-1)	5 Area	6 cm(-1)	6 Area
668	0,117	668	0,045	668	0,0032	668		668	0,0495	668	
653	0,5414	653	0,2252	653	0,3069	653	0,4836	653	0,2676	653	0,4527
632,9174	7,54375	632,7128	4,658765	632,6298	3,027955	632,6886	4,70024	632,7192	3,99985	632,735	4,49420
606,3609	7,0463	605,7667	4,1372	605,6035	2,7272	605,7175	4,2245	605,7157	3,5212	605,774	3,9513
600,8247	6,4777	600,6193	3,4338	600,6032	2,2075	600,6607	3,556	600,5264	2,8462	600,571	3,3002
575,8198	7,4856	575,1604	5,1701	574,5609	4,0092	574,6135	6,2945	574,6916	4,9585	574,579	5,8906
566,6794	19,3545	566,0142	10,6138	565,2592	6,37	565,1732	9,978	565,0006	8,6608	564,807	9,5495
Sum(PO4)	40,3641	Sum(PO4)	23,3549	Sum(PO4)	15,3139	Sum(PO4)	24,053	Sum(PO4)	19,9867	Sum(PO4)	22,6916

OH/PO4	Average	STDEV	RSD		OH%	Average	STDEV	RSD
0,186893	0,196281	0,004881	2,652705		51,24123	53,77877	1,319236	2,614344
0,199477					54,64243			
0,197726					54,16917			
0,195412					53,54379			
0,200125					54,81766			
0,198056					54,25835			
0,174618					47,92391			
0,187203					51,3251			
corrected against FA 0,185452	0,184007	0,004881	2,652705		50,85184	50,46145	1,319236	2,614344
0,183138					50,22646			
0,187851					51,50033			
0,185782					50,94102			

HA/FA_60/40

| | 1 | | 2 | | 3 |
cm(-1)	Area	cm(-1)	Area	cm(-1)	Area
668	0,041	668	0,0378	668	0,0312
653	0,3174	653	0,262	653	0,3388
632,6894	7,1698	632,544	4,8916	632,6349	7,4067
605,5116	5,0521	605,2434	3,6122	605,4397	5,217
600,4641	4,1392	600,4425	2,8423	600,4523	4,281
574,5745	7,5094	574,3197	5,6725	574,3715	8,1232
565,041	12,2165	564,9575	8,0045	564,7215	12,4198
Sum(PO4)	28,9172	Sum(PO4)	20,1315	Sum(PO4)	30,041

HA/FA_40/60

| | 1 | | 2 | | 3 |
cm(-1)	Area	cm(-1)	Area	cm(-1)	Area
668		668		668	
653		653		653	
632,6926	3,30255	632,4841	4,75731	632,5406	4,42098
606,7128	3,576	606,4214	5,2012	606,4755	5,0278
600,5139	2,7292	600,7201	4,5257	600,766	4,4516
575,7324	4,474	575,624	5,7803	575,3956	6,4374
564,5697	7,8045	565,8453	13,4977	565,2459	11,8179
Sum(PO4)	18,5837	Sum(PO4)	29,0049	Sum(PO4)	27,7347

	OH/PO4	Average	STDEV	RSD	OH%	Average	STDEV	RSD
HA/FA_40/60	0,177712				48,76005			
	0,164017	0,167044	0,009523	6,152799	45,05877	45,87677	2,573698	6,047302
	0,159402				43,81148			
corrected against FA	0,165438				45,44273			
	0,151743	0,15477	0,009523	6,152799	41,74145	42,55944	2,573698	6,047302
	0,147128				40,49416			

	OH/PO4	Average	STDEV	RSD	OH%	Average	STDEV	RSD
HA/FA_60/40	0,247942				67,74119			
	0,242982	0,245826	0,002559	1,095558	66,40065	67,16917	0,69154	1,083038
	0,246553				67,36569			
corrected against FA	0,235668				64,42387			
	0,230708	0,233552	0,002559	1,095558	63,08332	63,85185	0,69154	1,083038
	0,234279				64,04836			

HA/FA_80/20

1		2		3	
cm(-1)	Area	cm(-1)	Area	cm(-1)	Area
668	0,4704	668	0,6271	668	0,9191
653	1,1433	653	1,3068	653	1,819
632,6027	8,086	632,6909	8,4044	632,6673	11,4912
604,5335	4,2826	604,6853	4,2552	604,6479	5,8983
599,8748	2,9351	599,7622	2,924	599,8705	4,0829
572,9012	8,9901	572,8654	9,0747	572,7513	13,13
562,2496	10,0408	561,1676	10,7666	561,0875	14,0176
Sum(PO4)	26,2486	Sum(PO4)	27,0205	Sum(PO4)	37,1288

	OH/PO4	Average	STDEV	RSD
	0,308055			
	0,311038	0,309529	0,001492	0,501919
	0,309496			
corrected	0,29578			
against	0,298764	0,297255	0,001492	0,501919
FA	0,297221			

OH%	Average	STDEV	RSD
83,98771			
84,79403	84,38631	0,403238	0,497401
84,37719			
80,67039			
81,47671	81,06899	0,403238	0,497401
81,05986			

XRD patterns and FTIR spectra of rehydroxylated OHA samples
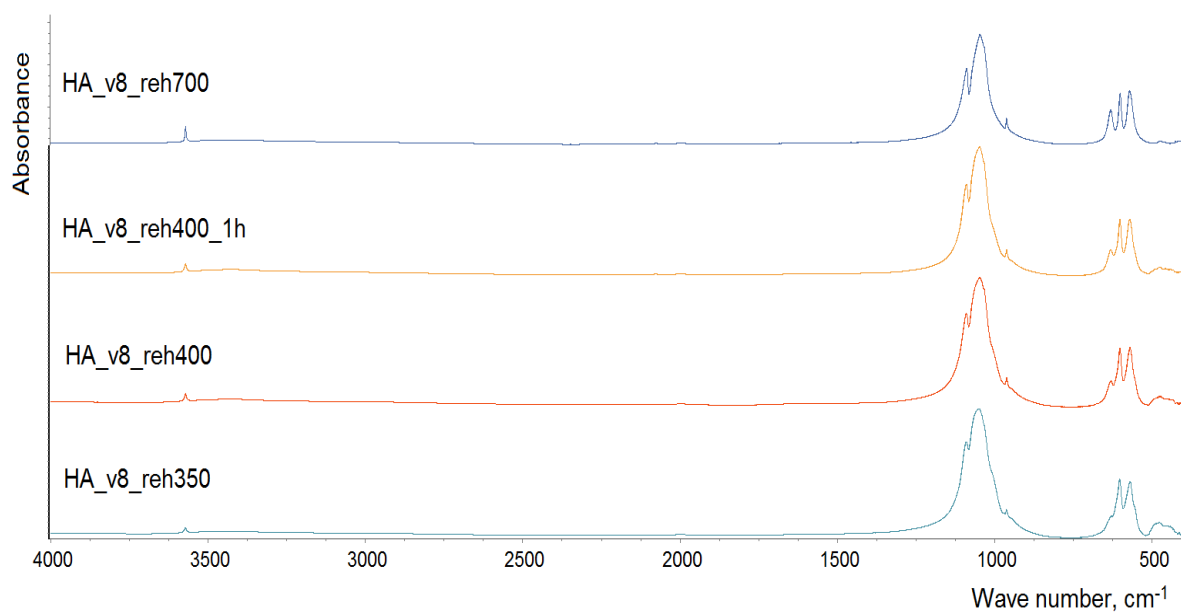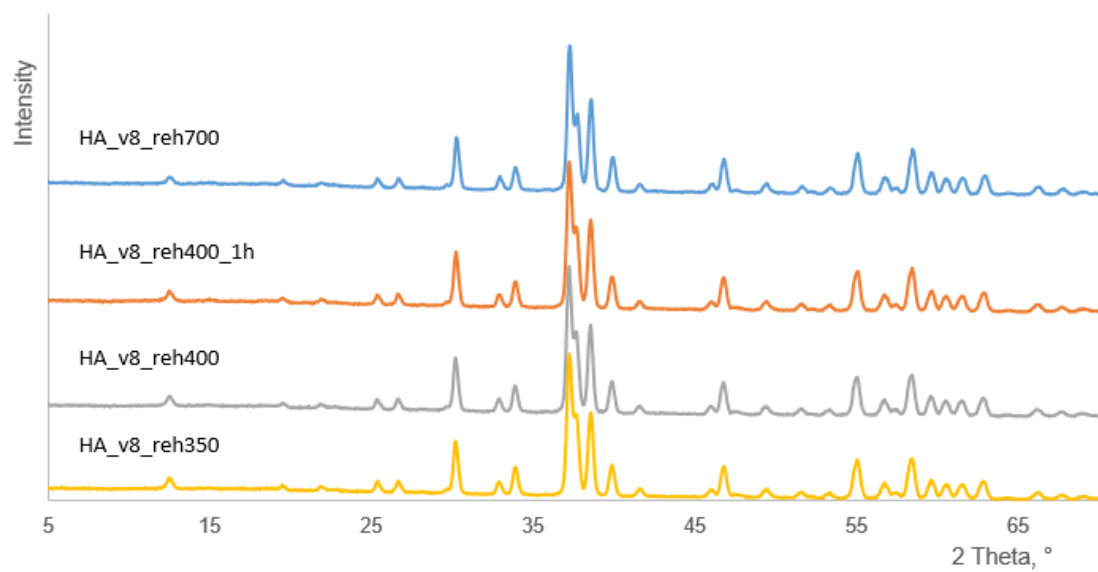
OH⁻ and PO_4^{3-} area data of OHA from deconvulated $500 - 750\ cm^{-1}$ FTIR spectral range

HA

	1		2		3		4	
	cm(-1)	Area	cm(-1)	Area	cm(-1)	Area	cm(-1)	Area
	653,5	0,8029	653,5	0,9793	653,5	0,4568	653,5	0,5151
	632,328	9,9715	632,411	9,516	632,343	4,3839	632,299	6,6554
	601,689	8,1468	601,993	7,9918	601,871	3,7484	601,973	5,7511
	574,714	5,4319	574,941	5,7733	574,729	2,671	574,897	3,978
	566,530	10,766	567,314	9,71	566,963	4,4381	567,693	6,8656
	550,027	2,9583	553,332	0,6785	553,332	0,8298	553,332	1,0003
	Sum(PO4)	27,303	Sum(PO4)	24,153	Sum(PO4)	11,687	Sum(PO4)	17,595

HA_v8_reh700

	1		2		3	
	cm(-1)	Area	cm(-1)	Area	cm(-1)	Area
	653,5	4,0762	653,5	0,7201	653,5	0,8902
	632,408	12,912	632,262	10,736	632,372	8,5568
	601,736	10,696	601,778	9,0542	601,787	7,1086
	574,176	9,6968	574,684	6,6027	575,117	4,4042
	565,493	11,836	567,025	9,758	567,340	8,8928
	551,520	2,7782	555,077	3,2252	553,332	2,4426
	Sum(PO4)	35,007	Sum(PO4)	28,640	Sum(PO4)	22,848

HA_v8_reh400_1h

	1		2		3		4	
	cm(-1)	Area	cm(-1)	Area	cm(-1)	Area	cm(-1)	Area
	653,5	0,1126	653,5	0,7896	653,5	1,1077	653,5	0,1188
	632,859	6,1029	632,892	8,7055	633,023	8,3189	632,550	6,7908

HA

	OH/PO4	Aver	%OH
1	0,36521	0,37813	100
2	0,39397		
3	0,37509		
4	0,37825		

HA_v8_reh700

	OH/PO4	Aver	%OH	Aver, %
1	0,36884	0,37274	97,543110	98,5735
2	0,37487		99,137161	
3	0,37450		99,040246	

HA_v8_reh400_1h

	OH/PO4	Aver	%OH	Aver, %
1	0,23905	0,25513	63,218555	67,4727
2	0,25785		68,190770	

Top PO4 area tables

cm(-1)	Area
610,551	2,7685
601,677	5,9131
575,111	7,0653
566,738	7,1944
552,917	2,5883
Sum(PO4)	25,529

cm(-1)	Area
611,494	3,4224
601,736	8,6777
574,980	10,950
566,069	8,055
552,965	2,6562
Sum(PO4)	33,761

cm(-1)	Area
610,379	3,8066
601,551	7,0679
575,310	9,2986
566,160	7,6394
552,281	3,1083
Sum(PO4)	30,920

cm(-1)	Area
611,114	2,4441
602,066	7,6138
575,223	8,2223
567,061	7,2618
553,786	1,5429
Sum(PO4)	27,084

reh400 area tables

1	
cm(-1)	Area
653,5	0,1843
632,927	4,1505
611,832	2,2681
602,057	4,9232
576,533	5,0576
567,255	5,8253
553,130	1,4457
Sum(PO4)	19,519

2	
cm(-1)	Area
653,5	0,3364
632,778	4,6505
611,366	2,4942
601,942	5,4063
576,767	5,0105
567,641	6,6343
553,834	1,4363
Sum(PO4)	20,981

3	
cm(-1)	Area
653,5	2,3126
633,008	5,2581
611,420	3,0921
601,873	5,4457
576,863	5,7829
567,367	6,7587
553,389	1,8469
Sum(PO4)	22,926

reh350 area tables

1	
cm(-1)	Area
653,5	0,1477
633,82	3,4239
612,508	4,3537
602,169	5,4575
580,092	4,3943
568,192	8,9634
553,045	2,392

2	
cm(-1)	Area
653,5	0,1004
633,685	3,025
612,522	3,4673
602,398	5,2343
580,990	2,5395
569,019	9,1219
553,349	1,3972

3	
cm(-1)	Area
653,5	0,6284
633,333	4,6844
612,576	4,8296
602,458	7,7698
579,465	5,9877
568,256	10,391
553,683	2,1274

Summary tables

3	0,26903		71,148788
4	0,25072		66,304961
5	0,25578		67,643969
6	0,25837		68,329448

HA_v8_reh400

	OH/PO4	Aver	%OH	Aver, %
1	0,21262		56,230915	
2	0,22164	0,22120	58,615621	58,4996
3	0,22934		60,652288	

HA_v8_reh350

	OH/PO4	Aver	%OH	Aver, %
1	0,13395		35,423972	
2	0,13901	0,14118	36,763328	37,3378
3	0,15059		39,826222	

HA_v8

	OH/PO4	Aver	%OH	Aver, %
1	0,03117		8,2434010	
2	0,03247	0,03137	8,5885242	8,29838
3	0,03049		8,0632259	

Sum(PO4)	25,560

Sum(PO4)	21,760

Sum(PO4)	31,105

1

cm(-1)	Area
653,5	0,7668
637,074	1,0513
613,661	8,5862
603,735	6,4065
582,734	5,7402
567,728	9,7741
553,213	3,2196
Sum(PO4)	33,726

2

cm(-1)	Area
653,5	0,3225
637,495	1,1143
614,001	7,9385
603,757	7,2573
582,470	6,1104
567,634	9,5008
553,442	3,5042
Sum(PO4)	34,311

3

cm(-1)	Area
653,5	0,0614
637,198	0,8028
614,172	4,8824
603,689	5,5918
583,947	1,6606
568,291	12,884
552,575	1,3111
Sum(PO4)	26,33

HA_v6

	OH/PO4	Aver	%OH	Aver, %
1	0,04645		12,284467	
2	0,04991	0,04622	13,199112	12,2238
3	0,04230		11,188000	

1

cm(-1)	Area
653,5	0,3608
636,515	1,5261
613,247	7,6138
603,345	6,379
583,256	3,7446
568,321	12,544
552,775	2,571
Sum(PO4)	32,853

2

cm(-1)	Area
653,5	0,3245
636,027	2,3157
614,148	8,6105
603,643	11,712
581,906	8,9835
567,854	12,934
553,896	4,1556
Sum(PO4)	46,397

3

cm(-1)	Area
653,5	0,5772
636,481	1,3398
613,164	7,1492
603,509	6,3662
581,896	6,1188
567,744	9,2138
553,411	2,8214
Sum(PO4)	31,669

Raman spectra of OHA samples
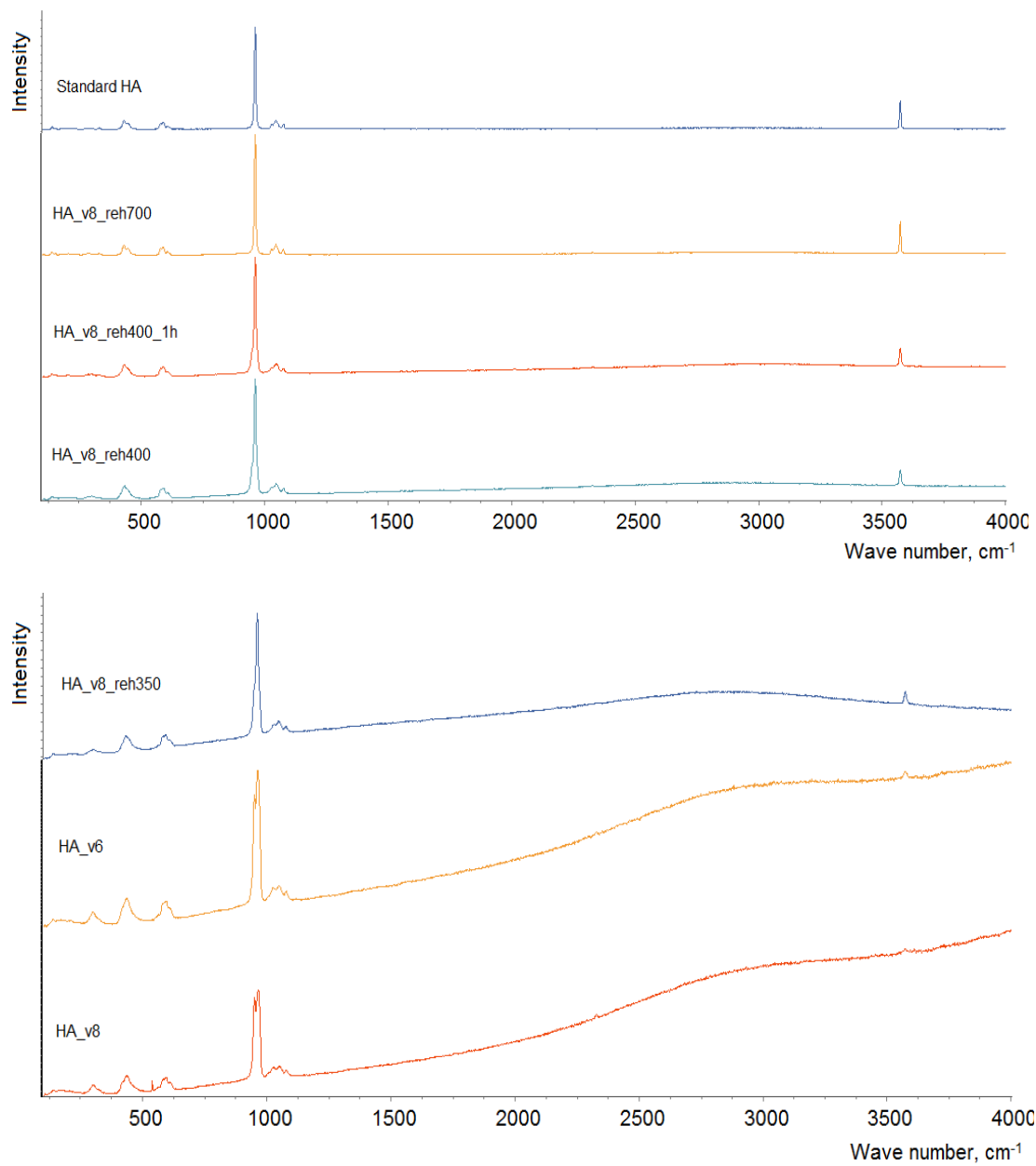
OH⁻ and PO_4^{3-} area data of commercial HA and HA coatings from deconvulated $500 – 750$ cm^{-1} FTIR spectral range

Commercial HA powder for coatings

1	653,5	0,3223
	634,573	1,1854
	615,319	1,3141
	603,007	4,6429
	576,794	4,2573
	566,642	3,2084
	555,160	1,016
sum po4	14,438	
	7	

2	653,5	0,417	3
	633,82	2,057	
	616,659	2,568	
	602,780	4,997	
	576,276	6,947	
	565,829	4,674	
	554,892	2,896	
sum po4	22,08		
	4		

3	653,5	0,1563
	634,779	1,0995
	615,315	1,3072
	602,749	4,7839
	576,139	3,6704
	565,184	3,2109
	555,800	1,1002
sum po4	14,072	
	6	

	OH/PO4	Aver	%OH	Aver, %	STDEV	ST Error
1	0,08209		21,7114	22,3361	2,05878	1,1886
2	0,09315	0,08446	24,6349	2	4	4
3	0,07813		20,6620			

0,378136 standard HA

cHA

1	653,5	0
	633,665	2,4694
	620,481	4,8359
	605,062	18,680
	581,338	12,586
	567,444	11,105
	553,577	4,2145
sum po4	51,422	

2	653,5	0
	633,665	0,9794
	621,629	2,3718
	603,053	8,6239
	575,094	8,7307
	564,251	4,5337
	554,210	1,1212
sum po4	25,381	

3	653,5	0
	634,779	1,1302
	615,31	1,3072
	602,74	9,9847
	576,13	10,793
	565,18	5,7821
	555,80	2,3494
sum po4	30,216	

	OH/PO4	Aver	%OH	Aver, %	STDEV	ST Error
1	0,04802		12,6996	10,931	1,5388	0,8884
2	0,03858	0,0413	10,2046			
3	0,03740		9,89148			

0,378136 standard HA

3	
653,5	0
633,0119	10,7456
615,8903	5,9042
601,999	20,0502
579,8903	16,7729
565,1842	13,0588
554,7893	6,7903
sum po4	62,5764

2	
653,5	0
633,8902	4,9037
616,893	3,9047
602,6792	10,7893
577,893	8,9004
565,903	5,1845
552,984	2,7561
sum po4	31,535

1	
653,5	0
633,4284	6,1101
617,6589	4,3891
602,9203	15,1105
579,2636	10,1696
566,2783	9,5906
552,2069	4,3416
sum po4	43,6014

ht-cHA					
OH/PO4	Aver	%OH	Aver, %	STDEV	ST Error
1	0,140135		37,05953			
2	0,1555	0,155785	41,12283	41,19817	4,176822	2,411489
3	0,17172		45,41215			

0,378136 standard HA

Appendix 8

Expression of bone cell markers in osteoblasts grown on conventional (HA1) and
hydrothermally treated (HA2) HA coatings after 7 and 14 days cell culture
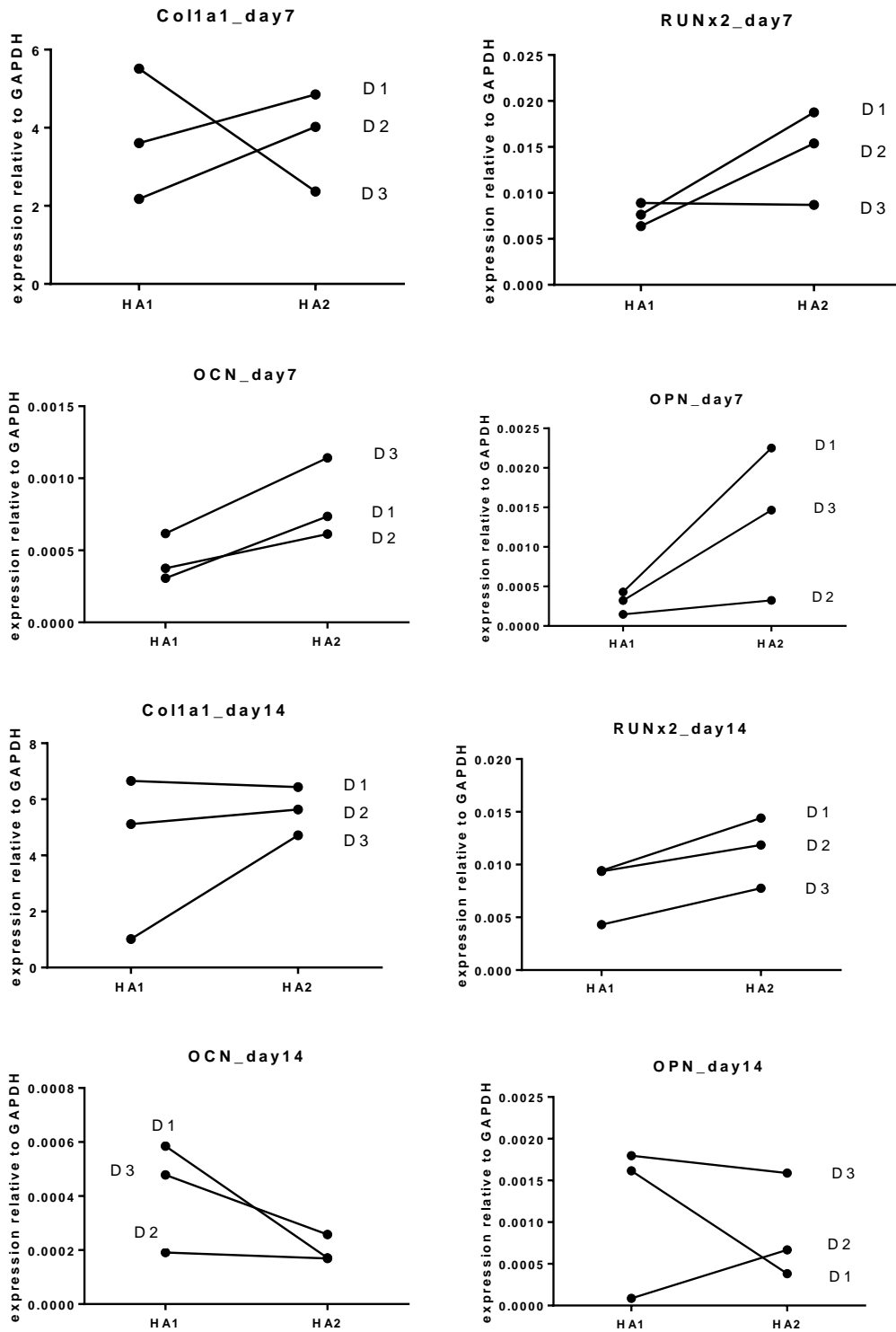
HA1 = cHA, HA2 = ht-cHA, D1 = donor 1, D2 = donor 2, D3 = donor 3